

Analysis of the Ocean Falls Wave Energy Converter in Regular Waves

M.I. Kelkitli

Analysis of the Ocean Falls Wave Energy Converter in Regular Waves

by

M.I. Kelkitli

to obtain the degree of Master of Science
at the Delft University of Technology,
to be defended publicly on Wednesday March 14, 2018 at 15:30 PM.



bam

infra

BAM Infraconsult bv

Student number:	4223314	
Project duration:	May 1, 2017 – March 14, 2018	
Thesis committee:	Prof. dr. ir. A. V. Metrikine	TU Delft
	Dr. ir. A. J. Laguna	TU Delft
	Dr. ir. J. D. Bricker	TU Delft
	Ir. E. ten Oever	BAM Infraconsult B.V.
	Ir. B. Reedijk	BAM Infraconsult B.V.

An electronic version of this thesis is available at <http://repository.tudelft.nl/>.



Abstract

There is a vast wave energy potential in the oceans of the world. Many promising technologies of wave energy conversion have been developed, such as the oscillating water column. BAM Infraconsult B.V. has developed the Ocean Falls concept of an oscillating water column that has the addition of a tube and a back wall, which is able to move in order to change the resonant characteristics of the structure to match incoming wave frequencies.

A numerical model has been made to capture the dynamic behaviour of the oscillating water column represented as a "rigid piston", where the system is modelled as a linear mass-spring-damper. The internal water surface is assumed to be horizontal and flat, both valid approximations for small chamber widths with respect to the wavelength of the incoming wave. The hydrodynamic coefficients, as well as the excitation force on the piston have been obtained using ANSYS AQWA. Thermodynamics in the chamber have been included by assuming a linear, adiabatic and reversible air flow. Furthermore, pressure oscillations in the chamber due to the oscillation of water are assumed small compared to the atmospheric pressure. The equation of motion of the piston is coupled to the pressure oscillations inside the air chamber, which includes linear turbine damping and air compressibility. The response of the system has been studied in the frequency domain for regular and irregular waves.

Model experiments have been performed to compare the linear model to experiment results for regular waves. The turbine damping has been modelled by adding a lid on the air chamber containing an opening where air can flow through. The area of the opening is related to the level of damping induced on the water surface inside the chamber. Two back wall positions and three different damping cases have been studied.

Air compression has been negated from the linear model while comparing to experiments due to scaling complications and the relatively small effect of air compression in the flume geometry of the Ocean Falls. For the case with no turbine damping, the model experiments indicate a longer resonant period compared to the linear model. This difference, to a smaller extent, is also visible in the damping cases. The measured flow in the damping cases is slightly larger than the linear model. Pressure measurements compare well with the linear model. Efficiency is defined to be the power in the waves divided by the power available to a power take-off system, such as a turbine. For the low damping case, the efficiency measured and efficiency computed in the linear model compare well and both give a peak efficiency of around 60%, contrary to the high damping cases where the model under-predicts the measured efficiency, indicating a higher damping input into the model possibly due to the linearisation of the damping. For high damping the experiments also give an efficiency of around 60%, while the numerical model predicts this to be circa 50%.

Acknowledgements

Firstly, I would like to thank my professor A.V. Metrikine and my daily supervisor A.J. Laguna for their outstanding guidance and patience with me. Antonio, thank you for always being ready to answer any question you are asked!

Secondly, I owe a great debt to the creator of the concept Erik ten Oever and I appreciate it that he was willing to spend his valuable time in giving me his exceptional insight in the problems I had faced. Also, many thanks are in order to Markus Muttray for his help and interest in this research. Additionally, I would like to thank the whole BAM Infraconsult Coastal department for their kindness and support. Also, special thanks go to Michael van de Koppel, Cas Hendriks and Vera Wong for their time in the wave lab.

Thirdly, I would like to acknowledge Heynen B.V. and Dennis de la Roy for providing me with the necessary pressure sensors to perform the experiments for my research. I am also very grateful to Jos van Driel for helping me set-up the sensors for the experiments. Their support for this research has not been in vain.

Last but definitely not least, my thanks go out to my dearest friends and family. My beloved friends, the Classic, whom I have known for more than 18 years have always been by my side and I cannot thank them enough. Son olarak, sevgisini ve desteğini benden hiçbir zaman esirgemeyen sevgili aileme teşekkürlerimi sunarım. Daima bana karşı sabırlı ve şefkatli olan sevgili annem Sevilenay'a, babam İrfan'a ve ağabeyim Salih Alpay'a sonsuz minnettarım.

*M.I. Kelkitli
Delft, March 2018*

Contents

Abstract	iii
1 Introduction	1
1.1 Context	1
1.2 Problem definition	1
1.3 Scope	1
1.4 Research approach	2
2 Literature review	5
2.1 Wave energy converters	5
2.1.1 Oscillating water columns	5
2.1.2 Oscillating body devices	6
2.1.3 Wave overtopping systems	6
2.2 Modelling of OWCs	7
2.2.1 Theoretical modelling	7
2.2.2 CFD modelling.	9
2.2.3 Experimental testing.	9
2.3 Conclusions.	10
3 Theoretical model	11
3.1 The Ocean Falls concept	11
3.2 Model derivation	11
3.2.1 Acting forces	12
3.2.2 Formulation of equations of motion	13
3.2.3 Thermodynamics of the air chamber	14
3.2.4 Linear turbine	16
3.3 Radiation and excitation forces	17
3.4 Discussion	18
3.5 Conclusions.	18
4 Analytical steady-state solution	19
4.1 Frequency domain solution.	19
4.2 Natural frequency analysis	20
4.3 Model validation	21
4.3.1 Open air chamber	21
4.3.2 Closed air chamber	21
4.4 Air compressibility analysis	21
4.4.1 Equations of motion without air compression	21
4.4.2 Solutions in frequency domain.	22
4.5 Power response to regular and irregular waves	22
4.5.1 Power yield in regular waves	23
4.5.2 Power yield in irregular waves	23
4.5.3 Capture width and efficiency.	25
4.5.4 Optimum turbine parameter.	26
4.6 Conclusions.	27
5 Experiment Methodology	29
5.1 Test objective	29
5.2 Description of the test facility.	29
5.3 Experiment set-up	29
5.3.1 Model bathymetry	29

5.3.2	Wave calibration	30
5.3.3	Model scaling	30
5.3.4	Regular waves	32
5.3.5	Thermodynamics in the air chamber	32
5.3.6	Cross section and model geometry.	34
5.3.7	Set-up of wave gauges, air pressure sensors and camera	34
5.4	Experiment program and protocol	36
5.5	Summary	36
6	Experiment results and comparison to theory	37
6.1	Wave reflection analysis.	37
6.1.1	Mansard & Funke method	37
6.1.2	Incident wave amplitudes	37
6.1.3	Reflection of the Ocean Falls structure	38
6.2	Data processing.	38
6.3	Response to no turbine damping	40
6.4	Determining equivalent linearised turbine parameter K_1	40
6.5	Flow and pressure.	42
6.6	Efficiency	43
6.7	Observations	49
6.7.1	Comparison of results	49
6.7.2	Experiment limitations	49
6.8	Conclusion	50
7	Discussion and conclusions	51
7.1	Discussion	51
7.1.1	Theoretical model	51
7.1.2	Experiment methodology and data processing.	51
7.2	Conclusion	52
7.3	Recommendations and further research proposals	53
7.3.1	Modelling	53
7.3.2	Experiments	53
7.3.3	Recommended further study.	54
	Bibliography	55
A	Solutions to potential flow theory	59
B	Ocean Falls ANSYS AQWA model	61
B.1	ANSYS AQWA	61
B.1.1	WAMIT/NEMOH comparison	62
B.1.2	ANSYS AQWA model	62
B.2	The Ocean Falls AQWA model.	65
B.2.1	Geometry definition	65
B.2.2	Mesh configuration	66
B.2.3	Input wave conditions	66
B.2.4	Results	67
B.3	Conclusion	67
C	Data acquisition and processing	69
C.1	Data acquisition	69
C.1.1	Wave gauges	69
C.1.2	Pressure sensors	70
C.2	Data processing.	70
D	Experiments program and protocol	73
D.1	Experiment program	73
D.2	Experiments protocol.	74

E	Non-linear time-domain model	77
E.1	Non-linear equations of motion.	77
E.2	State-space representation of the convolution	78
E.3	Solution in python	78
E.4	Results	79
	E.4.1 Validity of approximation	79
	E.4.2 Engineering approach to model and experiments comparison.	80
E.5	Discussion	80
E.6	Conclusion	84

Introduction

There is a large energy potential in the oceans of the world. One of these is the wave energy potential. Theoretically, the oceans contain around 3 TW of wave power, which is in the same order of magnitude of the world power usage [1]. This significant potential to supply the world with renewable energy is perhaps the most attractive reason to investigate the possibilities to capitalise on this potential. This report aims to contribute to the research of oscillating water column wave energy converters.

1.1. Context

One of the many types of wave energy converters is the oscillating water column (OWC). An OWC is a wave energy converter that consists of a wave capture chamber filled with air that is connected to an air turbine. The OWC principle essentially boils down to the interface between water and air, where, as incident waves reach the structure, the water level inside the chamber oscillates and in turn compresses and decompresses air in the chamber. This oscillation allows air to flow through the turbine, which then generates energy through the rotation of the turbine blades. The oscillation of water inside the chamber can be regarded as an oscillating mass with dynamic characteristics such as a natural period at which the system resonates.

BAM Infraconsult B.V. has developed the Ocean Falls OWC wave energy converter that has the addition of a tube with rectangular cross section and a moveable back wall that aims to change the resonant characteristics of the system to align with incident wave periods. This concept has a pneumatic power take-off, meaning the energy in the waves is extracted through air flow through a turbine.

1.2. Problem definition

This research aims to create a numerical model based on physical principles that predict the performance of the Ocean Falls in regular and irregular waves. This problem can be split into the following main research questions:

- *"How does the flow, pressure and power of the system computed through the theoretical model interact with regular and irregular waves and how does the Ocean Falls perform?"*
- *"What is the natural period of the system and how does the linear power take-off (PTO) damping and linear air compressibility influence the natural period?"*
- *"What is the effect of the statically moveable wall on the resonant characteristics of the system?"*
- *"How does the linear model compare to experiments performed for regular waves?"*

1.3. Scope

This report aims to contribute to the development of OWCs. Conventional OWC wave energy converters are generally designed to have a fixed natural period, whereas the Ocean Falls OWC's essential addition is that the system can statically adjust its natural period to tune it to incoming wave conditions. This is also the fundamental addition of this research.

The research questions mentioned above are aspired to be answered in this report. It is important to mention what is considered to fall within the scope of this research and what is not. Firstly, the aim of the theoretical model is to derive linear equations of motion for the oscillation of the water surface inside the chamber, the air flow through the turbine, the pressure inside the chamber and the power available to the turbine. This model includes the linearised air compressibility addition. The model will be solved for the steady-state response and for regular and irregular waves. Secondly, through the equations of motion, definitions for the undamped and damped natural frequency can be presented to assess the effect of geometric parameters on the resonant period of the system. Thirdly, model experiments performed for regular waves aim to validate the model and provide relevant data regarding the performance of the system. Finally, an initial performance assessment can be given for the Ocean Falls. It is important to note that performing the experiments for irregular waves and developing a non-linear model do not fall within the scope of this research.

1.4. Research approach

The problem is approached firstly by performing a literature study on the modelling of OWCs. From this the research splits into two directions; the first is the derivation and solution of the theoretical model and the second is the preparation, execution and processing of the experiments and experimental data. The theoretical model is combined with the hydrodynamic coefficients obtained through diffraction software ANSYS AQWA. Furthermore, the results obtained from both the model and experiments are compared and discussed. Based on this conclusions are drawn and recommendations are made. Finally, some further research proposals are given.

This chapter gives the introduction to the research, followed by chapter 2 that describes the literature reviewed for this research. Chapter 3 gives the theoretical model derivation after which chapter 4 gives the steady-state solution to the model in frequency domain. Chapter 5 describes the methodology used to perform the experiments and chapter 6 gives the experiment results and the comparison with the model. Finally, chapter 7 gives the important discussion points, followed by the conclusion and recommendations. The roadmap of this research is depicted visually in figure 1.1, also indicating the respective chapters of each section considered in this research.

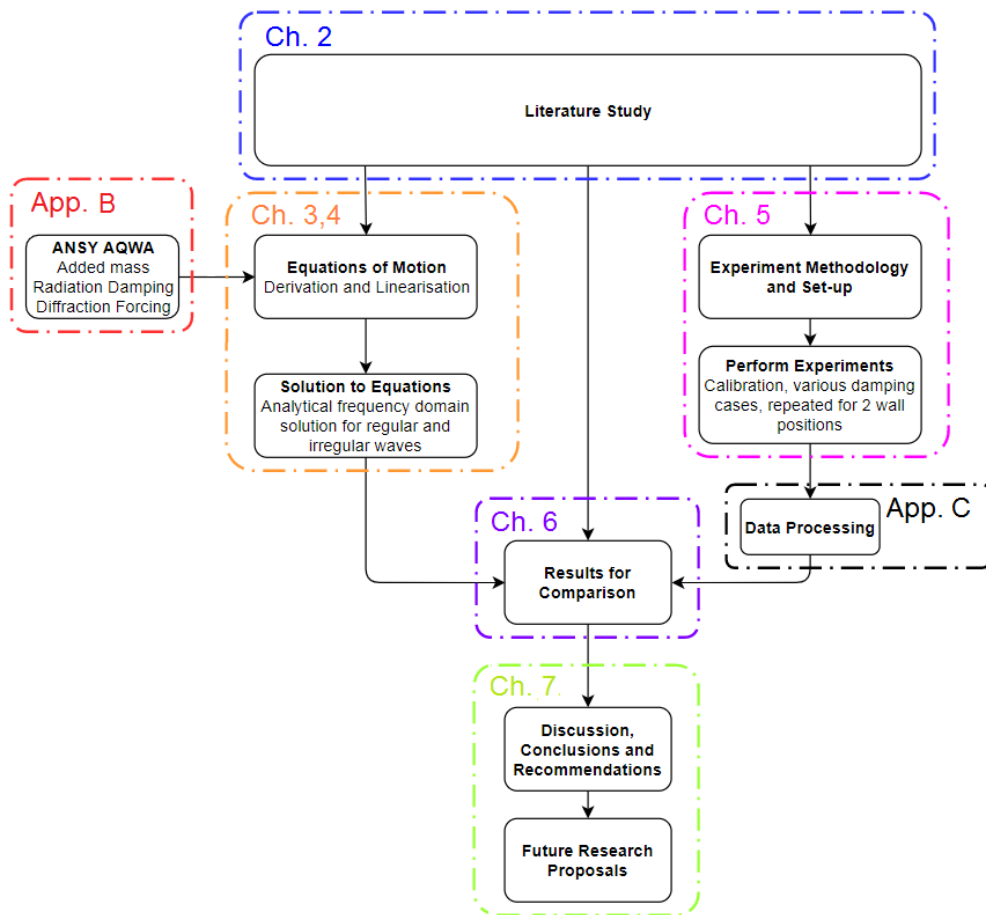


Figure 1.1: Flowchart of the set-up of the research and the respective chapters in this report.

2

Literature review

Many technologies exist to extract energy from the oceans, ranging from wave and tidal energy to ocean thermal energy conversion and osmotic power generation. Carefully considering the power of the former, wave energy, the oceans theoretically contain around 3 TW of wave power, which is in the same order of magnitude of the power usage in the world [1]. This significant potential to supply the world with renewable energy is perhaps the most attractive reason to investigate the possibilities to capitalise on this potential. With the recent political incentives set out by the European governments, the sector aims to produce 100 GW of power through wave and tidal energy by the year 2050 [2]. Considering the scope of this report, the focus will be on the wave energy aspect of the above mentioned numbers. This chapter contains a review of the state of the art of the wave energy sector, specifically on the modelling of oscillating water column wave energy converters, to place in context the numerical and experimental modelling performed within the scope of this research.

2.1. Wave energy converters

First, let us consider the technology around wave energy conversion. Through the past decades, reaching back to the 1980s, substantial efforts have been made to contribute to the development of wave energy conversion systems. According to McCormick [3] there are more than 1000 techniques to convert the energy in the waves to energy that can be used. These concepts are also increasing, where it seems like the wave energy industry is not converging to a general agreement of a technique but rather diverging. Several of these techniques have been developed and applied, where some have even harvested energy. Falcão [4] has conveniently classified wave energy converters according to their physical principles into three sub categories; oscillating water columns, oscillating body systems and over-topping converters. Let us consider several examples within these categories to illustrate the extent of wave energy conversion techniques.

2.1.1. Oscillating water columns

Firstly, the oscillating water column (OWC) wave energy converter is one of the most extensively studied and developed category of the ones mentioned above. The principle of an OWC is simple. Incoming waves oscillate a water surface inside a semi-enclosed structure with an air chamber, through which the air inside the chamber is compressed and decompressed, allowing an air flow through a turbine. In contrast to other wave energy converters the OWC indirectly extracts energy from waves, namely through pneumatic power take-off. A clear advantage of an OWC is its ability to be placed at shorelines and coastal regions. Also, because an OWC uses air flow to generate power, the turbine power take-off is employed at high rotational speeds, meaning a low torque and thus a more reliable generator for long term wave energy conversion, according to Sheng et al. [5], [6]. These advantages make the oscillating water column a popular choice as a wave energy converter. An often mentioned example is the first fixed oscillating water column to have been employed, the LIMPET plant installed on the Isle of Islay off the west coast of Scotland [7]. A more recent fixed oscillating water column, similar to the previous is the Mutriku OWC wave energy plant in the Mutriku town of Spain. See figure 2.1. This device is employed also as a breakwater adding to the functionality of the energy generator [8]. Although the Mutriku device has been struck by severe storms and has taken considerable damage, possibly due to some design and construction flaws, the device has provided power to circa 100 households after

modifications [9], [10].



Figure 2.1: The Mutriku breakwater oscillating water column from the air. This image has been taken from Marqués et al. [9].

Oscillating water columns are also to be found in floating form. Actually, perhaps considered one of the pioneers of wave power technology, Yoshio Masuda developed a navigation buoy equipped with an air turbine. The oscillation of the water compressed air through the turbine generating power. These buoys were considered the first wave energy devices deployed in open sea [11]. This working example has also been further applied widely. One example is the spar buoy optimised in Falcão et al. [12]. This concept is a moored spar buoy inside which a water column oscillates to generate energy. It has extensively been studied in [13], [14], [15]. Another interesting development is the oscillating water column combined with floating wind turbines. This concept employs OWC wave energy converters in the support structure of a floating wind turbine. The concept is modelled and analysed in experiments by Aubault et al. [16]. This device aims to, on the one hand damp out the motions of the floating device and on the other hand generate energy from the waves.

The above mentioned is just a fraction of the oscillating water columns developed around the world. More interesting devices are left for the reader to discover, because discussing them here would not fall within the scope of this research. In summary, the oscillating water column is a versatile and adaptive form of power generation.

2.1.2. Oscillating body devices

The second mentioned category is the oscillating body systems. Simply put, in contrast to oscillating water columns, oscillating body devices extract energy from the waves through the motion of a body, such as a heaving buoy or a pitching vertical wall.

One interesting example of an oscillating body system is the PELAMIS wave energy converter. This 750 kW wave energy converter is a floating device that drifts in open sea and has a snake-like appearance. The PELAMIS consists of longitudinal segments that are hinged together. As waves excite the system, the hinged joints rotate and activate hydraulic rams that pump fluids at high pressure through hydraulic motors, which in turn drive electrical generators [17]. See figure 2.2. The PELAMIS device has been discontinued.

2.1.3. Wave overtopping systems

This final category considered here is the wave overtopping devices. Such devices capture the water at the wave crest and store it in reservoir at a higher elevation than the average water elevation around it. This stored potential energy can be converted into electrical energy through hydraulic turbines.

A remarkable example of such a device is the Wave Dragon overtopping device. The system consists of two wide flaps that operate as wave reflectors to guide incoming waves to the centre ramp and into the reservoir that collects the overtopping water. Through hydraulic turbines this potential energy is converted into useful energy [18], [19]. See figure 2.3.

The mentioned cases above are presented here to give an indication of the available wave energy con-



Figure 2.2: The PELAMIS wave energy converter. Image has been taken from Yemm [17].



Figure 2.3: The Wave Dragon overtopping wave energy device. This image has been taken from Tedd and Kofoed [19].

verter devices. The amount of concepts is still growing and the sector does not seem to be converging to one working wave energy converter. More insight in the trend of the market can be found in the studies mentioned above and the references within those, because this does not fall within the scope of this report.

2.2. Modelling of OWCs

Let us now consider oscillating water columns again. This section aims to give an insight in the theoretical, numerical and experimental modelling of OWCs.

2.2.1. Theoretical modelling

One of the first people to model an oscillating water column was Michael McCormick in his published articles where he modelled a spar-buoy type OWC [20]. The model assumes the water inside a hollow floating structure to behave like a rigid piston oscillating in heave direction. Evans [21] continued this approach by solving the equations analytically for simple geometries as two parallel vertical walls in 2D and a cylindrical tube in 3D. These publications assumed no horizontal variation in elevation inside the chamber. This approach is called the "rigid piston" approach.

A more accurate approach is to assume a uniform pressure inside the air chamber, but allowing the internal water surface to vary horizontally. This approach also brings the inner reflections of the waves inside the chamber into consideration. The reflection from the inner walls is essentially disregarded in the rigid piston approach. This method was first applied in Sarmiento and Falcão [22] where the waves generated by a harmonic spatially uniform pressure applied on a segment of water surface are modelled. This method was generalised and adopted to apply to oscillating water columns in a comprehensive book by Falnes [23]. Chapter 7 of this book gives an explanation for the applied-pressure approach for oscillating water columns. Figure 2.4 taken from Falcão [11] depicts both approaches.

Let us consider the former approach in more detail. The rigid piston method essentially models the motion of the water surface as a flat horizontal piston and the dynamic model consists of a mass oscillating in heave direction that is connected to a spring and damper. The piston oscillation accelerates water mass around it and also radiates waves away from the column. Therefore, the spring represents the hydrostatic

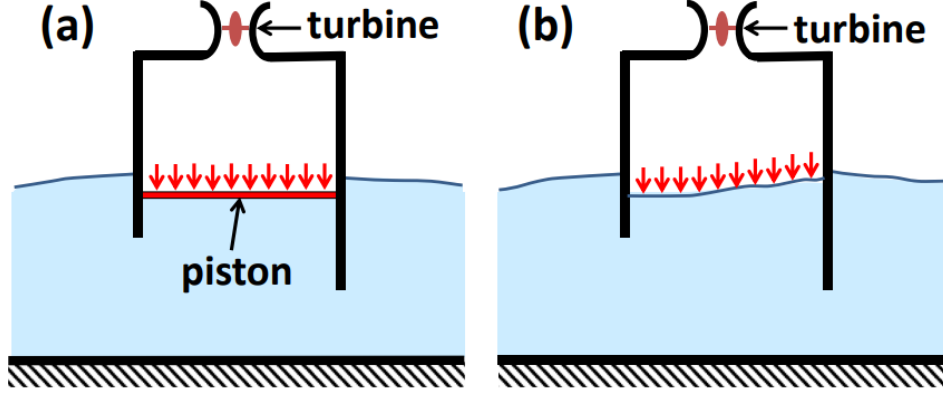


Figure 2.4: A visual depiction of two approaches to modelling OWCs. On the left hand side the rigid piston model is given and on the right hand side the spatially uniform pressure method is given. This drawing has been taken from Falcão et al. [11].

stiffness and the damper is the radiation damping and other forms of energy loss or energy extraction through power take-off systems. If $z(t)$ is the heave motion of the piston, the single degree of freedom equation of motion can be written in the time domain as

$$m\ddot{z}(t) = f_{rad}(t) + f_{hydrostatic}(t) + f_{pto}(t) + f_{wave}(t) \quad (2.1)$$

where m , $f_{rad}(t)$, $f_{hydrostatic}(t)$, $f_{pto}(t)$ and $f_{wave}(t)$ are respectively the mass of the piston, radiation forcing, hydrostatic forcing, power take-off forcing and wave excitation forcing. For complex geometries the hydrodynamic coefficients and wave excitation forces can be determined with the use of software such as WAMIT, ANSYS AQWA and NEMOH.

Let us now consider the uniform applied pressure approach. This method assumes a uniform air pressure applied to the internal water surface of the OWC. So, let us introduce a volume flow rate $q(t)$. Considering a linear model, the total volume flow rate can be equated to the superposition of the excitation flow rate and the radiation flow rate as

$$q(t) = q_e(t) + q_r(t) \quad (2.2)$$

where q_e and q_r are respectively the excitation flow rate (from wave excitation) and the radiation flow rate, due to the pressure oscillations inside the air chamber. For both the rigid piston and the uniform pressure approach the pressure inside the chamber $p(t)$ can be related to the volume of air inside the chamber and its change in time. This pressure relation can be extended to include compressible air or non-linear turbine performance characteristics.

Let us assume for now a simple linear relation between $q(t)$ and $p(t)$. This means that the system is linear and for harmonic time dependent excitations the steady-state response should also be harmonic, time-dependent with a possible phase shift. This enables the system to be solved in frequency domain for steady-state in regular waves. Following the theory of Evans and Porter [24] we further conveniently decompose the radiation flow rate in frequency domain as

$$Q_r = -(\tilde{B} + i\tilde{A}) \quad (2.3)$$

where \tilde{A} and \tilde{B} are analogous to respectively the added mass and radiation damping of the rigid piston approach. Note here that these values are not equal to the added mass and radiation damping coefficients in the rigid piston approach because both models are expected to give different results. Also using the analogy between electrical circuits, we can define the complex $-(\tilde{B} + i\tilde{A})$ as the radiation admittance, where \tilde{B} and \tilde{A} are respectively the radiation conductance and radiation susceptance, also in accordance with Falnes and McIver [25]. The above equations can be further elaborated and solved in the frequency domain. The solutions can be found in Evans and Porter [24] and Falnes and McIver [25]. An interesting article by Brendmo et al. [26] depicts the transformation of both the rigid piston and uniform applied pressure approach in terms of the mechanical mass spring damper system and the equivalent electrical circuit diagram.

Generally speaking, the relation between flow and pressure is not linear. The thermodynamics in the chamber can be non-linear but also the air turbine can introduce non-linearities. Non-linear equations of

motion cannot be solved in the frequency domain so these must be solved in the time domain. The time domain motion of a rigid floating body has been given by Cummins [27]. This representation can be used to define the time domain response of an oscillating water column as

$$(M + M_{A,\infty})\ddot{z}(t) = \int_0^t K(t-\tau)\dot{z}(\tau)d\tau - kz(t) + f_{wave}(t) + f_{pto}(t) \quad (2.4)$$

where $M_{A,\infty}$ is the added mass at very high frequencies and the integral term represents the radiation force. $K(t)$ is the impulse response function. Note here that equation 2.4 is the time domain equation for the rigid piston approach. The right hand side can be augmented to include non-linear forcing terms, such as friction. Solving these equations are more time consuming than the linear ones, but have been applied extensively. An alternative to directly solving the integral term in equation 2.4 is to approximate the integral term by a state-space model. This so called state-space model represents the integral term as a physical system of first order differential equations with input, output and state variables. The state-space approximation of the convolution term significantly reduces the computational time. An interesting published article by Iturrioz et al. [28] has employed a state-space model of the convolution term and extended it conveniently to solve the non-linear equations of motion in the time-domain. The model has been validated both with experiments and commercial CFD code. The research shows that the presented model is reliable and efficient in computational time sense.

A more simplistic approach to modelling non-linearities is to assume that the added mass and radiation damping coefficients are not frequency dependent but are constants. This replaces the convolution term by constant parameters for radiation damping and added mass. The system can then be made to include non-linear terms like quadratic pressure-flow relation and the differential equations can be solved numerically by employing an ODE solver, for example ode45 in Matlab. This has been done by Gervelas et al. [29] and compared to experimental data, where the model compares fairly well.

2.2.2. CFD modelling

The methods mentioned in the previous sections are in accordance with potential flow theory and its assumptions. Potential flow theory does not account for large wave and body motions and energy dissipation effects like viscous losses, turbulence and eddy shedding. These phenomenon might be interesting to investigate, especially in cases with large velocities. Computational Fluid Dynamics (CFD) codes have been developed to model the mentioned phenomenon. Generally speaking, these programs solve the Reynolds-averaged Navier Stokes equations (RANS). CFD also enables the inclusion of complexities in the geometry of the system. For example, in Amin [30] a vertical wall has been added to the internal water surface and the motions have been studied using CFD code. According to Amin, the addition of the vertical wall increases the efficiency of the system. Also, in Elhanafi [31] CFD code has been employed to optimise an offshore OWC in fully non-linear conditions. An obvious disadvantage of CFD software is the computational power and time it requires.

2.2.3. Experimental testing

OWCs have widely been tested in model scale and also somewhat in prototype scale. Before reviewing some of these cases let us take a look at scaling. In general, there are two methods of scaling prototypes to model dimensions: Froude scaling and Reynolds scaling, where the Froude number is kept constant in the former and the Reynolds number is kept constant in the latter. In Froude scaling the ratio between inertia forces and gravity forces are kept constant, whereas in Reynolds scaling the ratio between inertia forces and viscous forces are kept constant. In practice it is impossible to keep both the Froude and the Reynolds numbers constant while scaling, except for scaling factors close to 1. If we omit viscous effects, similitude using Froude scaling is preferable for OWCs.

An important complication is the scaling of the air chamber geometry. Let us define ϵ as the scale factor where $\epsilon = L_p/L_m$, where L_p and L_m are length parameters in respectively prototype and model scale. To scale the pressure inside the chamber one would need to scale the atmospheric pressure as well which is practically impossible, except for ϵ close to 1. A more convenient assumption would be to keep the atmospheric pressure constant in both prototype and model scale. This, however, according to Falcão [32], would mean the volume inside the chamber needs to be scaled with ϵ^2 instead of ϵ^3 .

Having said this, experimental study has contributed significantly to the development of OWCs. For example, in Koo and Kim [33], a land based OWC has been modelled to include non-linearities and has been compared to experiment results. Also in Chang et al. [34], a developed analytical model has been compared

to experimental results for a OWCs with different back plate angles and widths. Also, several other referenced articles in this chapter contain experimental studies.

2.3. Conclusions

This section contains an overview of the most important points discussed above.

- There is a wide variety of energy extraction from the oceans. One of which is the oscillating water column that extracts energy from the ocean's waves through a pneumatic power take-off system.
- In general, there are two methods to approach the modelling of OWCs, the rigid piston and the uniform applied pressure approach. The first method assumes the internal water surface to be a horizontal flat piston that oscillates in heave direction. The uniform applied pressure method is similar but allows for some variation in height horizontally inside the chamber and is thus a more realistic approach. The former is easier to apply to complex geometries because of the opportunity to make use of commercial software like WAMIT and ANSYS AQWA to determine the hydrodynamic coefficients.
- Both models can be extended to include non-linear dynamics, like non-linear power take-off damping or friction. These have been extensively applied for various OWCs.
- CFD code has been employed in studies to model non-linear phenomenon such as viscous losses, turbulence and eddy shedding. CFD is not limited by the assumptions of the linear wave theory and therefore aim give more accurate results. CFD code gives better results, but has the disadvantage of requiring significant computational time.
- OWCs have been extensively analysed with experiments. Scaling by keeping the Froude number constant is widely applied. Complications with scaling of air chamber require extra care while choosing model scale geometries.

3

Theoretical model

This chapter gives a comprehensive look at the "rigid piston" approach towards modelling the physics around the Ocean Falls concept. First the concept itself is presented, followed by the governing equations of the system and the model is described in the frequency domain for the linear case. Finally, the most important assumptions are briefly emphasized.

3.1. The Ocean Falls concept

The Ocean Falls oscillating water column wave energy converter concept is depicted schematically in figure 3.1. The concept consists of three key elements. The first is the tube connecting the incoming waves to the inner chamber inside the structure, which is the second element of the concept. Note here that the tube has a rectangular cross section. This chamber consists of a water and air compartment from which the energy of the waves is extracted through the compression of air through a turbine. And thirdly, the system contains a back wall which can be moved and fixed in various positions. This wall is aimed to statically vary the resonant characteristics of the system to tune it to incoming wave frequencies.

3.2. Model derivation

Let us define the coordinate system at the centre of the internal water surface, with z pointing upwards and x to the right in the direction of the wave propagation. Figure 3.2 gives a simplified schematic view of the system. The Ocean Falls consists of an internal water-air chamber connected through a tube to the open sea. The mean water level is set at $z = 0$. Under assumptions of linear water-wave theory, the flow in two dimensions is expressed in terms of the velocity potential $\phi(x, z, t)$. $\phi(x, z, t)$ needs to satisfy

$$\begin{aligned} \nabla^2 \phi &= 0, & \text{in fluid domain} \\ \phi_n &= 0, & \text{on fixed boundaries} \end{aligned} \quad (3.1)$$

where n gives the normal direction of the derivative. The linearised dynamic free surface condition at $z = 0$ is given by

$$-\frac{\partial \phi}{\partial t} + g\eta = \begin{cases} p(t)/\rho_w & \text{on internal free surface} \\ 0 & \text{on free surface outside chamber} \end{cases} \quad (3.2)$$

and the kinematic free surface condition at $z = 0$ by

$$\frac{\partial \eta}{\partial t} = \frac{\partial \phi}{\partial z} \quad (3.3)$$

The solutions to the potential flow theory are given in appendix A.

Several different approaches have been developed and applied to solve the hydrodynamic problem of OWCs. Generally speaking, one can distinguish two widely used methods, according to Falcão et al. [11]. These have been discussed in the previous chapter. Let us choose the rigid piston approach to model the Ocean Falls, based on the fact that the Ocean Falls has a complex geometry and the more obvious physical

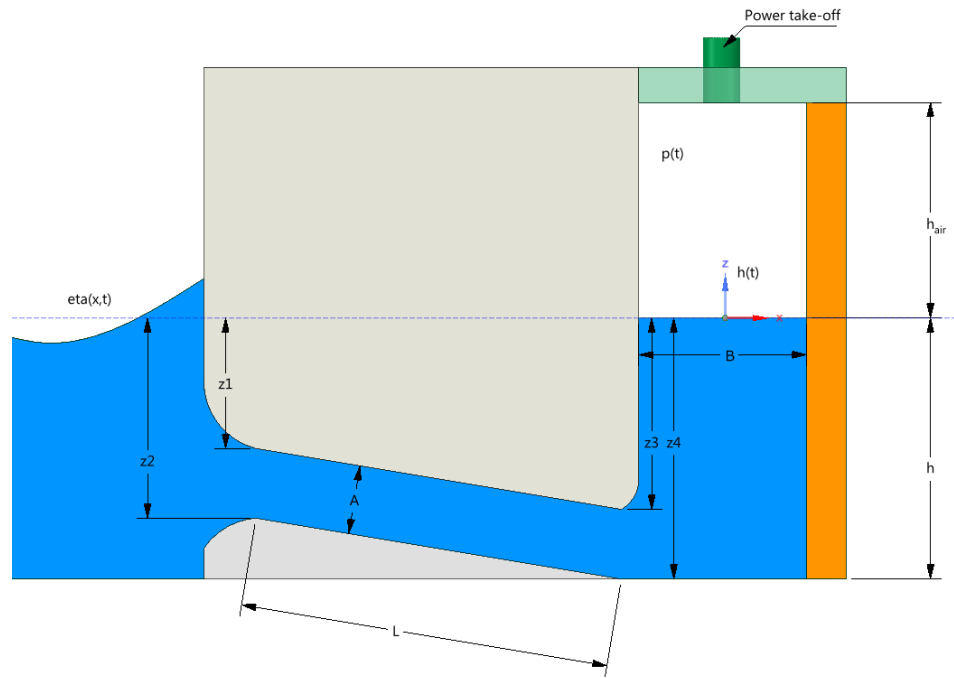


Figure 3.1: Ocean Falls schematic side view. The moveable wall is the wall on the far right.

interpretation of the rigid piston model compared to the uniform pressure model. The key difference to note between conventional rigid piston models and the one employed here is, however, the piston in the Ocean Falls concept is essentially a rigid body oscillating in the tube. The internal free surface is still assumed to be horizontal and flat. The presence of the tube in the Ocean Falls changes the physics of the system with respect to conventional oscillating water columns. The only way water can enter or leave the structure is through the tube. Therefore the oscillation of the water mass in the structure is physically governed by the oscillation of water in the tube. In other words, the system is considered as two reservoirs connected through the tube. Let us consider the oscillation of the water mass in the tube in terms of Newton's second law of motion. The following section gives a brief overview of the forces acting on this rigid body.

3.2.1. Acting forces

The forces acting on the rigid body are given below. Figure 3.3 gives the free body diagram of the tube water mass and the forces acting on it. The quantities represented in figures 3.2 and 3.3 have been adopted in this section.

- **Inertia force**

The first force to mention is the inertia of the oscillating mass, which is considered as a rigid body, equal to $m_t \ddot{U}$, where $U(t)$ is the flow through the tube and m_t is the water mass in the tube. Based on the assumption that the water is incompressible, in line with linear wave theory, mass continuity applies, meaning the flow of water through the tube can be given in terms of motion of the elevation inside the chamber.

- **Hydrostatic and gravity forces**

The hydrostatic forces are simply given by integrating the static water pressure over the cross sectional area of the tube. Considering the fact that there is no flow of water if both the water elevation inside and outside the structure are equal, the hydrostatic forces should cancel out. Since the internal water surface is taken to not vary in the x -direction, the elevation of the water column inside the chamber also acts as a hydrostatic forcing on the oscillating mass.

- **Air pressure force**

The air pressure change inside the chamber will cause an additional force on the tube equal to the pressure integrated over the cross sectional area of the tube.

- **Radiation force**

Due to the variation of the pressure inside the chamber the mass of water inside the structure will oscillate, accelerating the water mass around it and generating radiation waves. The radiation force, can be decomposed into forces which are in phase with the acceleration and the velocity of the rigid body. These forces can be represented through the added mass and hydrodynamic damping, respectively. These coefficients are determined through ANSYS AQWA, because the system geometry is considered complex.

- **Wave excitation force**

Finally, the wave forcing that acts on the oscillating body needs to be considered. This can be split into two parts, the first is the undisturbed wave forcing (no body considered) given by the Froude-Krylov force and the second is the correction to the Froude-Krylov force due to the presence of the structure, given as the diffraction force. As geometries become more complex it is more difficult to analytically define the diffraction force which is why numerical diffraction software ANSYS AQWA is utilised. The combined Froude-Krylov and diffraction forces in the time domain will be further given by one term as and referred to as $f_{wave}(t)$.

A variation on the mean water level at the seaside (say for example tidal oscillations) is not taken into account within the scope of this research, but can easily be done by adding an additional hydrostatic force on the seaside in addition to the hydrodynamic wave loading. The optimum geometry of the Ocean Falls is not dependent on the water height, so investigating this is not interesting at this stage.

3.2.2. Formulation of equations of motion

The momentum of the mass is given by $m_t U(t)$. Now, differentiating the momentum equation with respect to time and considering the forces mentioned above in terms of pressure gives us the second order differential equation for the single degree of freedom oscillation of the water mass in the tube in time-domain as

$$m_t \frac{dU}{dt} = \int_{z_2}^{z_1} p_{sea} dz - \int_{z_4}^{z_3} p_c dz + m_t g \sin(\theta) - f_{rad}(t) \quad (3.4)$$

where p_{sea} is the water pressure at the entrance of the tube and p_c is the pressure in the water at the chamber side of the tube.

The first forcing term on the right hand side is given by integration of the water pressure along the cross sectional area of the tube before the tube entrance. Similarly, the forcing term for the tube exit on the right side (chamber) can be obtained by integrating the water and chamber air pressures. Due to the inclination of the tube, there is an additional component of the gravitational force of the water mass that needs to be considered. Also, the oscillation of the air pressure inside the chamber will radiate waves and accelerate water around the column, so there is a radiation force that needs to be included. The friction in the channel and in- and outlet losses are not considered. Also, since there is no variation in cross sectional area of the tube and the velocity in the entrance and exit of the tube is assumed to be equal, no additional forces need to be considered. See figures 3.2 and 3.3.

The sea pressure is separated into a dynamic (waves) and a hydrostatic part, and similarly the pressure in the structure is also separated into hydrostatic pressure and the contribution of the oscillation of the air pressure. Assumed is that the water surface inside the structure also acts as a rigid piston, meaning no variation in x-direction applies to $h(t)$. Thus, the hydrostatic term of the pressure at the chamber side can be split into two components, as is done in equation 3.6. Elaboration of the hydrostatic integrals and the inclined gravitational force of the tube cancel out, because the cross sectional area of the tube is non-variant along the length. Here A is assumed to be equal to $z_2 - z_1$ and similarly equal to $z_4 - z_3$, a viable assumption on the condition that the angle θ is small.

Considering what is described above and specifying the integral terms in equation 3.4 gives

$$\int_{z_2}^{z_1} p_{sea} dz = f_{wave}(t) + \int_{z_2}^{z_1} \rho_w d g z dz \quad (3.5)$$

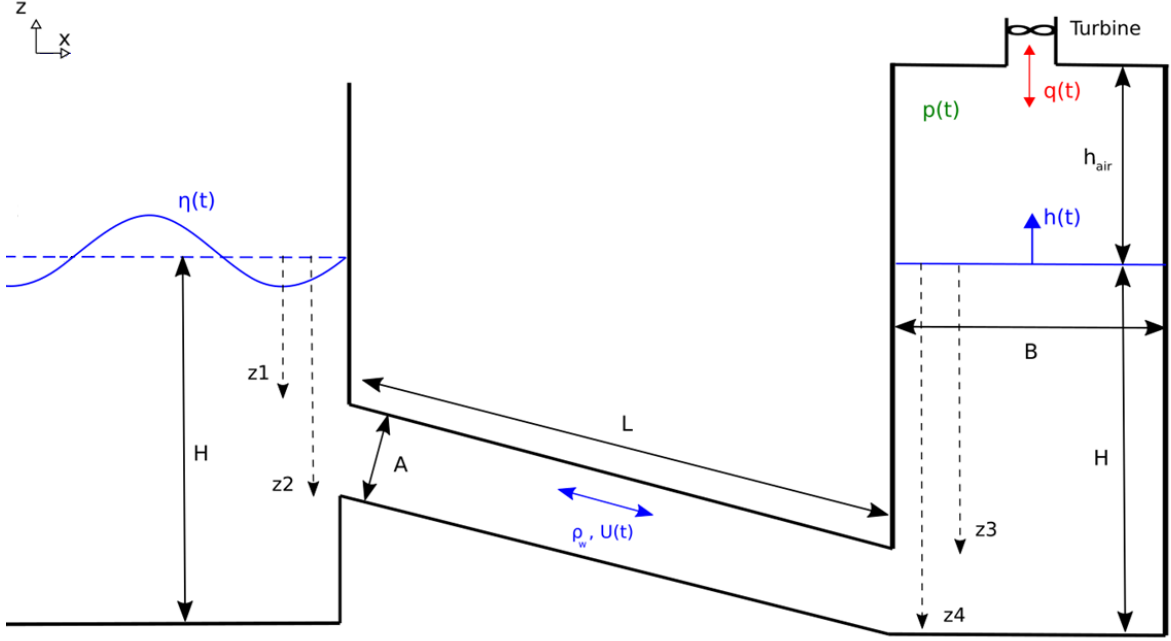


Figure 3.2: Simplified Ocean Falls schematic side view. The moveable wall is the wall on the far right.

$$\int_{z_4}^{z_3} p_c dz = f_p(t) + \int_{z_4}^{z_3} \rho_w g dz + \int_{z_4}^{z_3} \rho_w g dh(t) dz \quad (3.6)$$

where d is the depth of the structure in y -direction and $f_p(t)$ is the air pressure force acting on the rigid body.

To combine the oscillation of the mass in the tube with the water surface elevation inside the chamber, the mass conservation law for incompressible fluids needs to be used. This yields

$$U(t) = \frac{B}{A} \dot{h}(t) \quad (3.7)$$

Since long crested waves are assumed (i.e. the variation of the crest level along the width of the caisson in y -direction is neglected) the problem can be simplified to a 2-dimensional one by dividing d out, giving the equation of motion in time domain for the oscillation of the internal water surface, as

$$\rho_w B \ddot{h}(t) + \frac{\rho_w g A}{L} h(t) + \frac{A}{L} p(t) = \frac{f_{wave}(t)}{dL} - \frac{f_{rad}(t)}{dL} \quad (3.8)$$

where B is the width of the chamber, d is the depth of the structure in y -direction, L is the length of the tube, A is the height of the tube, f_{rad} is the radiation forcing, $p(t)$ is the air pressure inside the chamber and f_{wave} is the wave forcing on the oscillating body.

3.2.3. Thermodynamics of the air chamber

The variation of the pressure inside the chamber will induce a force on the piston. Assuming uniform pressure in the chamber and a flat internal free surface, the pressure force on the piston can easily be given by $F_p = Ap(t)$, where A is the tube area (or piston area) and $p(t)$ the uniform pressure fluctuation inside the chamber. This extra forcing term gives rise to the need of a second equation to account for the coupling of the system, one that defines the pressure inside the chamber. This is the mass conservation equation inside the air chamber. The discussion below follows the derivation by Sheng et al. [35] and Gomes et al. [14].

The airflow through the turbine is given by

$$\dot{m}(t) = - \frac{d\rho(t)V(t)}{dt} \quad (3.9)$$

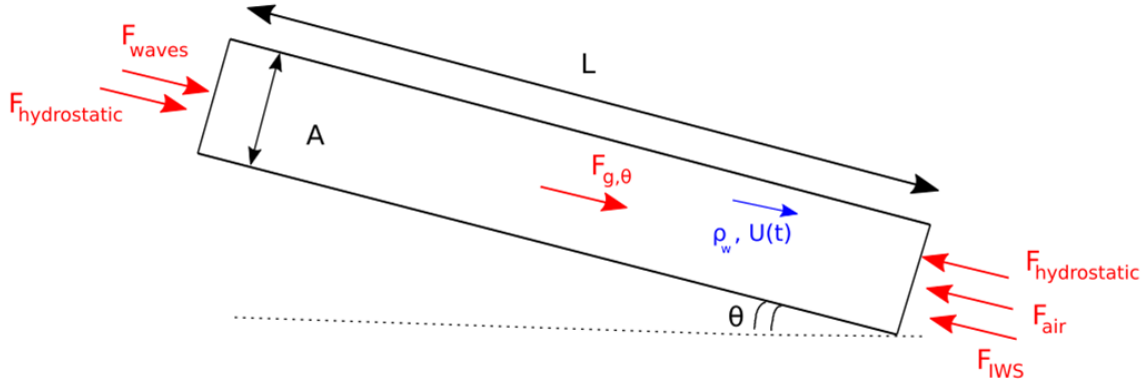


Figure 3.3: Free body diagram of the oscillating tube mass. F_{waves} , F_{air} and F_{IWS} are, respectively, the wave, the chamber air pressure and chamber internal free surface forces on the tube mass. F_g is the gravitational force that is decomposed in a force acting parallel to the other stated forces. The summation of the hydrostatic forces and this gravity force decomposition cancel each other out.

where $\rho(t)$ and $V(t)$ are the air density and the volume of the chamber, respectively. Important is to note that the relation between flow and change in volume is negative, because a positive change in internal water surface will cause a decrease in volume if one assumes positive mass flow is exhalation. Based on the fact that the air in the chamber is compressible, there needs to be a distinction between air entering the chamber and air exiting the chamber (inhalation/exhalation), because compressed air will have a larger density than atmospheric air. This distinction is made as follows

$$Q_{in}(t) = -1/\rho_c \dot{m}(t) \quad (\text{Exhalation}) \quad (3.10)$$

$$Q_{ex}(t) = -1/\rho_a \dot{m}(t) \quad (\text{Inhalation}) \quad (3.11)$$

where ρ_a and ρ_c is respectively the atmospheric air density (1.225 kg/m^3) and the air density inside the chamber. Considering an ideal gas and that the compression inside the chamber is an isentropic process, the gas law applies, namely:

$$\frac{p}{\rho^\gamma} = \text{constant} \quad (3.12)$$

where ρ_a and p_a are respectively the atmospheric air density and pressure. ρ_c and p are respectively the air density and air pressure in the chamber and γ is the specific heat ratio of air, equal to 1.4. So, equating the ideal gas statement for the air inside and outside the chamber gives

$$\frac{p(t) + p_a}{\rho_c^\gamma} = \frac{p_a}{\rho_a^\gamma} \quad (3.13)$$

and rearranging gives

$$\rho_c(t) = \left(1 + \frac{p(t)}{p_a}\right)^{\frac{1}{\gamma}} \rho_a \quad (3.14)$$

Expanding the above equation with the Taylor series until the third term for $\gamma > 0$, gives

$$\left(1 + \frac{p(t)}{p_a}\right)^{\frac{1}{\gamma}} = 1 + \frac{\ln\left(1 + \frac{p(t)}{p_a}\right)}{\gamma} + \mathcal{O}\left(\left(\frac{1}{\gamma}\right)^2\right) \quad (3.15)$$

and similarly expanding $\left[\ln\left(1 + \frac{p(t)}{p_a}\right)\right]$

$$\ln\left(1 + \frac{p(t)}{p_a}\right) = \frac{p(t)}{p_a} - \frac{1}{2}\left(\frac{p(t)}{p_a}\right)^2 + \mathcal{O}\left(\left(\frac{p(t)}{p_a}\right)^3\right) \quad (3.16)$$

Assuming the absolute pressure change inside the chamber is much smaller than the atmospheric pressure, equation 3.14 can easily be linearised. The assumption that the pressure change is small is a viable one, since the atmospheric pressure is of order 10^5 Pa, significantly larger than pressure differences occurring in OWCs according to Sheng et al. [5]. The linearised equation reduces to

$$\rho_c(t) = \rho_a \left(1 + \frac{p(t)}{\gamma p_a}\right) \quad (3.17)$$

Substituting equation 3.17 and its derivative into equations 3.10 and 3.11 gives the following equations

$$Q_{in}(t) = Bd\dot{h}(t) - \frac{Bd(h_{air} - h(t))}{\gamma p_a + p(t)} \dot{p}(t) \quad (\text{Inhalation}) \quad (3.18)$$

$$Q_{ex}(t) = \left(1 + \frac{p(t)}{\gamma p_a}\right) Bd\dot{h}(t) - \frac{Bd(h_{air} - h(t))}{\gamma p_a} \dot{p}(t) \quad (\text{Exhalation}) \quad (3.19)$$

where Q is the air flow in m^3/s . Assuming that the pressure change $p(t)$ is small compared to p_a and that the air chamber height h_{air} is large compared to internal free surface elevation $h(t)$, the system linearises to the following equation for inhalation and exhalation

$$\dot{m}(t) = \rho_a Bd\dot{h}(t) - \frac{\rho_a Bd h_{air}}{\gamma p_a} \dot{p}(t) \quad (3.20)$$

3.2.4. Linear turbine

The left hand side of equation 3.20 can now be equated to a certain mass flow rate through a turbine. In the case of OWCs a self rectifying turbine is needed, meaning flow in two directions is converted to a uni-directional flow for the turbine. Two common turbines to choose for OWCs with pneumatic power take-off are the Wells turbine, invented by A.A. Wells, and the bi-radial impulse turbine. According to Falcão et al. [15] the bi-radial impulse turbine is more effective for OWCs in various sea states, with also the advantage of a substantially smaller rotor diameter. However, bi-radial turbines need to be modelled non-linearly, whereas a Wells turbine can be linearly approximated fairly well. The extent of validity of this relation has been discussed in Gato et al. [36]. Therefore the Wells turbine has been chosen for this research.

In order to relate the air pressure inside the chamber to the mass flow in and out of the chamber, characteristic curves according to Dixon [37] are introduced as

$$\Psi = \frac{p}{\rho_a \Omega^2 D^2}, \quad \Phi = \frac{\dot{m}}{\rho_a \Omega D^3} \quad (3.21)$$

where Ω and D are respectively the angular velocity and turbine diameter. Also assuming a linear relation between the dimensionless flow and pressure gives

$$\Phi = K\Psi. \quad (3.22)$$

where K is the dimensionless turbine proportionality constant. Combining equation 3.21 and 3.22 yields the linear relation between the pressure and mass flow in time-domain as

$$\dot{m}(t) = \frac{KD}{\Omega} p(t) \quad (3.23)$$

where the turbine constants combined are called the turbine coefficient. Optimising the turbine diameter and rotational speed is not within the scope of this research, so therefore the flow through the turbine is given as

$$\dot{m}(t) = k_1 p(t) \quad (3.24)$$

where k_1 is the turbine parameter as mentioned above and will be referred to this way throughout the extent of this report. Combining equations 3.20 and 3.24 and dividing by the width of the system in y-direction d yields the following continuity equation for mass flow through the turbine in linearised form

$$\frac{k_1}{d} p(t) = \rho_a B \dot{h}(t) - \frac{B h_{air}}{c^2} \dot{p}(t) \quad (3.25)$$

where the speed of sound in air c is introduced as

$$c^2 = \frac{\rho_a}{\gamma p_a} \quad (3.26)$$

Note that a negative flow resembles an inhalation of air (since mass enters the chamber). This second term on the right hand side of equation 3.25 gives the spring like effect of the air chamber on the piston in heave motion. The effect of this air compressibility term is increased with increasing height of the chamber. The air density and speed of sound in air (c) are taken to be constant. The validity and adequacy of this approximation has been discussed in detail by Falcão and Justino in [38] and Sarmiento and Falcão in [22].

The coupled equations of motion can now be written as

$$\rho_w B \ddot{h}(t) + \frac{\rho_w g A}{L} h(t) + \frac{A}{L} p(t) = \frac{f_{wave}(t)}{dL} - \frac{f_{rad}(t)}{dL} \quad (3.27)$$

$$K_1 p(t) = \rho_a B \dot{h}(t) - \frac{B h_{air}}{c^2} \dot{p}(t) \quad (3.28)$$

where K_1 now is given in the respective unit per meter in y-direction. Finally, the power available to the PTO can be given by

$$P_t(t) = \frac{\dot{m}(t)}{\rho_a} p(t) \quad (3.29)$$

Making use of equation 3.23 and its simplification the above equation can be rewritten as

$$P_t(t) = \frac{K_1}{\rho_a} p(t)^2 \quad (3.30)$$

where P_t is the instantaneous power available to the turbine in W/m . Equations 3.27 and 3.28 are the equations of motion to be solved in the following chapter.

3.3. Radiation and excitation forces

An important part of the equations of motion that still has not been accounted for is the radiation and diffraction forcing. As the internal water surface oscillates, additional water particles around it will oscillate and waves will be radiated away from the structure. This radiation will remove energy from the system and thus the initial oscillation of the water surface will dampen out. Also, since the geometry of the structure is not simple, the wave forcing will be disrupted by the presence of the system. Both the radiation and diffraction forcing therefore needs to be incorporated somehow. The radiation forcing can be considered in the frequency domain as

$$\tilde{F}_{rad} = -\omega^2 A(\omega) \tilde{H} + i\omega B(\omega) \tilde{H} \quad (3.31)$$

where $A(\omega)$, $B(\omega)$ and \tilde{H} are respectively the frequency dependent added mass, radiation damping and complex amplitude of the internal water surface elevation. This frequency domain representation cannot be solved directly in the time domain, but can be solved through a convolution integral as in Cummins [27]. Also see equation 2.4. However, since the equations are linear, the steady-state solution can be found in the frequency domain.

The determination of the added mass, radiation damping coefficients and wave excitation forces is done through ANSYS AQWA. This software is a boundary element method (BEM) diffraction software, meaning the geometry of the system is split into a finite amount of panels that have the boundary condition that no water can move through them. The software then exerts an input wave forcing on an oscillatory body, in the case of AQWA it applies wave pressures at different phases and solves the numerical problem for each panel yielding a pressure distribution on the panels. AQWA gives the frequency dependant hydrodynamic coefficients for

added mass, radiation damping and diffraction forcing. However in the case of oscillating water columns it is slightly more complex to input these into software such as AQWA, because the oscillating body essentially is water. An in depth analysis has been performed to accurately model the Ocean Falls into AQWA in appendix B.

3.4. Discussion

The model derived above is a linear representation of the reality. We have made several assumptions in deriving these equations of motion. A brief overview of the assumptions and conclusions from this chapter are given below.

- Firstly, it is important to state that linear wave theory applies here. In other words the water fluid is assumed homogeneous, inviscid and incompressible, the surface tension is neglected, the flow is irrotational, waves are long-crested (two dimensional) and the wave amplitude is assumed small. The validity of these assumptions are assumed known and will not be discussed within the scope of this work.
- The width of the chamber B is assumed small with respect to incident wavelengths, so no variations in x -direction inside the chamber are present meaning the internal water surface has an oscillatory piston motion. For large chamber widths compared to wavelength the piston approach loses its validity.
- The pressure inside the chamber is assumed to be uniform and the relation between pressure and flow through the turbine is assumed to be linear. Also, ideal gas laws have been assumed meaning the compression and decompression of the air inside the chamber is an adiabatic and reversible process (no transfer of heat and matter). If the amplitude of the elevation inside the chamber is large with respect to the air chamber height, the linear approximation loses validity; because the air compression term is not dependent on the internal water surface elevation.
- Furthermore, frictional losses, thermodynamic losses and other non-linear phenomenon have not been included in this model.

3.5. Conclusions

In this chapter a theoretical derivation of the equations of motion were given. The concluding remarks are given below.

- The system is modelled as a rigid piston oscillating in one degree of freedom. Contrary to conventional oscillating water columns the piston in the Ocean Falls is represented by the tube.
- The dynamic model of system is considered to be a one degree of freedom single mass oscillating with a stiffness and damper attached, respectively representing the hydrostatic stiffness and radiation damping. The thermodynamics in the chamber are translated as a spring and damper aligned in series into this model, where the spring represents the compression of the air and the damper represents the power take-off. The oscillating mass and hydrostatic spring are given by the tube geometry.
- Since there is a body oscillating in water the radiation force must be considered. The added mass and radiation damping coefficients are determined through the ANSYS AQWA program. Also, since the geometry is complex, the wave excitation on the tube piston is computed numerically in AQWA.

4

Analytical steady-state solution

This chapter contains the frequency domain solutions to the equations of motion derived in the previous chapter. Note that all solutions are given in the model scale geometry of the Ocean Falls.

4.1. Frequency domain solution

The equations of motion for a single degree of freedom in the time domain derived in the previous chapter are presented here again as

$$\rho_w B \ddot{h}(t) + \frac{\rho_w g A}{L} h(t) + \frac{A}{L} p(t) = \frac{f_{wave}(t)}{dL} - \frac{f_{rad}(t)}{dL} \quad (4.1)$$

$$K_1 p(t) = \rho_a B \dot{h}(t) - \frac{B h_{air}}{c^2} \dot{p}(t) \quad (4.2)$$

Both equations 4.1 and 4.2 are linearised and can be solved linearly in the frequency domain for the complex amplitudes for elevation and pressure to obtain the steady-state solution. The solution is sought for in the form

$$\{F_{wave}, p, q, h\} = Re\{\{\tilde{F}, \tilde{P}, \tilde{Q}, \tilde{H}\} e^{i\omega t}\} \quad (4.3)$$

where $q(t)$ is the volume flow. We recall that the radiation force can be represented in the frequency domain as is given in equation 3.31. By inserting the above solutions and dividing the exponent term out and rewriting them, the steady-state solutions of the equations of motion can be given by the following equations as

$$\tilde{H} = \frac{\tilde{F}(\omega)}{-\omega^2 \left(\rho_w B + \frac{m_a(\omega)}{L} \right) + i\omega \left(\frac{B_r(\omega)}{L} + \frac{BA}{L} \Lambda \right) + \frac{\rho_w g A}{L}} \quad (4.4)$$

$$\tilde{P} = \Lambda \tilde{Q} = i\omega \Lambda B \tilde{H} \quad (4.5)$$

$$\Lambda = \left(\frac{K_1}{\rho_a} + \frac{i\omega B h_{air}}{\rho_a c^2} \right)^{-1} \quad (4.6)$$

where the forcing term here has been simplified as $\tilde{F}(\omega) = A_{inc} F_{wave}(\omega)/L$, where $F_{wave}(\omega)$ is the aforementioned wave excitation, consisting of the Froude-Krylov and diffraction forces. The force excitation coefficients obtained from AQWA are proportional to the incident wave amplitude indicated as A_{inc} . All coefficients from AQWA have been divided by the depth of the structure in y-direction d . Equation 4.4 and 4.5 give respectively the complex amplitude for the steady-state vibration of the elevation and air pressure inside the chamber. Please note that these solutions are not dependent on any initial conditions.

Finally, the time-averaged power amplitude is given by

$$\bar{P}_t = \frac{K_1}{2\rho_a} |\tilde{P}|^2 \quad (4.7)$$

Now the system has been solved in the frequency domain. The above analytical expressions for the complex amplitudes of elevation, pressure and power are further discussed in the remainder of this chapter.

4.2. Natural frequency analysis

The essential design characteristic of the Ocean Falls OWC is the natural frequency. Generally, for coupled systems the undamped natural frequencies are given by solving the characteristic equation given by

$$\det [\mathbf{K} - \omega^2 \mathbf{M}] = 0 \quad (4.8)$$

where, \mathbf{K} , \mathbf{M} and ω are the stiffness matrix, mass matrix and the natural frequency, respectively.

Let us consider the case of the Ocean Falls with open chamber conditions, meaning the turbine damping and compression of air is not considered, which means the thermodynamic equation is disregarded. In this scenario, the elevation inside the chamber is given by the oscillations of a single degree of freedom oscillating mass. The undamped natural frequency for such a system is given by

$$\omega_n = \sqrt{\frac{\rho_w g A / L}{\rho_w B}} = \sqrt{\frac{g A}{L B}} \quad (4.9)$$

The natural frequency for a single degree of freedom, axis-symmetric conventional oscillating water column, as described in Evans and Porter [24] is given by

$$\omega_n = \sqrt{\frac{g}{l}} \quad (4.10)$$

where g and l are respectively the gravitational acceleration and the draft of the OWC. In this simple case, the stiffness is given by the hydrostatic stiffness characterised by the geometry of the chamber and the mass is equal to the mass of the oscillating water column. Note here that no hydrodynamic added mass and radiation damping coefficients are included, but these can be approximated empirically like in Veer et al. [39] and Sheng et al. [40]. Clearly, the natural frequency of the Ocean Falls is different when compared to conventional OWC systems. Essentially, the oscillating water mass in the Ocean Falls is the mass in the tube, contrary to conventional OWCs, where that mass is the mass column in the chamber. This difference significantly changes the behaviour of the natural frequency for given geometry parameters.

Now, also considering the thermodynamics of the system and the damping terms in the equations of motion, we can derive an effective natural frequency for the system. Combining and elaborating equations 4.4, 4.5 and 4.6 effectively reduces the system to a mass spring damper system with augmented stiffness and damping terms given as

$$k_{eff} = \frac{\rho_w g A}{L} + \frac{\omega^2 \frac{B A}{L} \frac{B h_{air}}{\rho_a c^2}}{\left(\frac{K_1}{\rho_a}\right)^2 + \omega^2 \left(\frac{B h_{air}}{\rho_a c^2}\right)^2} \quad (4.11)$$

$$b_{eff} = \frac{B_r(\omega)}{L} + \frac{\frac{B A}{L} \frac{K_1}{\rho_a}}{\left(\frac{K_1}{\rho_a}\right)^2 + \omega^2 \left(\frac{B h_{air}}{\rho_a c^2}\right)^2} \quad (4.12)$$

where k_{eff} and b_{eff} are respectively the effective stiffness and damping. Firstly, considering the effective stiffness term it is clear that the air compressibility inside the chamber acts like a spring. For increasing air chamber height h_{air} the air compressibility also increases. Interesting is to note that the turbine characteristics also influence this spring term, since K_1 is in the denominator of the effective stiffness term. The addition of PTO damping acts in a similar way. On the condition that K_1 is always larger than 0, the addition of a turbine into the system increases the effective damping, as expected, since energy needs to be extracted from the system. Here it is important to note that K_1 is inversely proportional to the damping of the system. In other words, larger K_1 gives less damping.

With the new definitions in equations 4.11 and 4.12, the system is now considered as a single degree of freedom mass with an effective spring and an effective damper. The damped natural frequency for such a system is given by

$$\omega_{n,eff} = \omega_0 \sqrt{1 - \zeta_{eff}(\omega)^2} \quad (4.13)$$

with

$$\zeta_{eff} = \frac{b_{eff}(\omega)}{2\sqrt{k_{eff}(\omega)m(\omega)}} \quad (4.14)$$

$$\omega_0 = \sqrt{\frac{k_{eff}(\omega)}{m(\omega)}} \quad (4.15)$$

where $m(\omega)$ is the mass term including the frequency dependent added mass. The terms ζ_{eff} and ω_0 are respectively the effective critical damping and undamped natural frequency. Equation 4.13 is solved iteratively to obtain the effective natural frequency of the system for various geometry and turbine parameters. Based on the natural frequency equations stated above, increasing the chamber width B of the system will also increase the natural period.

4.3. Model validation

Important is to validate the model for some conditions to check whether the model corresponds to what is expected in reality. This section presents some hypothetical cases to discuss the result the model gives for these cases and to check whether or not it is well aligned to what is expected. The hydrodynamic coefficients and excitation forces used in this section are for the first wall position. Please refer to appendix B for the numerical values used for the hydrodynamic coefficients.

4.3.1. Open air chamber

Firstly, let us try to recreate open chamber conditions, meaning that there is actually no chamber just an open box-like structure inside the water. Setting the value for the volume to a much larger value should resemble a system where there is no air chamber, meaning that Λ should tend to zero. Increasing the chamber height of the system to large values makes this possible. Figure 4.1 gives two graphs; left is the normalised elevation amplitude for a chamber width over chamber height ratio of $1e-10$ and right is the normalised pressure amplitude for the same case. From these, one can conclude that a sufficient increase in the chamber height indeed does cause the physics of the turbine and air compressibility to vanish in the system and causes the model to become just an oscillating mass in water. Similarly, the pressure amplitude vanishes because the pressure above the water is equal to the atmospheric pressure.

4.3.2. Closed air chamber

Decreasing the diameter of the turbine will cause the chamber to be enclosed more. Figure 4.2 below gives this case. As the turbine diameter tends to 0, the turbine damping parameter will also become 0 and the effective natural frequency will change, since the effective stiffness is being dominated by the air compressibility term. In reality, one would observe a non-linear behaviour of the air in the chamber as the IWS fluctuates, since the more one compresses a sealed chamber, the higher the pressure will be and thus the higher the resisting force will become. However, as mentioned in the previous chapter, the equations of motion have been linearised and so the air chamber volume is assumed not to be effected by the elevation inside the chamber.

4.4. Air compressibility analysis

This section contains the comparison between the Ocean Falls system with and without air compressibility.

4.4.1. Equations of motion without air compression

Let us now consider the case where the air compression inside the chamber is neglected. We can do this by simply negating the second term on the right hand side in equation 4.2 as

$$K_1 p = \rho_a B \dot{h} \quad (4.16)$$

Now we can rewrite the above equation and substitute it into the heave equation of motion in equation 4.1. Similar to the case with air compression, we look for the steady-state solution in the complex form like in equation 4.3. Note that only the Λ term changes with this case, all other terms remain the same. This gives us the complex heave and pressure amplitudes as follows

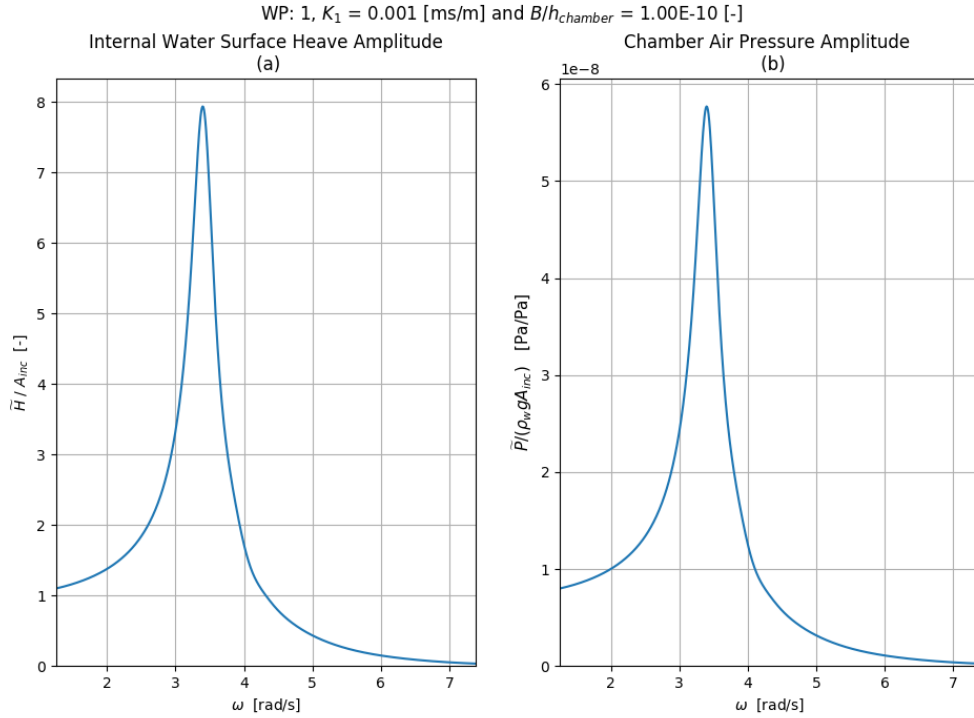


Figure 4.1: A graph of the heave and pressure amplitude for "open chamber" conditions.

$$\tilde{H}_i = \frac{\tilde{F}(\omega)}{-\omega^2 \left(\rho_w B + \frac{m_a(\omega)}{L} \right) + i\omega \left(\frac{B_r(\omega)}{L} + \frac{\rho_a B A}{K_1 L} \right) + \frac{\rho_w g A}{L}} \quad (4.17)$$

$$\tilde{P}_i = \Lambda \tilde{Q} = i\omega \frac{\rho_a B}{K_1} \tilde{H}_i \quad (4.18)$$

The following section gives the solutions in the frequency domain for the case with and without air compression.

4.4.2. Solutions in frequency domain

To clearly indicate the effect of the air compression term in the equations of motion, one has to change the ratio between the PTO damping and air compression terms. This is achieved by varying the turbine damping parameter and observing the solutions in frequency domain for both the heave and pressure. The same geometry used in the validation above is also used here.

Figure 4.3 gives the graphs for the solutions with and without the air compression term for varying turbine damping parameters K_1 . It is clearly visible that for high values of the turbine parameter K_1 , so systems with less damping, the inclusion of air compressibility does not have much effect. For more damped systems the difference becomes more visible. Additionally, both in the heave and pressure amplitudes the incompressible air cases give slightly larger values. This is more clear in the higher damped systems. Overall, the air compressibility term has little effect in the system for flume geometry conditions. Please note that air compressibility effects are generally significant for full-scale geometries. This is emphasized in depth in Falcão et al. [32].

4.5. Power response to regular and irregular waves

The ultimate aim of any wave energy converter is to generate electrical power through the waves. It is therefore evident that any optimisation or analysis should be done through the power yield of the model. This section will give the generated mechanical power for the Ocean Falls model for regular and irregular waves.

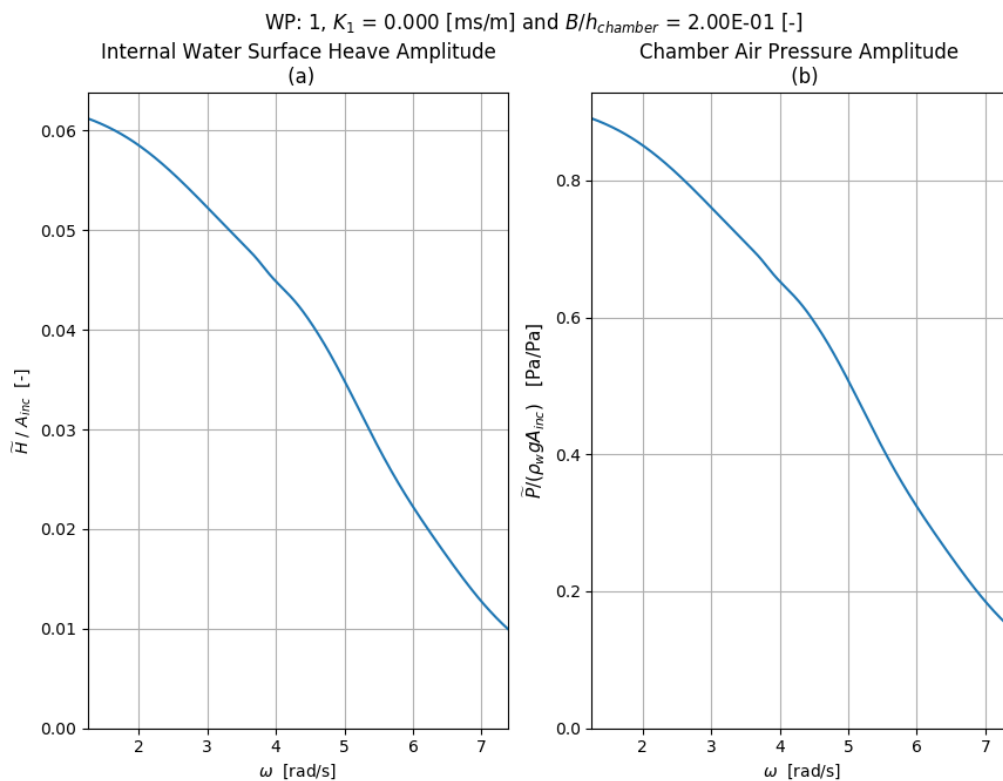


Figure 4.2: A graph of the heave and pressure amplitude for "closed chamber" conditions.

Furthermore, the efficiency will be given and also the turbine parameter will be optimised for the case without air compression. Please note that only the geometry of the Ocean Falls model in the flume has been used here, any optimisation is therefore done based on this geometry. The geometry specifics can be found in figure 5.8.

4.5.1. Power yield in regular waves

Previously, in this chapter the time-averaged power was given in equation 4.7. The power yield in regular waves per meter in y -direction for varying turbine parameters is given in figure 4.4. The maximum power is clearly given in at around the natural period of the system, which is expected. From the graph is clear that there is an optimum value for K_1 .

4.5.2. Power yield in irregular waves

The analysis of the Ocean Falls oscillating water column performance subject to irregular waves is modelled using a stochastic model as presented in Falcão et al. [41] and Gomes et al. [13]. The water level in the ocean is far from represented by a regular wave. However, a linear superposition of a large amount of regular waves with different frequencies and amplitudes is a much better approximation. This chapter briefly explains the method applied to obtain statistical representative functions of the dynamics and power performance of the Ocean Falls obtained through the frequency domain results presented above.

So, let us consider an irregular wave sea state, one that is represented by a linear superposition of regular sinusoidal waves with each of them having a distinctive frequency and amplitude. An essential assumption that needs to be stated here is that this approach implies that the free surface elevation in irregular waves is described as a stationary and ergodic process described by a Gaussian distribution. An ergodic process meaning a realisation of a sea state that, if it is averaged in time or space the results are the same as if it were averaged over an ensemble of realisations of the same process. This approach to modelling random waves is elaborately described in Holthuisen [42] and also has applications in many fields in offshore and coastal engineering.

The Gaussian probability density function of the free-surface is given by

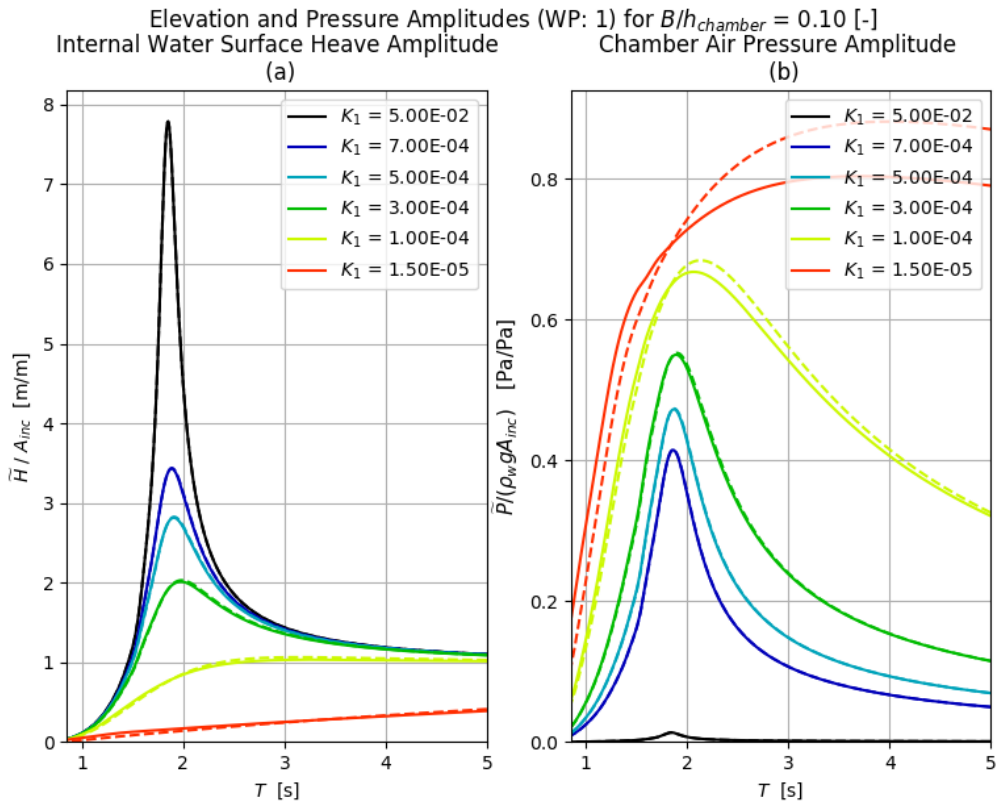


Figure 4.3: The heave and pressure amplitudes with and without air compression included for varying turbine damping parameter K_1 . The solid lines give the graphs for the solutions with air compressibility, the dashed lines give the graphs for the solution without air compressibility.

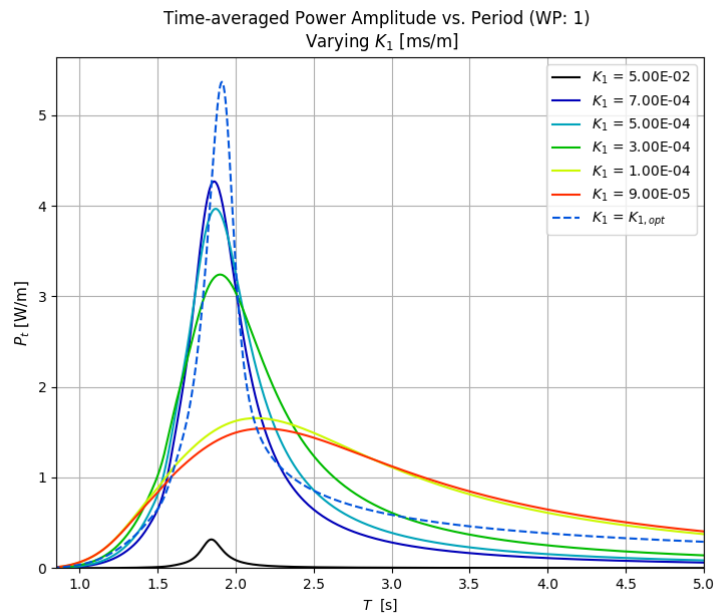


Figure 4.4: A graph of the time-averaged power amplitude for constant turbine parameters.

$$f_{\text{pdf}}(\zeta) = \frac{1}{\sqrt{2\pi}\sigma_\zeta} \exp\left(-\frac{\zeta^2}{2\sigma_\zeta^2}\right) \quad (4.19)$$

where ζ and σ_ζ is the free surface elevation and its standard deviation, respectively. The variance of a spectrum is given by

$$\sigma_\zeta^2 = \int_0^\infty S_{\zeta\zeta}(\omega) d\omega \quad (4.20)$$

where $S_\omega(\omega)$ is the energy density spectrum of the irregular sea state. Let us consider a standard JONSWAP spectrum to describe this energy density spectrum given by the following formula

$$S_{\zeta\zeta}(\omega) = \frac{320H_{1/3}^2}{T_p^4} \omega^{-5} \exp\left(\frac{-1950}{(T_p)^4} \omega^{-4}\right) \gamma^{\alpha(\omega)} \quad (4.21)$$

where $H_{1/3}$, T_p , ω , and γ is the significant wave height, peak period of the spectrum, wave excitation frequency in radians per second and peakedness factor, respectively. The term α and the step-function β are given by

$$\alpha(\omega) = \exp\left(-\left(\frac{\frac{\omega}{2\pi/T_p} - 1}{\beta\sqrt{2}}\right)^2\right) \quad (4.22)$$

$$\beta = \begin{cases} 0.07 & \text{if } \omega < 2\pi/T_p \\ 0.09 & \text{if } \omega > 2\pi/T_p \end{cases} \quad (4.23)$$

The comprehensive study behind the JONSWAP spectrum definition given above can be found in Hasselmann et al. [43]. Now that we have defined the irregular wave spectrum we can define the response of the system heave and pressure to this irregular wave spectrum in terms of spectral density. Based on the fact that the system is linear and ζ is given by a Gaussian probability density function it means that the response can be described also as a Gaussian probability density function. A derivation for this is given in Journée et al. [44] in chapter 6. In line with the approach taken in Falcão and Rodrigues [41] and approach taken in Gomes et al. [13], we can define the heave and pressure standard deviation in irregular waves as

$$\sigma_h^2 = \int_0^\infty S_{\zeta\zeta}(\omega) \left| \frac{\tilde{H}(\omega)}{\zeta_a} \right|^2 d\omega \quad (4.24)$$

and similarly for pressure

$$\sigma_p^2 = \int_0^\infty S_{\zeta\zeta}(\omega) \left| \frac{\tilde{P}(\omega)}{\zeta_a} \right|^2 d\omega \quad (4.25)$$

where ζ_a is the incident wave amplitude and \tilde{H} and \tilde{P} are the complex transfer functions for respectively heave and pressure.

Similarly, recalling equation 3.30 the time-averaged power for a random sea state can be given by

$$\bar{P}_{t,irr} = \frac{k_1}{\rho_a} \sigma_p^2 \quad (4.26)$$

where σ_p is the standard deviation for the pressure response in irregular waves. Note here that k_1 is given in m·s meaning the above given equation for power is in W.

4.5.3. Capture width and efficiency

This section gives the definitions for the power in waves for regular and irregular waves. Furthermore, the definitions used for capture width and efficiency are given. Finally, a comparison is made between the efficiency of the Ocean Falls in regular and irregular waves.

The time-averaged power per meter wave crest in regular waves can be derived by defining the potential and kinetic energy in waves and summing them up. The derivation will not be provided here but can be found adequately described in Holthuijsen [42]. The time averaged wave energy flux per meter wave crest for regular waves is given by

$$\bar{J} = \frac{1}{2} \rho_w g \zeta_a^2 c_g \quad (4.27)$$

where ζ_a is the wave amplitude and c_g is the group velocity of the waves given by

$$c_g = \frac{\omega}{2k} \left(1 + \left(\frac{2kh}{\sinh(2kh)} \right) \right) \quad (4.28)$$

where ω , k and h are respectively the wave frequency, wave number and water depth. For irregular waves this becomes slightly different. The time averaged wave energy flux for irregular per meter crest is calculated through the sum of the power per meter crest of each regular wave component over the range of the random energy density spectrum. Again following Gomes et al. [13] the wave energy flux in irregular waves per meter wave crest can be given by

$$\bar{J}_{irr} = \sum \bar{J}(\zeta_a(\omega)) \quad (4.29)$$

where ζ_a is the wave amplitude of a single component and is given by

$$\zeta_a = \sqrt{2S_\omega(\omega)d\omega} \quad (4.30)$$

where S_ω is the random wave energy density spectrum and $d\omega$ is a frequency interval, which will give smoother results if set smaller. It is common to give the ratio between the hydraulic power and the power in the waves in terms of capture width in units meters. The capture width is defined as

$$L_c = \frac{\bar{P}_t}{\bar{J}} \quad (4.31)$$

where \bar{P}_t is the hydraulic power (power available to turbine) in W and \bar{J} is the wave energy flux per meter wave crest in W/m . A slightly preferred approach to this is by giving the efficiency which is simply the capture width divided by the device width, which is in this case equal to the width of the wave flume d_{flume} . Note here that the width of the chamber is slightly smaller to the width of the wave flume; $d < d_{flume}$. The efficiency can now be given as

$$\eta = \frac{\bar{P}_t}{\bar{J}d_{flume}} \quad (4.32)$$

Similarly, for the case of irregular waves the equation does not change, only the subscript 'irr' is added to both hydraulic and wave power. Figure 4.5 gives a graph of the efficiencies as defined above for irregular waves. The efficiency for the irregular waves is given in terms of the peak period of a JONSWAP spectrum, T_p , not to be confused by a range of frequencies employed to determine the efficiency in regular waves. The peakedness factor has been varied in the irregular wave case to evaluate the change in efficiency for wider spread JONSWAP spectra. This analysis can be applied to cases with other types of spectra like Bretschneider and Pierson-Moskowitz, depending on the design parameters of the device. Clearly, a significant drop in efficiency is visible in the case of irregular waves compared to the efficiency in regular waves. This reduction is circa 40% - 50%.

Let us note here that equation 4.21 is only valid for JONSWAP wave growth for a given wind speed. For arbitrary combinations of $H_{1/3}$ and T_p the "320" coefficient needs to be adjusted. To check the validity of this equation, the $H_{1/3}$ obtained through the $H_{1/3} = 4\sqrt{m_0}$ relation has been compared to the arbitrary chosen one. The significant wave heights differ for various spectra at low and high peak periods, but are equal at resonant periods, and will therefore not change the results significantly. At low and high peak periods the efficiency will be slightly higher than depicted in figure 4.5.

4.5.4. Optimum turbine parameter

Previously, the turbine parameter was defined in terms of turbine diameter and turbine rotational speed. In practice it is possible to apply some control to the turbine by manipulating the rotational speed. This fact suggests that the turbine can perhaps be modified in real time for various incoming frequencies. This section contains the derivation for an optimised turbine parameter K_1 .

Let us first consider the system without any air compressibility. The solutions to the equations of motion reduce to equations 4.17 and 4.18. The complex power can be given by multiplying the damping parameter

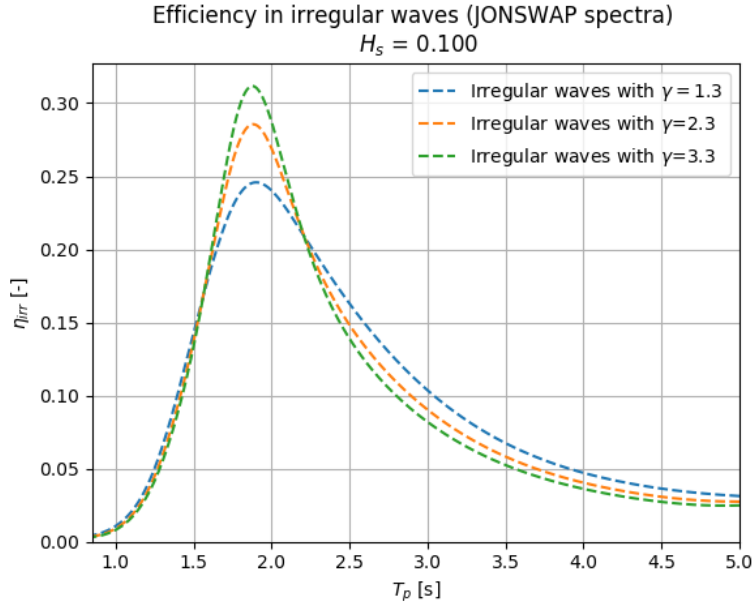


Figure 4.5: Capture width divided by flume width for irregular waves with $K_1 = 7E - 4 \frac{ms}{m}$ and varying peakedness factor γ .

divided by the air density multiplied by the complex pressure amplitude squared. Elaborating this gives us the time averaged power as

$$\bar{P}_t = \frac{K_1}{2\rho_a} \left(i\omega \frac{\rho_a}{K_1} B \left(\frac{\tilde{F}(\omega)}{-\omega^2 \left(\rho_w B + \frac{m_a(\omega)}{L} \right) + i\omega \left(\frac{B_r(\omega)}{L} + \frac{BA}{L} \frac{\rho_a}{K_1} \right) + \frac{\rho_w g A}{L}} \right) \right)^2 \quad (4.33)$$

Let us now derive this equation with respect to K_1 and set it to zero. Rewriting this by moving K_1 to the left side and all other terms to the right side gives us the optimum turbine damping parameter in terms of frequency. The optimal value for K_1 regarding power yield for a given geometry is

$$K_{1,opt} = \frac{i\omega \rho_a B A / L}{-\omega^2 \left(\rho_w B + \frac{m_a(\omega)}{L} \right) + i\omega \left(\frac{B_r(\omega)}{L} \right) + \frac{\rho_w g A}{L}} \quad (4.34)$$

One can state based on equation 4.34 that the PTO damping term is optimally equal to the denominator of the complex amplitude of the elevation. So, when the PTO damping term is equal to the summation of the mass, radiation damping and stiffness terms in the denominator, it is optimal. This is in accordance with, among other examples, Rezanejad et al. [45].

Figure 4.6 gives a efficiency plot of the case with a fixed and optimum PTO damping case. One can clearly state that the optimum turbine increases the peak efficiency. However, the peak does become slightly narrower and shifts slightly to a higher resonant period.

4.6. Conclusions

This chapter has presented the solutions to the dynamic system for regular waves, irregular waves and varying turbine parameters for the flume model geometry. This section gives an overview of the chapter and highlights some key points.

- Parameters have been used as input in the system to simulate respectively 'open' and 'closed' chambers. Results for an open chamber give low pressure amplitudes and undamped heave amplitudes in line with what is expected. Similarly for a closed chamber the heave amplitude is highly damped and pressure amplitudes give larger values, as expected.
- The influence of air compression has been studied in the model. For low turbine damping systems the air compression has little to no effect on heave and pressure amplitudes. If the turbine damping is increased the effect of compressibility is significant, as it gives a slightly increased values with respect to

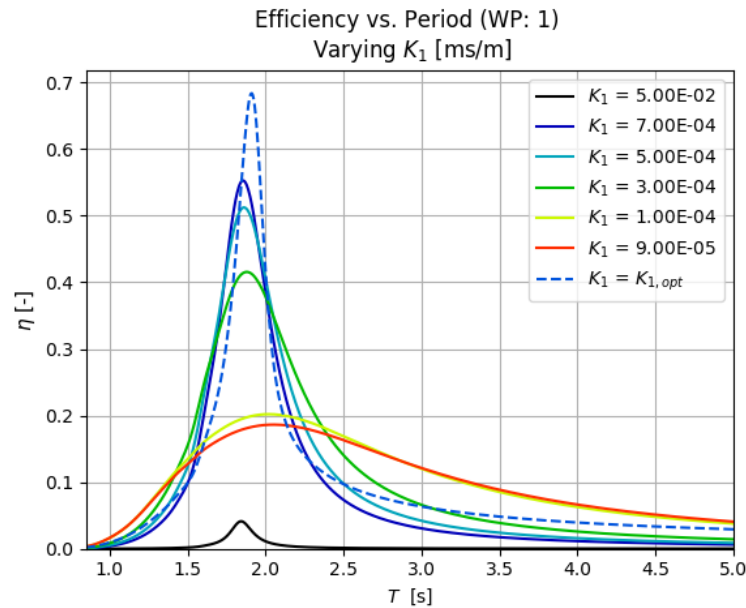


Figure 4.6: Efficiency of the system for fixed and optimum K_1 for regular waves.

the model without air compressibility for both heave and pressure amplitudes, where this difference is more evident in the latter.

- Efficiency has been defined as the capture width of the system divided by the total width of the device in the flume, approximately equal to the flume width d_{flume} . For regular waves, the maximum achieved efficiency is around 55% occurring at a slightly lower period than the heave resonant peak. JONSWAP spectra have been employed to input irregular waves into the system. In irregular waves the efficiency drops to 25% - 31% for various values of the peakedness factor γ in the JONSWAP spectrum.
- Finally, the turbine parameter has been assumed to be able to vary in the frequency domain giving rise to be able to find an optimum. For the case of the model without air compressibility, the optimum turbine damping coefficient has been derived as a function of frequency. In regular waves, the optimum turbine parameter increases the maximum efficiency to circa 68%.

5

Experiment Methodology

An experimental program has been executed with the purpose of analysing the hydrodynamic response of the Ocean Falls to incoming regular waves. The experiments consist of test preparation, calibration of incident wave heights and frequencies and finally performing the actual experiments. This chapter gives a comprehensive explanation of the performed experiments.

5.1. Test objective

The objectives of the model experiments are to:

- assess the wave reflection and transmission coefficients of the Ocean Falls structure;
- determine and assess the internal water surface elevation and chamber pressure for regular waves;
- assess the dynamic response of internal water surface elevation and chamber pressure for a variation of the back wall position;
- and determine and assess the hydraulic power and efficiency of the system.

The above mentioned items have been performed for two different wall positions and two different turbine damping scenarios.

5.2. Description of the test facility

The 2D physical modelling has been carried out in the BAM Infraconsult wave laboratory in Utrecht. The wave flume of BAM Infraconsult in Utrecht consists of a long rectangular glass tank with a wave generator on one side. The flume has a length of 25 m, a width of 0.6 m and a height of 1.0 m. The maximum permissible water depth is 0.7 m with a maximal wave height of 0.3 m. The flume is equipped with the Edinburgh Designs piston wave generator, which can generate regular and irregular waves. The Edinburgh Designs piston wave generator is able to correct the paddle motion to absorb the reflected wave. The incoming and reflected wave fields in front of the structure to be investigated are measured by resistance wave gauges. The reflection analysis is based on the method of Mansard and Funke [46] for which the WaveLab software (Aalborg University) has been applied. Time series of water level elevations have been recorded at a frequency of 32Hz which is sufficient for the purpose of wave analysis. The flume is composed by windows on both sides through which the generation and development of the waves can be observed as well as their interaction with the structure. In addition, videos and photos can be recorded and made through these windows. This above description has been taken from BAM Infraconsult engineering reports. Figure 5.1 gives an image of this flume.

5.3. Experiment set-up

This section contains some key aspects on the approach to performing the experiments.

5.3.1. Model bathymetry

The model experiments will be performed in constant water depth and therefore no foreshore is needed. A constant water depth of 0.5 m is used during the entire extent of the experiments.

DMC Wave Flume (Utrecht)

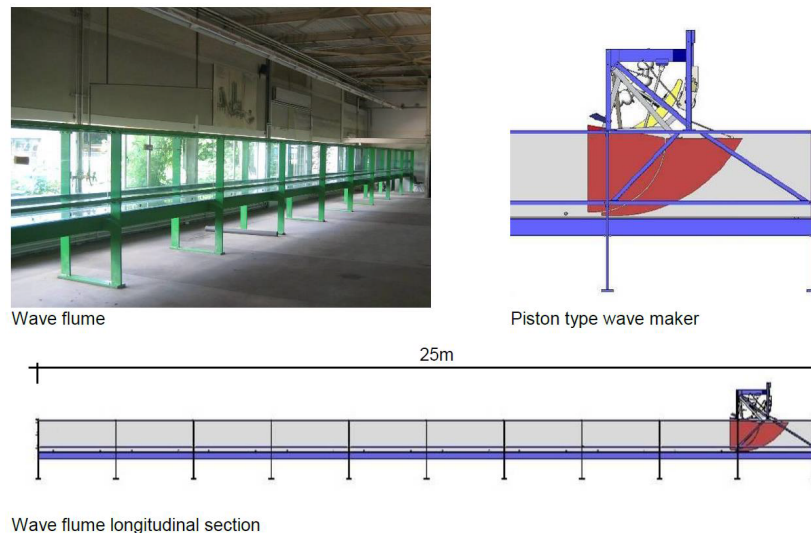


Figure 5.1: An image of the DMC wave flume located in Utrecht. This image has been taken from BAM Infraconsult engineering reports.

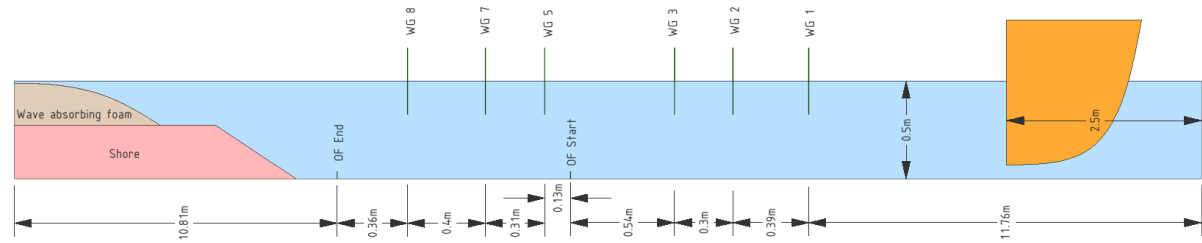


Figure 5.2: Schematic view of the wave flume during calibration runs. The abbreviation "WG" stands for wave gauge.

5.3.2. Wave calibration

Before the experiments of the Ocean Falls, the test conditions have been calibrated. This calibration is necessary to ensure that the desired design wave conditions are accurately produced at the required location. In this case the target waves are calibrated in front of the wave paddle as the offshore wave height is provided. During the calibration runs, an absorbing foam has been placed at the extreme end of the flume in order to minimize reflections against the rear end of the flume. Wave gauges have been placed in deep water and at the location of the entrance of the Ocean Falls. The wave gauges in deep water have been used to compare the deep water waves during the calibration runs with the deep water wave conditions during the test runs. The locations of the wave gauges during the calibration runs can be seen in figure 5.2. During the calibration runs, the target wave heights can be achieved by slowly incrementing a gain factor which multiplies the amplitude of the wave signal. For the Ocean Falls experiments in regular waves, however, it does not matter what the incident wave height is as long as the calibration and normal runs are consistent. The most important addition of these runs is the possibility to compare incident wave amplitudes between runs with and runs without the structure in the flume. The incident amplitudes for both cases should be similar. Figures 5.3 and 5.4 give some pictures of the set-up taken during experiments.

5.3.3. Model scaling

The scale for the experiments is chosen based on:

- the prototype structure geometry;
- whether the required wave conditions can be produced by the wave maker;
- whether the structure will fit into the wave flume without disrupting the ratios between geometric



Figure 5.3: Pictures taken during wave experiments.

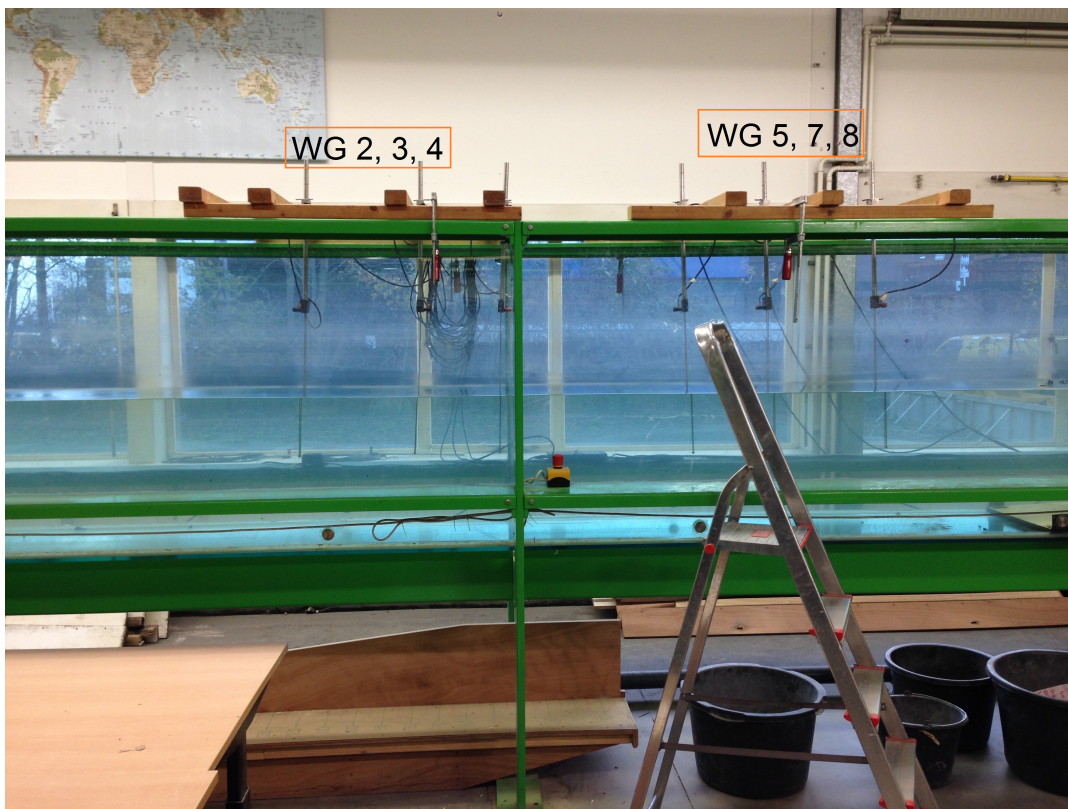


Figure 5.4: Pictures of the calibration experiments set-up.

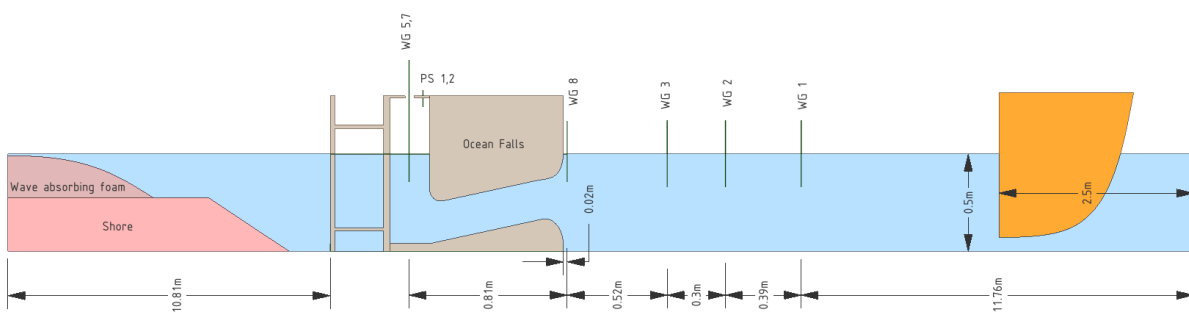


Figure 5.5: Schematic view of the wave flume during runs including the structure. The abbreviation "WG" and "PS" stand for wave gauge and pressure sensor, respectively.

lengths;

- and whether the wave heights and internal water surface elevation can be measured accurately.

The scale used in the experiments has been based on Froude scaling, where the Froude number is kept constant. The Froude number is given by

$$Fr = \frac{U}{\sqrt{gD}} \quad (5.1)$$

where U , g and D are respectively the velocity, gravitational acceleration and water depth, not to be confused with the turbine diameter, also depicted as D . With this condition, the Froude number in the prototype and model scales must be equal. This is needed to compare model and prototype wave periods. The scaling factor for this experiment is chosen to be $\epsilon = 30$. Based on Froude scaling, the time will scale with a square root, so the scaling factor of time will be equal to $\sqrt{30} = 5.47$.

5.3.4. Regular waves

The structure is tested in the flume for regular waves. The set-up for these runs is given in figure 5.5. The experiments contain tests for periods varying from $T = 5.0s$ to $T = 0.85s$ with corresponding wave lengths $\lambda = 10.9m$ to $\lambda = 1.12m$. These chosen values are derived from realistic values in prototype scale. The chamber widths considered are $B = 0.2m$ and $B = 0.25m$, meaning the assumption with regard to wavelength to chamber width ratio is valid. Also, to stay in line with the assumptions of linear wave theory, a fixed incident amplitude of 3 cm is used (low wave steepness). Appendix D gives an overview of the test program.

5.3.5. Thermodynamics in the air chamber

The numerical model, as stated in chapter 3, contains the compression of air inside the chamber. However, to satisfy the similitude of the compression of air in the chamber in model and prototype scale, one would also need to scale the atmospheric pressure with it, which is practically impossible unless ϵ is circa 1. A more realistic approach to scaling the compression is to assume the atmospheric pressure is equal in both model and full scale. This approach results in scaling the volume with ϵ^2 instead of ϵ^3 , according to Falcão et al. [15] and Forestier et al. [47]. This complication combined with the relatively small effect of air compressibility in the linear model for the flume model geometry, makes it convenient to disregard the compressibility of the air, simplifying the equations of motion. The effect of the air compression is thus not analysed in the experiments. Please refer back to chapter 3 to review the derivation.

Another important part of the model experiments is the damping of the turbine. Even in the largest wave tanks a model scale of approximately 1:10 can be achieved, meaning a maximum power ratio of 1:3200, according to Falcão et al. [32]. This scale is extremely small to create a ‘mini’ turbine to include in model experiments. Alternatively, the OWC can be sealed with a lid that contains a small opening. As the water column oscillates the lid will induce some damping on the system, proportional to the area of this orifice. The relation between the pressure drop and the flow through this opening is quadratic and is used to model bi-radial turbines that have a similar relation between pressure and flow. Since the model described in chapter 3 assumes a linear turbine, using an orifice necessitates a linearisation of this quadratic relation. The following chapter further elaborates the processing of data.

As mentioned before, there are two different damping cases considered; "Low" and "High" damping. Figure 5.6 gives a schematic top view of the air chamber lid that has been used during the experiments. The pictures taken of the lid can be found in figure 5.7. Table 5.1 gives the level of damping expressed in orifice area to total area ratios for each experiment case.

Table 5.1: Damping levels computed by dividing the orifice area by the total area of the water surface.

PTO Damping	Orifice area ratios	
	B/L=0.34	B/L=0.42
Low	0.0268	0.0216
High	0.0169	0.0137

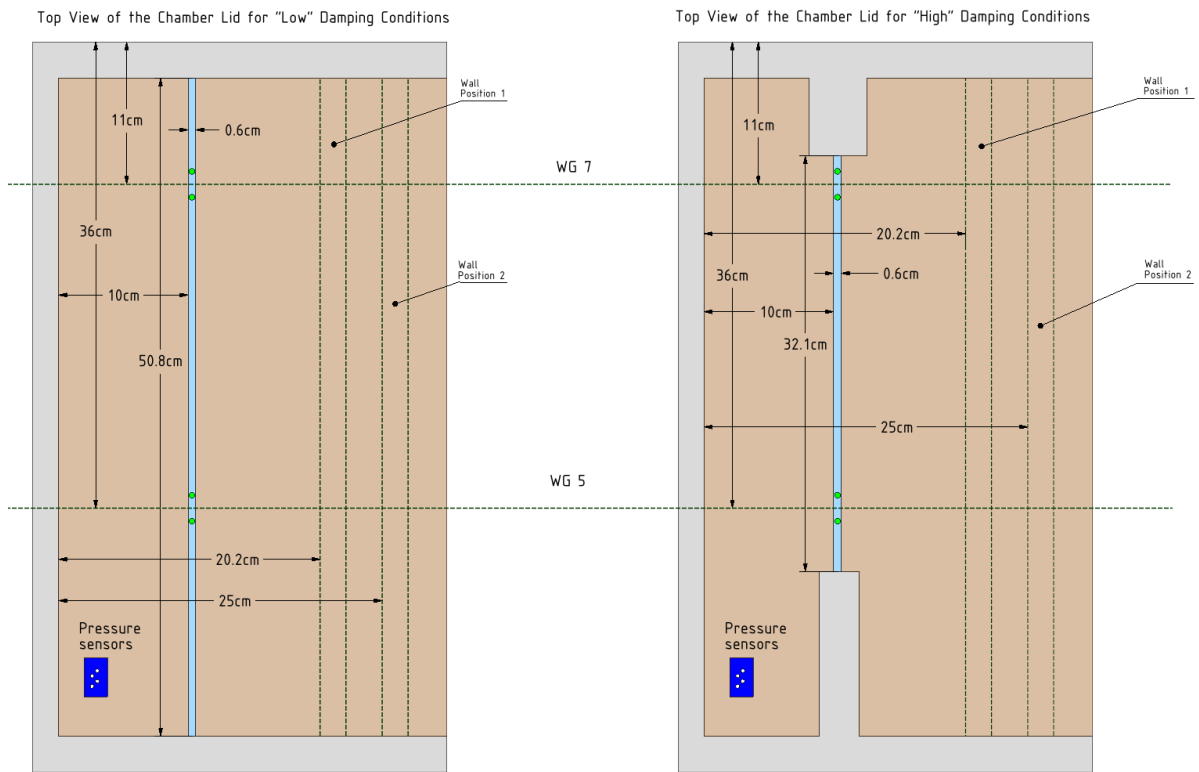


Figure 5.6: Schematic top view of the air chamber lid used for both low and high damping cases. The dashed vertical lines indicate where the back wall positions are.

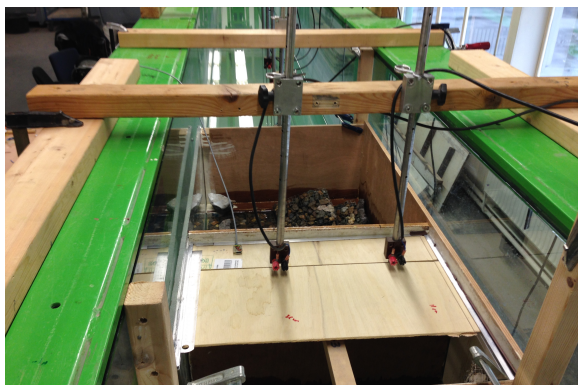


Figure 5.7: Pictures of the PTO damping lid.

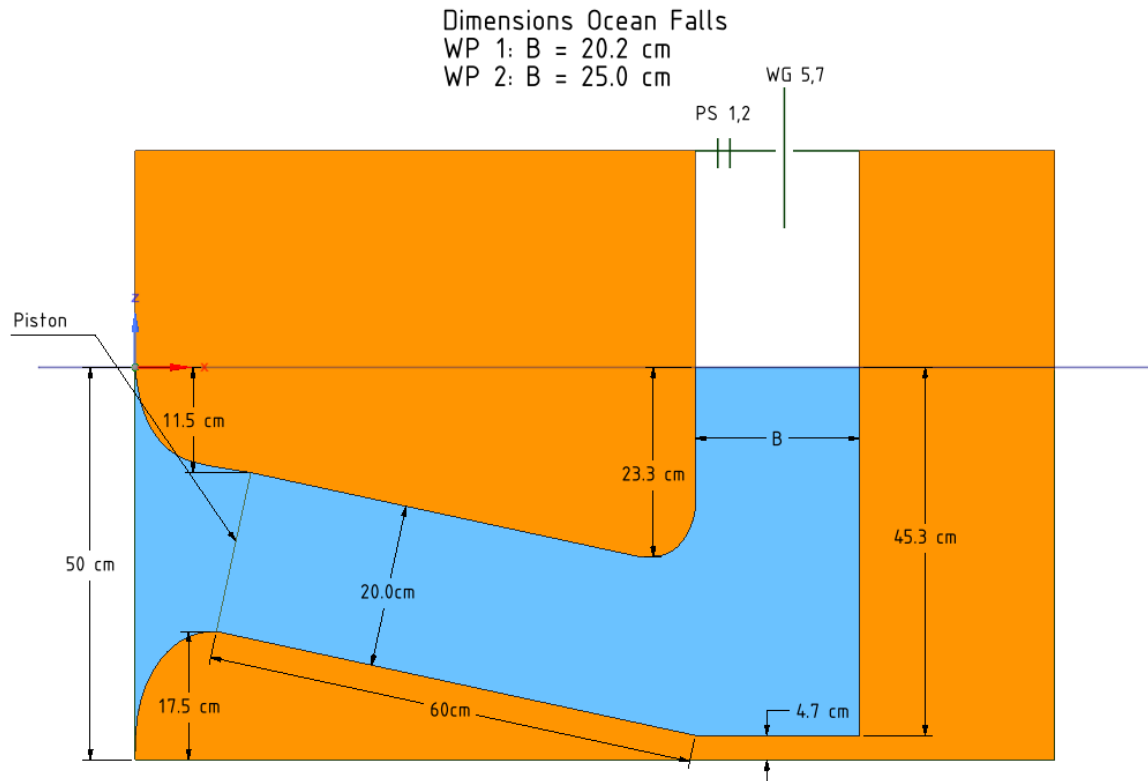


Figure 5.8: Geometry of the Ocean Falls model. This cross section is identical to the model used in AQWA. Appendix B

5.3.6. Cross section and model geometry

The cross section drawings are given in figure 5.8. The structure is built using wood and plexiglass and is connected together using screws and glue. Figure 5.9 gives a picture taken of the Ocean Falls structure during an experiment run with PTO damping.

5.3.7. Set-up of wave gauges, air pressure sensors and camera

The wave gauge equipment used is the Edinburgh Designs WG8USB Wave Gauge Controller. This controller contains input measurements from wave probes that measure the resistance determined by the height of the water elevation. These gauges are robust and simple to use with full scale error of less than 0.1% [48]. However, given the fact that the wave gauge disturbs the water surface during the presence of waves and that the wet surface of the gauge will have a slightly increased conductivity, the uncertainties will be slightly higher. To be able to use these gauges accurately, they need to be calibrated before each set of runs by adjusting the height for a fixed length.

The air pressure sensors that are used are the Smartec SPD102DAhyb ones, developed and manufactured by Smartec. These sensors have an accuracy of 2.2% of the full span of the sensor, which is 100 mmH₂O. Two samples of this sensor have been granted free of charge to this study by Heynen B.V.. These sensors measure the pressure in the chamber with respect to the pressure in the atmosphere. Therefore two cylinders are placed on each sensor, where one cylinder is connected with a blue plastic pipe to the atmosphere and the other is kept in place. See figures 5.10 and 5.11. The pressure sensors have been connected to a laptop through the National Instruments USB-6008 Multifunction I/O Device. This device enables the pressure sensor measured voltage to be translated to data on a computer. The data acquisition system is written in NI LabVIEW by TU Delft employee Jos van Driel. The data sheets for the sensors and interface with an image of the LabVIEW diagram and front panel can be found in appendix C.

Additionally, a camera is placed facing the flume from the side at the location of the Ocean Falls to film the dynamic effects inside the chamber and before the structure. Appendix C gives an overview of the measuring equipment in more detail.

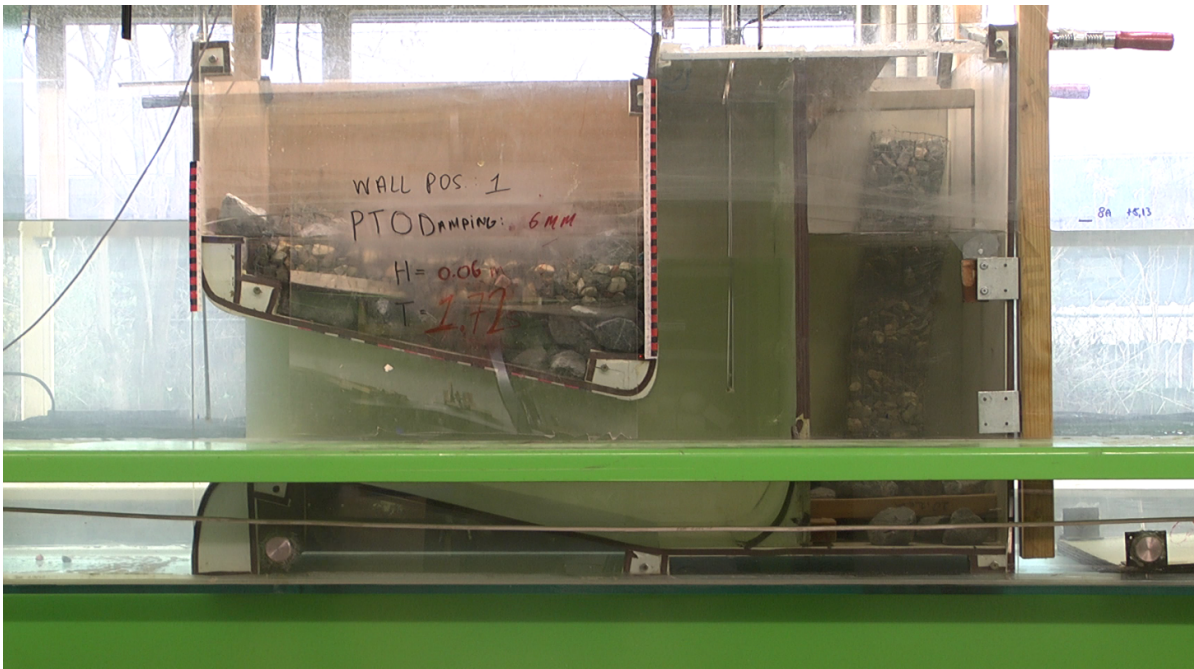


Figure 5.9: The Ocean Falls during an experiment run with PTO damping.



Figure 5.10: Pressure sensor on the damping lid of the system.



Figure 5.11: Pressure sensor and the interface device used for the data acquisition. Each sensor contains two cylinders to measure the difference in pressure between them. One of these is connected to the atmosphere while the other measures the air pressure in the chamber.

5.4. Experiment program and protocol

The experiments performed are in the order of calibration runs and then runs including the structure for respectively no turbine damping, low turbine damping and high turbine damping. This sequence is repeated for a second back wall position with the exception of running the calibration runs again. In appendix D an overview of the performed runs is given in more detail. A brief list of the steps taken to perform the experiments is also given in appendix D.

5.5. Summary

This chapter gave an explanation of the methodology that has been used in the experiments. Some key points to underline are given below.

- Regular wave experiments are performed for the Ocean Falls for damped and undamped cases. Calibration runs have also been performed to compare incident wave amplitudes of runs with and without the structure in the flume.
- Model and prototype similarity is scaled by keeping the Froude number constant. A scaling factor of $\epsilon = 30$ is used.
- The air compressibility in the chamber is disregarded because of scaling issues combined with the fact that it has little influence in the linear model for flume model geometries.
- The PTO damping is modelled as an orifice in the lid of the air chamber. The area of opening is proportional to the amount of damping. Pressure sensors have been placed inside the chamber to measure and quantify this damping.

6

Experiment results and comparison to theory

This chapter gives the results obtained from the experiments and their comparison to the theoretical model.

6.1. Wave reflection analysis

Before we look into the comparison of theoretical model and the experiments, let us consider the reflection of waves in the flume and also the reflection of the Ocean Falls structure. If we recall the previously mentioned experimental runs performed in the flume, we had: the calibration runs performed in an empty flume and then the runs with the structure included. The reason the calibration runs have also been performed in the flume is to determine whether the reflection analysis with and without the structure is similar and also to tune the real desired wave heights, since what the user inserts into the wave generator software is not exactly reproduced in the flume. Secondly, the experiment runs were performed including the structure.

6.1.1. Mansard & Funke method

The measured data during the experiments has been decomposed into reflected and transmitted waves using the WaveLab 3 program developed by Aalborg University [49]. The method employed in this program is the Mansard & Funke method [46]. This method decomposes the waves into an incident wave, reflected wave and an extra noise term. Contrary to this method, the previous Goda & Suzuki [50] method splits the data into only incident and reflected components and utilises only two wave gauges, whereas the Mansard & Funke method uses three. Through analytical expressions the Mansard & Funke method can determine the incident and reflected waves and also with the addition of the third wave gauge minimise the noise component in the least squares sense. To do this the user has to measure the elevation using the three wave gauges placed in close proximity to each other and in series on one line. These gauges need to measure simultaneously.

6.1.2. Incident wave amplitudes

Let us now consider all wave gauges in the calibration runs and the first three wave gauges in all the runs including the structure in the flume. Please refer to chapter 5 for schematics of the locations of the wave gauges. Using WaveLab 3, reflection analyses have been employed to these gauges to determine the incident and reflected wave amplitudes. Before considering the results, the expectations should be mentioned of these analyses. Firstly, one expects the incident wave amplitudes to not differ much between all the runs mentioned above. This expectation is due to the fact that the reflection analysis employed determines the reflection coefficient, with and without structure, and determines the incident wave amplitude. Note here that the measured data has not been filtered for this analysis. Figures 6.1 and 6.2 give all the incident wave amplitudes determined through WaveLab 3 for both wall positions with unfiltered data.

Based on these figures one can say that there is a difference in incident wave amplitudes of the different wave runs, especially at longer periods. At shorter periods the differences are fairly small. For long periods the difference becomes more significant and should be kept in mind when reviewing the results below. Additionally, the experiments with $B/L = 0.42$ give slightly more deviating results for the incident wave amplitudes, especially between calibration and normal runs compared to the $B/L = 0.34$ case. Here B and L respectively

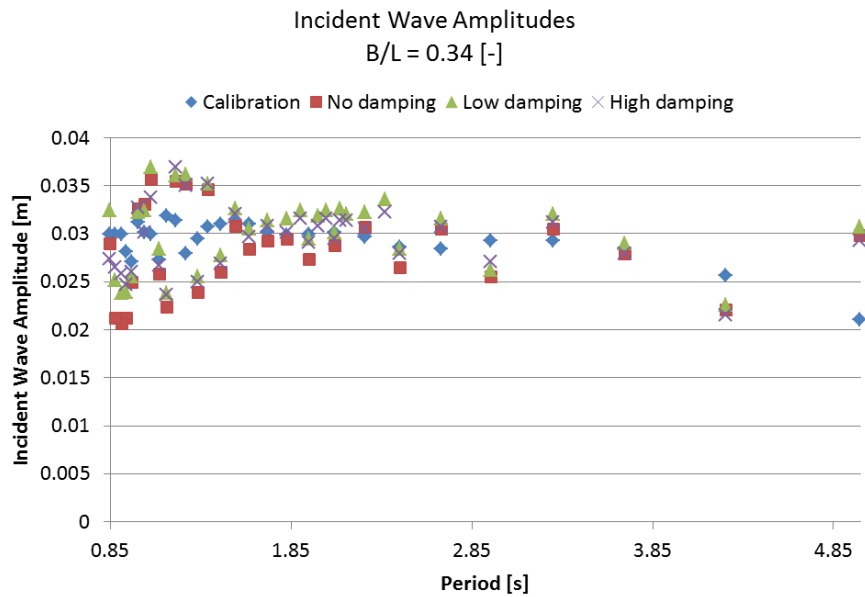


Figure 6.1: Incident wave amplitudes for the first wall position determined through the Mansard & Funke method in WaveLab 3.

refer to the width of the chamber and the length of the tube. Also, we can note that the difference between the runs including the Ocean Falls are smaller than those compared to the calibration runs. These graphs are included to evaluate the extent of consistency of the Mansard & Funke reflection analysis employed in WaveLab 3 with respect to each performed run.

6.1.3. Reflection of the Ocean Falls structure

Let us now take a closer look at the reflection coefficients with the Ocean Falls included in the flume. In contrast to a vertical wall, the Ocean Falls will reflect the incoming waves differently for varying frequencies. At resonant frequencies the structure will have a lower reflection coefficient than at low and high frequencies. This reflection coefficient analysis has been performed for all runs to compare between runs including power take-off (PTO) damping and runs without. First let us consider the case with no PTO damping. Figures 6.3 and 6.4 give the graphs of the reflection coefficients of unfiltered wave gauge data of the first three wave gauges before the structure. It is clearly visible that at the resonant period the reflection coefficient reaches its lowest, around 80%. Similarly, for the cases of low and high damping the coefficient is lowest at resonant peaks, but significantly lower than the case of no damping. This difference in coefficients between no, low and high damping is related to the wave absorption of the structure with and without damping. In the case of no damping, the drop in reflection coefficient can be acquitted to energy losses in the system, because, theoretically, if no energy is extracted from the system the reflection coefficient should be 100%. This means, for the case of incident wave amplitudes at around circa 0.03 m the Ocean Falls maximum wave absorption is around 20% for both cases. It is well known that the wave energy flux is related to the wave height squared, so it is difficult to generalise the values obtained here. The low damping cases reduce the reflection coefficient to circa 35%, meaning in the low damping case additionally circa 35%-40% of the wave amplitude is absorbed. As expected, the high damping case further reduces the reflection coefficient to around 15%, meaning additionally circa 65% of the wave amplitude is absorbed. It is interesting to study these reflection reductions for more wave amplitudes, however this does not fall within the scope of this research.

6.2. Data processing

The results from the experiments above have been obtained from unfiltered data. The performed experiments are in regular waves. Since the reality of the waves in the flume contain more than one frequency, the data needs to be filtered to include just one frequency and processed to compare adequately with respect to the theoretical model. It is true that you can input multiple frequency excitations into the model and filter less information, but for convenience it is chosen to use just one. This section contains a brief explanation of the data processing. Appendix C gives a more in depth depiction.

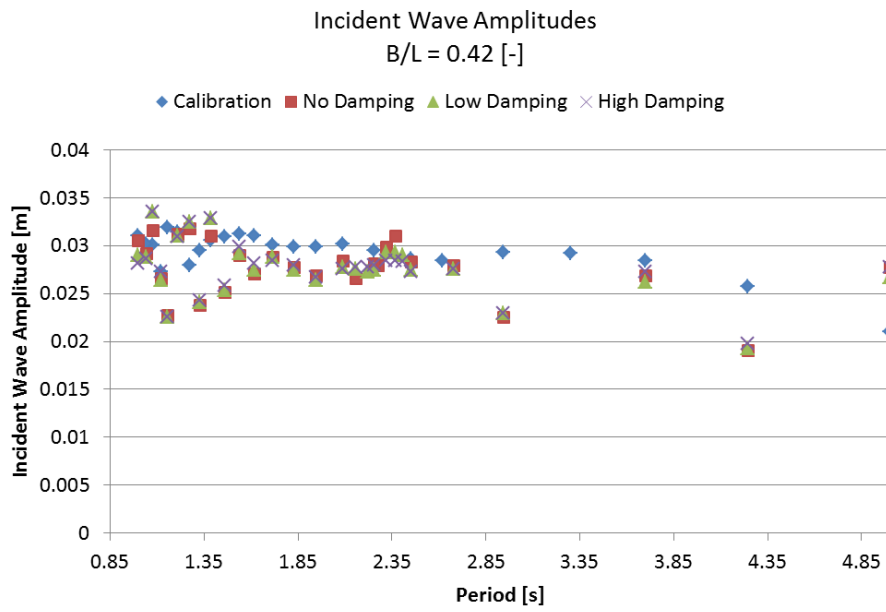


Figure 6.2: Incident wave amplitudes for the first wall position determined through the Mansard & Funke method in WaveLab 3.

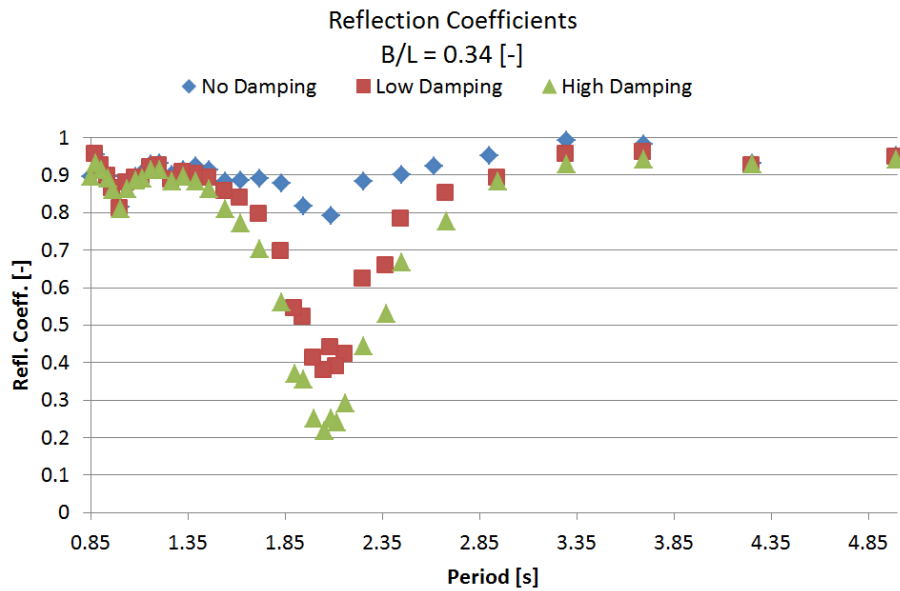


Figure 6.3: Reflection coefficients of the structure for the second wall position determined through the Mansard & Funke method in WaveLab 3.

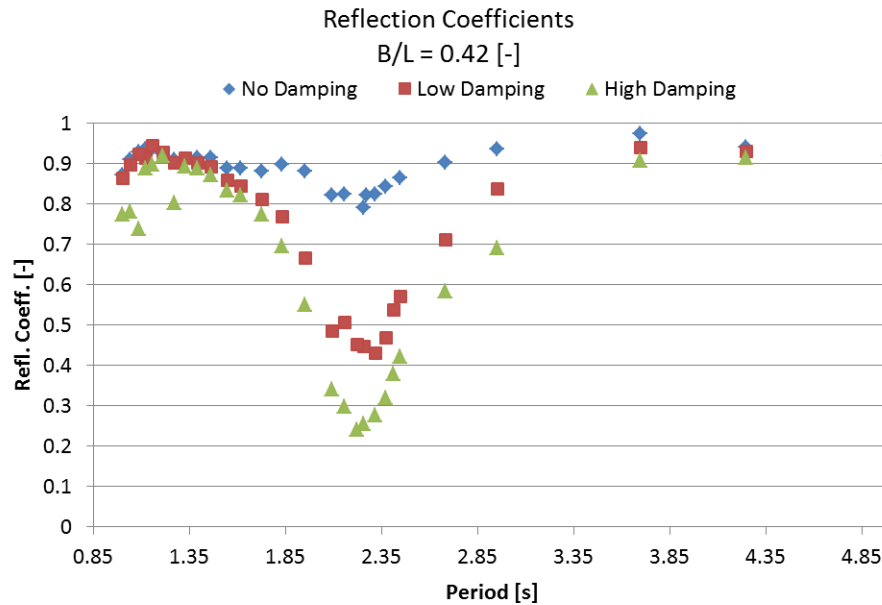


Figure 6.4: Reflection coefficients of the structure for the second wall position determined through the Mansard & Funke method in WaveLab 3.

Firstly, since the pressure data acquisition system has a slightly different sampling rate compared to the elevation one, these pressure data sets have been down-sampled to have the same sampling rate as the elevation data. Secondly, both the pressure and elevation data sets have been filtered to include only one frequency. This is done by taking the Fourier transform of the data sets and removing all frequencies except for the one containing the most power spectral density. Taking the inverse Fourier transform of the filtered frequencies gives the filtered regular wave in time-domain. To compute the flow, the elevation data is simply differentiated with respect to time and multiplied by the internal water surface area. Finally, in order to obtain the power available to the turbine in time the lag between both the pressure and elevation data sets must be fixed. During the experiments, the performer of the experiments must walk between both data acquisition systems and cannot start them simultaneously. Therefore, a lag between both data sets is present. This lag can be fixed by taking the cross correlation of both data sets, determining the lag time and shifting either data set to align with the other. The above explained method is briefly what has been employed before the experiment results and model results have been compared. Please refer to appendix C for a more extensive explanation.

6.3. Response to no turbine damping

Before considering the damping of the turbine, let us consider the case where there is no lid placed on the structure, meaning it is not damped. Figure 6.5 gives the flow amplitudes per meter incident wave amplitude inside the chamber for various periods. In these graphs the measured data is compared to the theoretical model. Firstly, we can acknowledge that the peaks of the theoretical model are higher than the measured data. This falls within the expectation since the model is linear and does not include any energy losses other than radiation damping; friction, viscous losses and other non-linear phenomenon are not accounted for. However, this does not mean that the radiation damping and added mass determined through the AQWA model is correct. One can observe that the resonant peaks are significantly different in the model and predicted case. An explanation for this can be that the model underestimates the mass of the system, which can perhaps be acquitted to the inadequate approximation of the added mass and radiation damping by the AQWA model. Please refer to appendix B for more insight in the AQWA model.

6.4. Determining equivalent linearised turbine parameter K_1

Before any comparison can be made between the theoretical model and the experiments with damping, we must determine the linear damping coefficient K_1 .

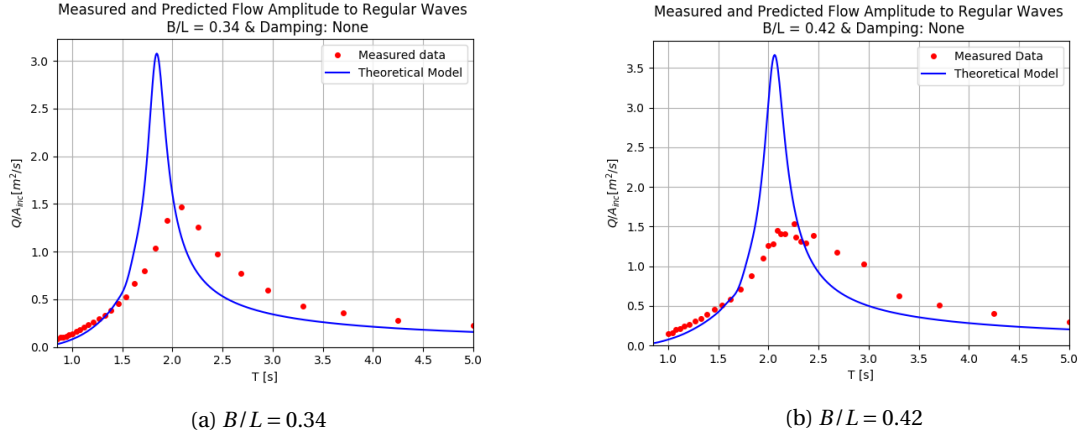


Figure 6.5: Flow amplitude per meter incident regular wave amplitude with no PTO damping.

The Wells turbine which has been used in the linear model can adequately be represented by a linear relation between pressure and flow according to Falcão et al. [15]. In model scale experiments this linear relation can be represented by a porous membrane. However, during the performed experiments, for convenience, an orifice type damping has been employed, where the internal water surface is damped by adding a lid on the air chamber with an opening. In the latter type, the pressure-flow relation is quadratic. Including this non-linearity ensures that the equations of motion cannot be solved in the frequency domain. Therefore an equivalent linearisation is necessary. The quadratic relation obtained from the experiments is linearised by equating the energy over one period for both linear and non-linear case to obtain an equivalent linearised damping coefficient from the experiments, which will be referred to as $K_{1,mes}$. Following the method of linearisation employed by Bingham et al. [51], let us denote the linear and quadratic relations of the pressure and flow as

$$p(t) = \frac{1}{a_2} q(t)^2 \text{sgn}(q(t)) \quad (6.1)$$

$$p(t) = \frac{1}{a_1} q(t) \quad (6.2)$$

Now, let us define the pressure and flow as harmonics in time as

$$q(t) = |\tilde{Q}| \sin(\omega t) \quad (6.3)$$

$$p(t) = |\tilde{P}| \sin(\omega t) \quad (6.4)$$

where \tilde{Q} and \tilde{P} are respectively the flow and pressure complex amplitudes, given in eq. 4.17 and eq. 4.18. The wave energy over one period can be given by

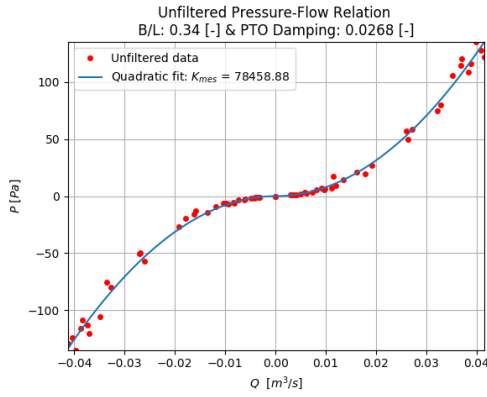
$$W = \frac{1}{T} \int_0^T p(t) q(t) dt \quad (6.5)$$

Inserting the pressure and flow defined above for both the linear and non-linear case and equating both gives us the following relation

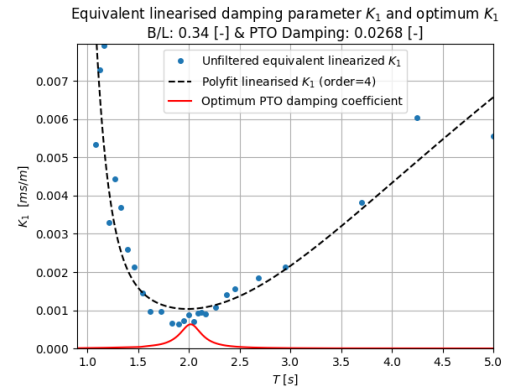
$$a_1 = \frac{3\pi}{8|\tilde{Q}|} a_2 \quad (6.6)$$

This flow is dependent on the linear damping coefficient a_1 and also the incident wave amplitude and frequency and therefore needs to be solved iteratively. Solving this equation gives a linearised damping coefficient a_1 for a certain frequency and amplitude. a_1 relates to the notation used in chapter 3 as

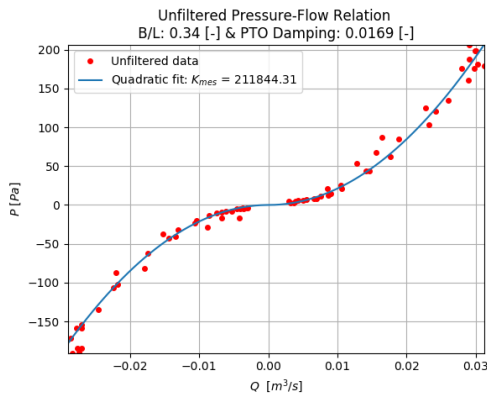
$$K_{1,mes} = a_1 \frac{\rho a}{d} \quad (6.7)$$



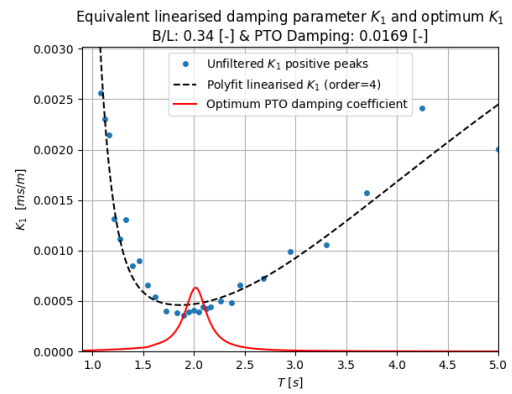
(a) Pressure flow relation.



(b) Linearised PTO damping versus the period.

Figure 6.6: Pressure flow relation and PTO damping K_1 determination for $B/L = 0.34$ and low damping.

(a) Pressure flow relation.



(b) Linearised PTO damping versus the period.

Figure 6.7: Pressure flow relation and PTO damping K_1 determination for $B/L = 0.34$ and high damping.

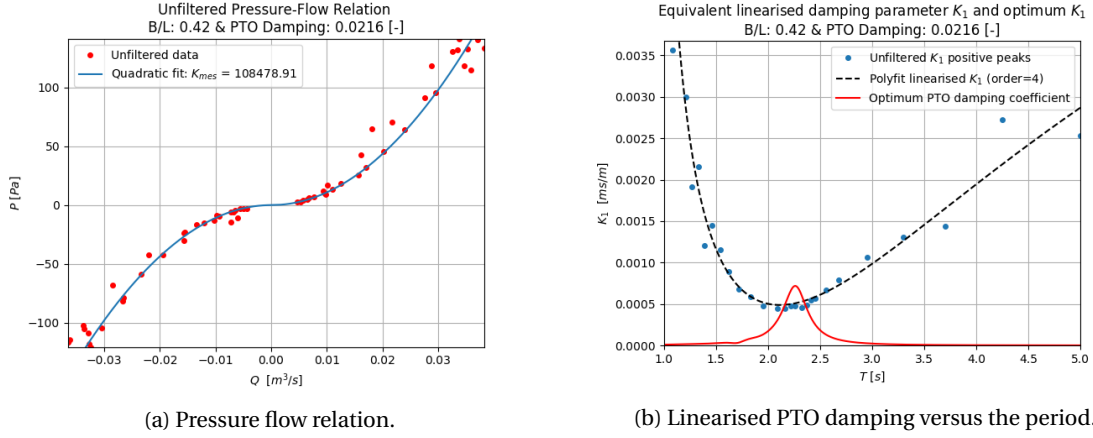
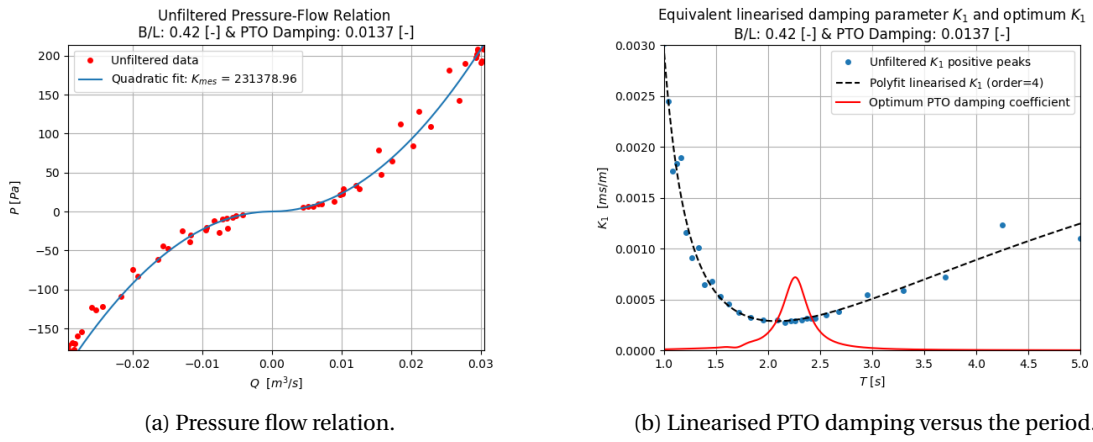
Now, with this relation the equivalent linearised PTO damping coefficients can be computed for the measured data points. Finally, a line is fit through the linearised damping coefficients to obtain an empirical expression to directly use as input for the linear solution.

Figures 6.6, 6.7, 6.8 and 6.9 give respectively the pressure-flow relation and PTO damping coefficients for both wall position scenarios and PTO damping cases. Firstly, one can state that the general trend of the pressure flow relations are indeed quadratic. The data points give good fits with the quadratic line, especially at low damping cases.

The turbine parameters are lowest (indicating high damping) at the resonant peaks, which is expected. The K_1 graphs are consistent with respect to both high and low damping and both wall positions. The optimum turbine parameter, given in equation 4.34 has also been plotted in these graphs. It is clear that at short and long periods the difference between the optimum and measured turbine parameter is the largest. The obtained PTO damping graphs are inserted into the system analytically in frequency domain to obtain the steady-state solutions. The results compared to the experiments are discussed below.

6.5. Flow and pressure

Now that the damping coefficients have been determined, the theoretical model can be computed. This has been done for the pressure, flow and power to compare these to the experimental results. Firstly, let us compare the flow computed in the theoretical model to that of the experiments. As mentioned above, the flow in the experiments has been computed through the elevation data in the chamber. The filtered flow amplitude, so containing only one frequency, has been plotted against the period. Also, the theoretical flow, computed using the determined damping coefficients is plotted. See figures 6.10, 6.11, 6.12 and 6.13 for the pressure and flow graphs. The flow approximates fairly well at high and low amplitudes, but at the resonant period,

Figure 6.8: Pressure flow relation and PTO damping K_1 determination for $B/L = 0.42$ and low damping.Figure 6.9: Pressure flow relation and PTO damping K_1 determination for $B/L = 0.42$ and high damping.

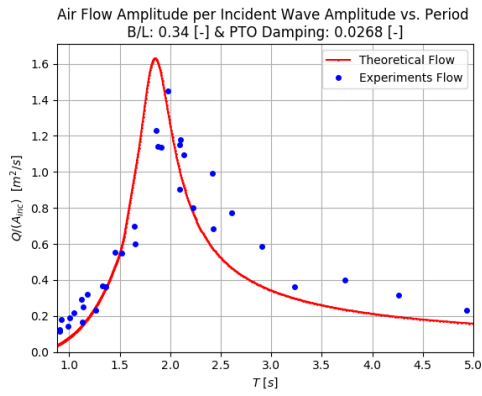
clear differences are visible. The theoretical model seems to underestimate the flow that is measured. The first reason for this is likely due to the discrepancies in the AQWA model results that have been used. This was also evident in the cases without PTO damping. Another explanation can be that the PTO damping determined is overestimated. Inaccuracies in pressure and elevation measurements can lead to wrong predictions of PTO damping. Examining pressure amplitudes one observes that the theoretical pressure amplitudes give good approximations to the measured pressure. Again there is a clear shift in resonant peak of the theoretical model with respect to the measured pressure, likely due to unreliable AQWA results. Also the measured pressure seems to be slightly lower than the theoretical model, likely due to energy losses excluding PTO damping like friction and other non-linear phenomenon.

6.6. Efficiency

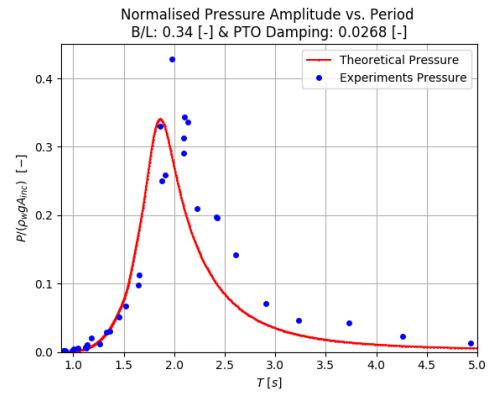
Similarly, to the theoretical model the efficiency can be computed by dividing the capture width of the experiment results by the width of the flume. The energy in the waves can be computed by using the amplitudes of the waves that have been determined through the reflection analysis discussed above and by computing the group velocities for the frequencies that remain after the filtering. The time-averaged power available to the PTO is given as

$$P_{t,mes} = \frac{1}{2} P_{mes} Q_{mes} \quad (6.8)$$

where P_{mes} and Q_{mes} are the measured pressure and flow amplitudes, respectively. This power is divided by the wave energy flux giving us the efficiency. Similarly, according to equations 4.31 and 4.32, the theoretical efficiency can be computed. Figures 6.14, 6.15, 6.16 and 6.17 give the efficiencies of the system. For the

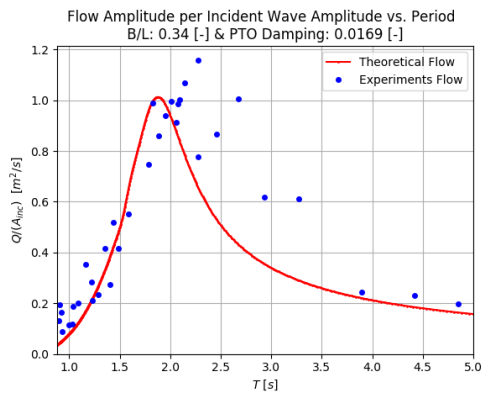


(a) Flow per incident wave amplitude.

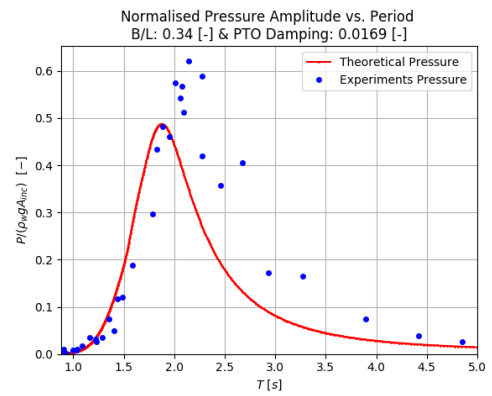


(b) Normalised pressure.

Figure 6.10: Pressure and flow for $B/L = 0.34$ and low damping.

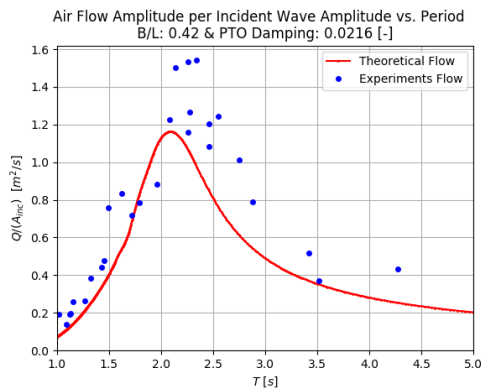


(a) Flow per incident wave amplitude.

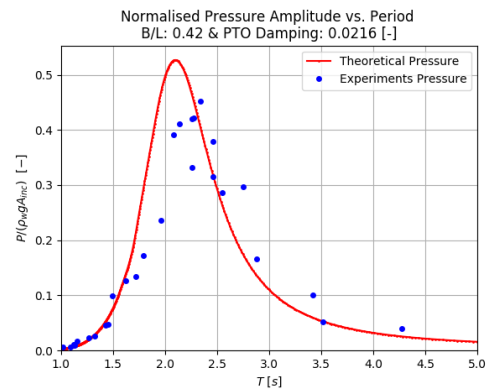


(b) Normalised pressure.

Figure 6.11: Pressure and flow for $B/L = 0.34$ and high damping.



(a) Flow per incident wave amplitude.



(b) Normalised pressure.

Figure 6.12: Pressure and flow for $B/L = 0.42$ and low damping.

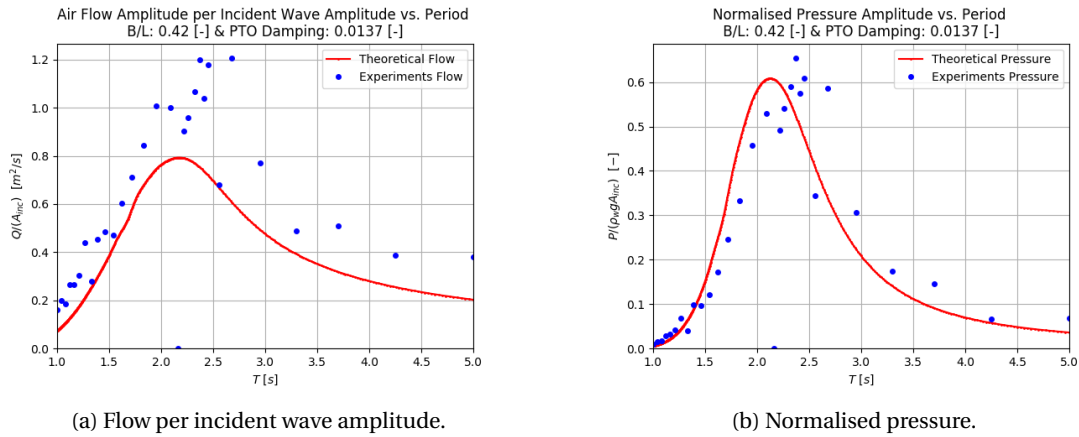


Figure 6.13: Pressure and flow for $B/L = 0.42$ and high damping.

low damping cases the theoretical efficiencies approximate the measured data fairly well, also taking into account the above discussed differences. The high damping cases, however, give slightly lower theoretical efficiencies than measured ones, indicating erroneous theory results, likely due to AQWA model discrepancies and linearisations.

A summary of all the important results of the reflection analysis and flow, pressure and efficiency analysis can be found in respectively tables 6.1 and 6.2.

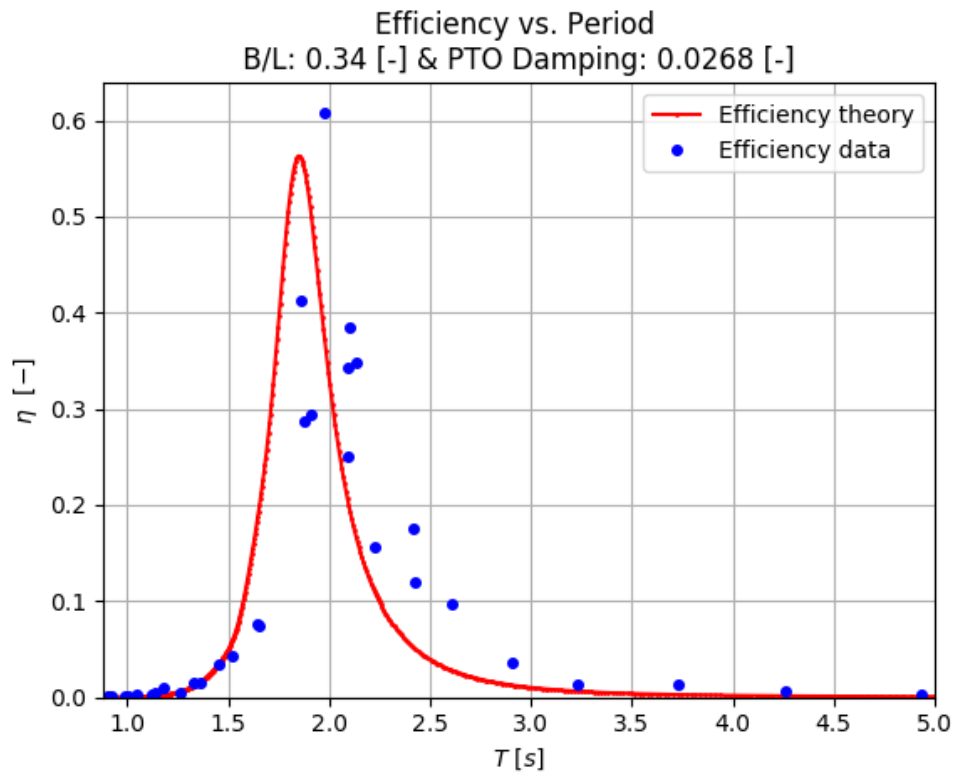


Figure 6.14: Efficiency of theoretical and experiment results for low damping and $B/L = 0.34$.

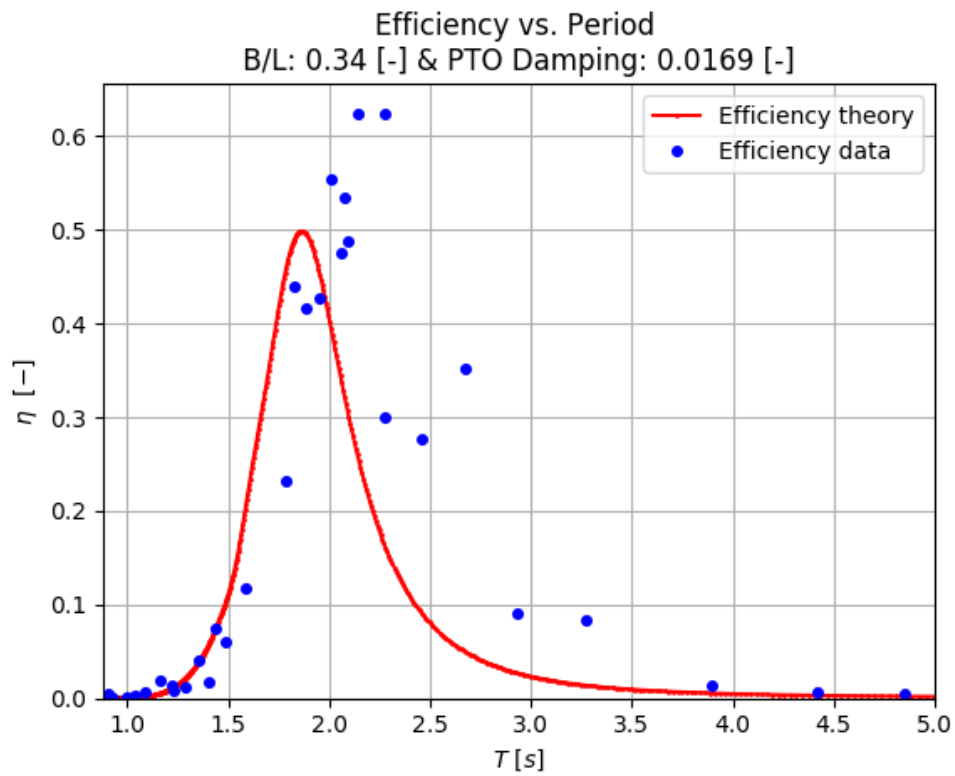


Figure 6.15: Efficiency of numerical and experiment results for high damping and $B/L = 0.34$.

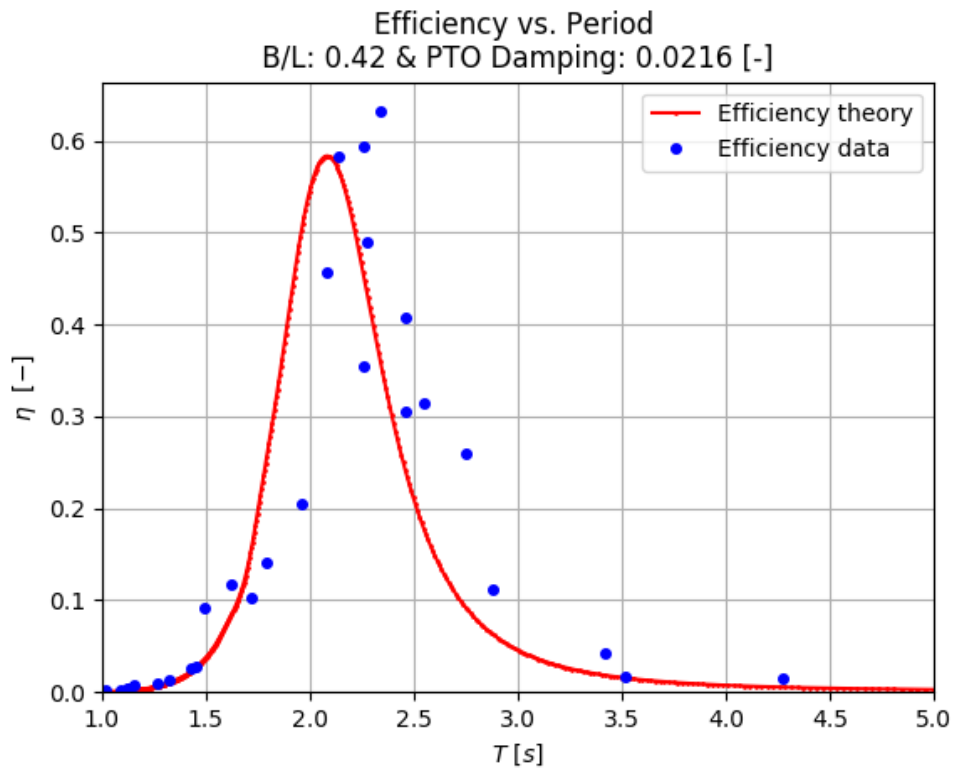


Figure 6.16: Efficiency of numerical and experiment results for low damping and $B/L = 0.42$.

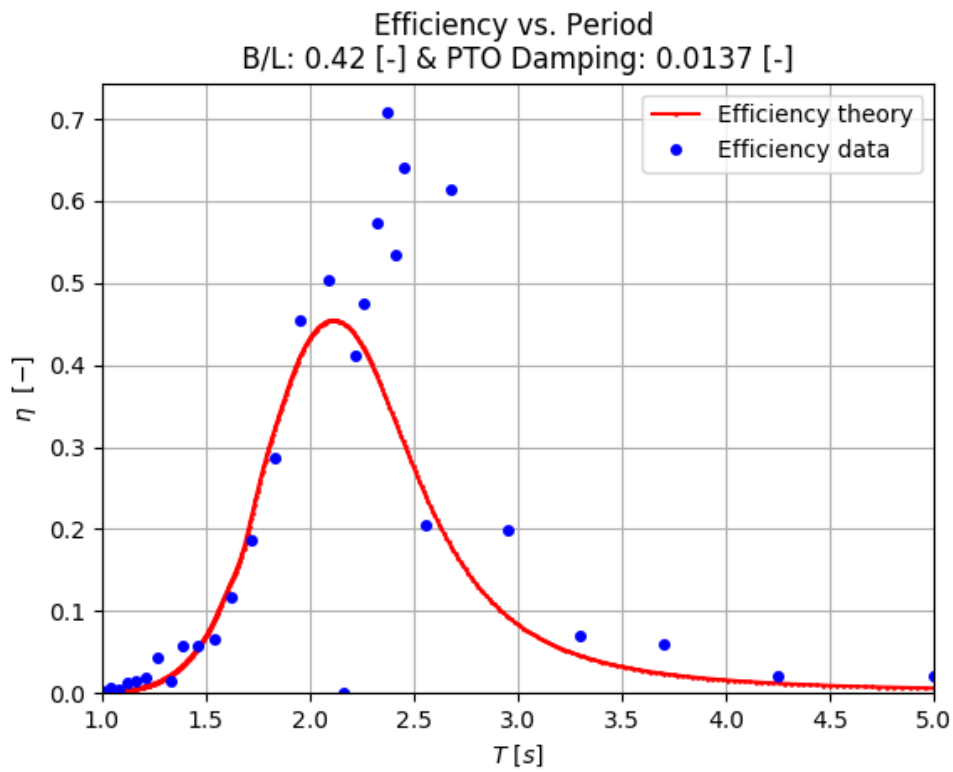


Figure 6.17: Efficiency of numerical and experiment results for high damping and $B/L = 0.42$.

Table 6.1: Table summarizing reflection analysis results. The minimum reflection coefficients are given. Values in between brackets represent the corresponding period of the given peak value.

Summary reflection analysis	Wall position 1 (B/L = 0.34)			Wall position 2 (B/L = 0.42)		
	No Damping	Low Damping	High Damping	No Damping	Low Damping	High Damping
Minimum reflection coefficient [%]	79 (T=2.09 s)	38 (T=2.05 s)	22 (T=2.05 s)	79 (T=2.26 s)	43 (T=2.32 s)	24 (T=2.22 s)

Table 6.2: Table summarizing the results for flow, pressure and efficiency in frequency domain. The peak values and peak periods are depicted in the table. The peak periods are given in between brackets. For some cases in the experiment results, the peak values have been given in terms of a range of values.

Summary of flow, pressure and efficiency results	Wall position 1 (B/L = 0.34)			Wall position 2 (B/L = 0.42)		
	No Damping	Low Damping	High Damping	No Damping	Low Damping	High Damping
Minimum turbine parameter K_1 [ms/m]	n/a	6.5 E-4	3.6 E-4	n/a	4.4 E-4	2.7 E-4
Flow $\frac{Q}{A_{inc}}$ [m^2/s]						
Model	3.1 (T=1.8 s)	1.62 (T=1.8 s)	1.0 (T=1.85 s)	4.4 (T=2.0 s)	1.2 (T=2.0 s)	0.8 (T=2.05 s)
Experiments	1.5 (T=2.05 s)	1.45 (T=1.95 s)	1.0 - 1.18 (T=2.2 s)	1.5 (T=2.25 s)	1.5 (T=2.25 s)	1.2 (T=2.5 s)
Pressure $\frac{P}{\rho_0 g A_{inc}}$ [-]						
Model	n/a	0.34 (T=1.8 s)	0.49 (T=1.85 s)	n/a	0.55 (T=2.05 s)	0.62 (T=2.05 s)
Experiments	n/a	0.35 - 0.42 (T=1.95 s)	0.6 (T=2.15 s)	n/a	0.55 (T=2.25 s)	0.63 (T=2.4 s)
Model	n/a	57 (T=1.8 s)	50 (T=1.8 s)	n/a	62 (T=2.05 s)	48 (T=2.05 s)
Experiments	n/a	42 - 61 (T=1.95 s)	50-62 (T=2.2 s)	n/a	62 (T=2.25 s)	60-70 (T=2.5 s)

6.7. Observations

6.7.1. Comparison of results

The theoretical model compared to the experiment data gives good overall agreement, except for the shift in the peak periods, where the measured peak is circa 0.25s - 0.5 s longer than in the theoretical model. The observations regarding the comparison of the model to the experiments is given below in more detail.

- Let us first consider the no damping case. As mentioned previously, the difference between model and experiments for this case can be distinguished into two parts; the difference in peak amplitude, where the model over-predicts the amplitude and the difference in peak period where the model predicts a shorter resonant period. The former can be explained due to the fact that the linear model does not account for any energy losses except for linear power take-off and radiation damping. This explains the lower peaks measured in the experiments. The latter can be acquitted to multiple reasons; the most probable is the underestimation of the added mass term in the model. Another explanation is that the damping phenomenon not included in the linear model increases the peak period.
- Furthermore, let us consider the flow, pressure and efficiency comparison between the model and the experiments. Generally, the flow is underestimated in the model for all the cases, whereas the pressure is a better match. The efficiency comparison for low damping cases give good approximations except for a shift in peak period. For high damping cases the comparison is worse, where the measured efficiencies are higher than the model prediction. This indicates two possible explanations; experimental data is erroneous and/or the linear model does not adequately represent the reality. The latter can be true since the turbine damping term is linearised, possibly explaining the peak differences at higher damping cases.

6.7.2. Experiment limitations

Experiments bear uncertainties that are related to model effects, measuring devices and data collection. These uncertainties are inevitable and need to be addressed in the interpretation of results. Several observations and limitations are given below for the performed experiments.

- For the reflection analysis, performing the experiments at high reflection runs, distortions in the standing wave occurred for long duration runs (longer than 1:30 minutes). The wave paddle seemed to have difficulty to keep up with high reflection waves coming back to the paddle from the structure. Clear ripples were visible in the water surface and the standing wave was clearly distorted. These effects were increasing as the wave run progressed. For long and short wave excitation periods this was especially visible at long duration runs (longer than 2:00 minutes). Also, variations of water level in y-direction (in the width of the flume) were visible, also distorting the experiments. The erroneous data from these runs has been discarded, by cutting out the data points when the distortions had started. An explanation for this distortion can be, as mentioned above, the difficulty of the wave paddle to adjust accordingly, but another reason can also be the relatively short distance between the structure and the wave paddle.
- The measuring equipment has its limitations, especially the pressure sensors. The sensors have an accuracy of 2.2% of the full span meaning their accuracy is not guaranteed under circa 22 Pa and above circa -22 Pa. The wave gauge accuracies are well enough and need not be discussed.
- During the experiments, at resonant wave periods and at high damping cases, the two lids of the air chamber, left and right of the orifice, have been observed to be moving. This motion of the flaps of the lid were measured to have an amplitude of 2-3 mm. Although small, this motion can cause an under estimation of the pressure inside the chamber, because pressure is relieved due to the oscillation of the flaps. Also, the damping exerted onto the internal water surface is hence reduced, meaning the experiment conditions have changed for various periods during the runs. Since the effect of this occurrence has not been quantified sufficiently, it would render the comparisons made with other runs erroneous.
- During the damping runs, it is important to seal the air lid consistently. This has been done by using silicone to shut all the corners of the lid. However, the entrances of the pressure sensors have not been sealed to not damage the sensors. Therefore small air openings can be present firstly at the entrance of

the pressure sensors on the lid and also the connections to the atmosphere through the side wall. See figure 5.10. These openings, compared to the orifice of the lid are considered small and are assumed not to have much effect on the results.

- Additionally, the results that have been depicted, excluding the reflection, calibration and PTO damping results, have been filtered. Filtering these time series data can cause loss of information, especially if there are significant peaks at higher or lower frequencies of the time series data. These occurrences of multiple frequencies in the data is likely due to more frequencies present in the excitation. This was observed at some wave periods where the piston motion inside the chamber was anti-symmetric. Another possible explanation for this is the presence of non-linear effects.

6.8. Conclusion

The most important conclusions based on the experiment results are summed below.

- The Mansard & Funke wave reflection analysis has been performed for all experiment runs. The incident wave amplitudes differ significantly between calibration and structure included runs, especially at long periods ($T = 5$ s). At shorter periods, this difference becomes smaller. For the $B/L = 0.42$ case the differences are larger compared to the $B/L = 0.34$ case. Also, the differences between incident waves between the runs with the structure included are significantly less. Overall, the incident wave amplitudes that are compared are in good agreement.
- The Ocean Falls absorbs around 20%, 62% and 84% of incident regular wave amplitudes for no damping, low damping and high damping cases for the $B/L = 0.34$ scenario, respectively. For $B/L = 0.42$ the absorbed percentages of incident wave amplitudes are 21%, 58% and 78% for no damping, low damping and high damping, respectively. The reflection for no damping cases can be acquitted to wave absorption of the system excluding PTO damping.
- For the no PTO damping case, the flow amplitude per meter incident wave height from the measurements and theoretical model has been plotted against the wave period. Increasing the width of the chamber B increases the resonant period, which is expected based on the model. The theoretical model overestimates the resonant peak compared to the experimental data, likely due to the fact that the model does not account for energy losses other than radiated waves. Also the natural period estimated by the theoretical model is lower than the measured one, probably due to AQWA model results.
- The pressure and flow measured give good quadratic relations. A quadratic line has been fitted through these graphs to determine equivalent linearised PTO damping coefficients by equating the energy available to the turbine over one wave period for both linear and quadratic PTO damping. The obtained K_1 values are used as input for the model.
- The theoretical flow is lower than the measured ones, especially at resonant periods and high damping cases. The theoretical pressure compares well to experiment results. For both pressure and flow the theoretical model estimates the resonant peak at a shorter period.
- For the $B/L = 0.34$ scenario, the theoretical efficiencies are circa 57% and 50% for respectively the low and high damping cases. Experiments results give 42% - 61% for low damping and 50%-62% for high damping. For the low damping case the measured values are well in line with expectations and the theoretical model, contrary to the high damping case where the measured efficiency is slightly higher than the theoretical one. The results are similar for the $B/L = 0.42$ scenario, where the theoretical efficiency is circa 62% and 48% for respectively low and high damping cases. The experiment results for these cases are 62% and 60%-70% for respectively the low and high damping cases. For all efficiencies the resonant peak is at a shorter period in the theoretical model compared to experiments.

7

Discussion and conclusions

This chapter contains the discussions, conclusions and recommendations of this research.

7.1. Discussion

Before we consider the conclusions of the performed theoretical and experimental analyses, let us consider the discussion around the linear model and experiments.

7.1.1. Theoretical model

Several assumptions and linearisations are made in order to solve the equations analytically for the steady-state response. The most important of these are given below.

- The width of the chamber B is assumed small with respect to incident wavelengths, so no variations in x -direction inside the chamber are present meaning, the internal water surface has an oscillatory piston motion. For large chamber widths compared to wavelength the piston approach loses its validity.
- The pressure inside the chamber is assumed to be uniform. Also, the ideal gas law approach is used, meaning the process of flow of air assumes no heat and matter transfer and is considered reversible. Some energy loss is thus neglected. Also, the spring-like air compressibility term in the equations of motion is linearised and is not related to the elevation inside the chamber. In reality, this spring coefficient will change as the air volume inside the chamber becomes smaller due to the water elevation.
- The hydrodynamic coefficients and diffraction forces have been computed through ANSYS AQWA. The results in AQWA bear some uncertainties, because of the difficulty of the numerical program to deal with resonating water surfaces. The hydrodynamic coefficients and diffraction forces give some discrepancies around the resonant periods. Appendix B gives an explanation of the AQWA model.
- The relation between pressure and flow has been assumed to be linear in the model. This relation in reality is quadratic, which is also evident from the experiment results. The results of the linear model, with the linearisation of the pressure-flow relation will therefore deviate from reality.
- Frictional and other non-linear energy losses inside the system have not been considered.

7.1.2. Experiment methodology and data processing

Experiments bear uncertainties that are related to model effects, measuring devices and data collection. These uncertainties are inevitable and need to be addressed in the interpretation of results. In the present experiments uncertainties are primarily related to points mentioned below.

- The measuring equipment brings some inaccuracies. The wave gauges perform well and have a sufficient accuracy. Contrary to this, the used pressure sensors have an accuracy of 2.2% of the full span which is equal to 22 Pa. Data retrieved that is lower than 22 Pa and higher than -22 Pa is not guaranteed to be accurate. This can bring implications in determining the damping coefficient at small flow oscillations.

- At resonant period runs, due to the air pressure on the bottom of the chamber lid, the flaps of the lid showed some motion at the orifice opening. This motion was measured to have an amplitude of 2-3 mm at the orifice. Although small, this motion likely reduces the pressure inside the chamber as it relieves the air and changes the damping conditions compared to cases where no motion was observed.
- The lid of the Ocean Falls is made air tight using silicone except for the entrances of the pressure sensors on the top of the lid and their respective connections to the atmosphere through the side wall. These small air openings are likely to effect pressure inside the chamber, but this effect is assumed to be minimal.
- It is probable that the wave paddle has difficulty to keep up with high reflection waves. High reflection runs, especially in short periods, showed significant distortion in the standing wave before the structure; many ripples were visible in the water surface and 3D effects were seen where the water level was significantly different in y-direction in the flume. This occurred at circa 1:30 minutes after the start of the wave generation. This can also influence the reflection analysis employed in Wavelab. To mitigate this problem the results have been cut out where the distortions had visually been determined.
- The data from the experiments that has been compared to the model has been filtered to include just one frequency. In some cases the excitation Fourier analysis gives multiple significant peaks at frequencies other than the input frequency. Filtering this data gives a portion of the reality.

The discussion points described above should be carefully taken into consideration before regarding the concluding remarks.

7.2. Conclusion

This section gives the conclusions drawn from the theoretical model and the performed experiments. The research questions mentioned in the Introduction are presented here again.

- *"How does the flow, pressure and power of the system computed through the theoretical model interact with regular and irregular waves and how does the Ocean Falls perform?"*

The system is linearly modelled as a single degree of freedom oscillating rigid piston. The rigid piston oscillations are effectively represented as a mass-spring-damper system where the spring and damper respectively represent the hydrostatic stiffness augmented with the spring-like air compressibility and the radiation damping with the addition of the PTO damping term. The hydrodynamic coefficients are determined through an ANSYS AQWA model.

For regular waves and a fixed turbine parameter, the maximum achieved efficiency is circa 55% occurring at a slightly lower period than the heave resonant peak. For the optimum turbine parameter K_1 , this maximum efficiency increases to 68%. In irregular JONSWAP waves the efficiency drops to 25% - 31% for various values of the peakedness factor γ in the JONSWAP spectrum.

- *"What is the natural period of the system and how does the linear power take-off (PTO) damping and linear air compressibility influence the natural period and what is the effect of the statically moveable wall on the resonant characteristics of the system?"*

The damped natural frequency is derived through the characteristic equation, but now including effective stiffness and damping definitions. These are respectively augmented with air compressibility and turbine damping terms. So, the air compressibility acts as a spring and the turbine as a damper. It is interesting to note that the air compressibility and turbine damper augmentations are dependent on wave frequency and are both dependent on the turbine parameter and air compressibility terms like height of the chamber and speed of sound in air. Increasing the width B of the chamber will also increase the natural period, which is expected.

- *"How does the linear model compare to experiments performed for regular waves?"*

For air flow through the turbine, the theoretical model overestimates the resonant peak compared to the experimental data for the case without PTO damping, likely due to the fact that the model does not account for energy losses other than radiated waves. Also the natural period estimated by the theoretical model is lower than the measured one, which can be caused by hydrodynamic coefficients that are not correctly modelled in the AQWA model.

The pressure and flow relation measured give good quadratic relations for the various test scenarios. A quadratic line has been fitted through these graphs to obtain the linearised equivalent turbine parameter values by equating the energy loss for both the quadratic and linear relation over one wave period. The obtained K_1 values are used as input for the model.

For tests with PTO damping, the theoretical flow is lower than the measured ones, especially at resonant periods and high damping cases. The theoretical pressure values compare well to experiment results. For both pressure and flow the theoretical model estimates the resonant peak at a lower period, similar to the case without PTO damping.

For the $B/L = 0.34$ scenario, the theoretical efficiencies are circa 57% and 50% for respectively low and high damping cases. Experiment results give 42% - 61% for low damping and 50%-62% for high damping. For the low damping case, the measured values are well in line with expectations and the theoretical model, contrary to the high damping case where the measured efficiency is slightly higher than the theoretical one. The results are similar for the $B/L = 0.42$ scenario where the theoretical efficiency is circa 62% and 48% for respectively low and high damping cases. The experiment results for these cases are 62% and 60%-70% for respectively the low and high damping cases. For all efficiencies the resonant peak is lower in the theoretical model compared to experiments, similar to the case without PTO damping.

7.3. Recommendations and further research proposals

This chapter gives an overview of the recommendations and proposals for further research projects.

7.3.1. Modelling

- The PTO damping significantly effects the linear model, especially at resonant periods. The quadratic relation between the flow and pressure has been linearised in this report. To obtain a more reliable outcome, one could extend the model to include non-linear PTO damping. This however would complicate the equations of motion significantly and render the system to only be solved in time-domain. Appendix E gives a brief explanation of the non-linear model.
- The presented linear model results can also be compared to a non-linear model results obtained through CFD code. This will give an insight in the viscous and turbulence effects in the system.
- ANSYS AQWA is used to approximate the added mass, radiation damping and diffraction forces. To obtain a second view on this, one should compare these results to the results obtained from other software like WAMIT and NEMOH for the same geometry.

7.3.2. Experiments

- The performed experiments were only for regular waves. Performing the same experiments for irregular waves will be useful and give a better indication of the performance of the system. This can be done primarily, by exciting the system with a summation of two or more regular waves with different frequencies. Furthermore, a white noise spectrum can be employed to have a broad frequency range.
- The turbine damping in the experiments has been modelled by an orifice, which depicts a quadratic relation between pressure and flow. The theoretical model contains linear turbine damping. The experiments therefore should be performed by employing a porous disc as the lid for the air chamber.
- To correctly map the reflection of the structure, one should test with multiple wave amplitudes. This will also give an indication on the relation between incident wave amplitude and wave absorption of the structure.
- The accuracy of the measurements is recommended to be improved by using more sensitive and accurate pressure sensors. Also, fixing the damping lid and using stiff material will ensure that the lid does not move at high pressures inside the chamber.
- The Mansard & Funke method of reflection analysis is assumed to be a good approximation but improving this is definitely recommended. Application of 4 or 5 wave gauges and selection of wave gauge sets with optimum spacing (or analysis of multiple sets) might give better results.

7.3.3. Recommended further study

This section gives a couple of interesting proposals that can be researched further.

- The model can be extended to include non-linear effects, for example friction. This addition will help quantify the importance of friction and give a more accurate result of the efficiency of the system.
- The back wall in the Ocean Falls is assumed to move only statically, so not having any dynamic effects. However it might be interesting to investigate the dynamic movement of the wall, be it active or passive. Where active movement means that the wall is moved by applying a force on it and passive movement is when the wall displaces when it is excited by wave forcing.

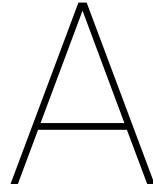
Bibliography

- [1] Gunnar Mørk, Stephen Barstow, Alina Kabuth, and M Teresa Pontes. Assessing the global wave energy potential. 20473, 2010.
- [2] Davide Magagna and Andreas Uihlein. Ocean energy development in europe: Current status and future perspectives. *International Journal of Marine Energy*, 11:84 – 104, 2015. ISSN 2214-1669. doi: <https://doi.org/10.1016/j.ijome.2015.05.001>. URL <http://www.sciencedirect.com/science/article/pii/S2214166915000181>.
- [3] Michael E McCormick. *Ocean wave energy conversion*. Courier Corporation, 2013.
- [4] António F de O. Falcão. Wave energy utilization: A review of the technologies. *Renewable and Sustainable Energy Reviews*, 14(3):899 – 918, 2010. ISSN 1364-0321. doi: <https://doi.org/10.1016/j.rser.2009.11.003>. URL <http://www.sciencedirect.com/science/article/pii/S1364032109002652>.
- [5] Sheng W., Alcorn R., and Lewis A. Assessment of primary energy conversions of oscillating water columns. i. hydrodynamic analysis. *Journal of Renewable and Sustainable Energy*, 6(5):053113, 2014. doi: 10.1063/1.4896850. URL <https://doi.org/10.1063/1.4896850>.
- [6] Wanan Sheng, Raymond Alcorn, and Anthony Lewis. Assessment of primary energy conversions of oscillating water columns. ii. power take-off and validations. *Journal of Renewable and Sustainable Energy*, 6(5):053114, 2014. doi: 10.1063/1.4896851. URL <https://doi.org/10.1063/1.4896851>.
- [7] Cuan B Boake, Trevor JT Whittaker, Matt Folley, Hamish Ellen, et al. Overview and initial operational experience of the limpet wave energy plant. In *The Twelfth International Offshore and Polar Engineering Conference*. International Society of Offshore and Polar Engineers, 2002.
- [8] Y Torre-Enciso, I Ortubia, LI López de Aguilera, and J Marqués. Mutriku wave power plant: from the thinking out to the reality. In *Proceedings of the 8th European Wave and Tidal Energy Conference, Uppsala, Sweden*, volume 710, 2009.
- [9] Y. Torre-Enciso J. Marqués, L.I. López de Aguilera. Mutriku. lessons learnt. In *Proceedings of the 3rd International Conference on Ocean Energy, Bilbao, Spain*, 2010.
- [10] Encarnacion Medina-Lopez, NWH Allsop, Aggelos Dimakopoulos, and Tom Bruce. Conjectures on the failure of the owc breakwater at mutriku. In *Proceedings of Coastal Structures and Solutions to Coastal Disasters Joint Conference, Boston, Massachusetts*, 2015.
- [11] António E.O. Falcão and João C.C. Henriques. Oscillating-water-column wave energy converters and air turbines: A review. *Renewable Energy*, 85(Supplement C):1391 – 1424, 2016. ISSN 0960-1481. doi: <https://doi.org/10.1016/j.renene.2015.07.086>. URL <http://www.sciencedirect.com/science/article/pii/S0960148115301828>.
- [12] António FO Falcão, João CC Henriques, and José J Cândido. Dynamics and optimization of the owc spar buoy wave energy converter. *Renewable energy*, 48:369–381, 2012.
- [13] R.P.F. Gomes, J.C.C. Henriques, L.M.C. Gato, and A.F.O. Falcão. Wave power extraction of a heaving floating oscillating water column in a wave channel. *Renewable Energy*, 99:1262 – 1275, 2016. ISSN 0960-1481. doi: <https://doi.org/10.1016/j.renene.2016.08.012>. URL <http://www.sciencedirect.com/science/article/pii/S0960148116307133>.
- [14] R.P.F. Gomes, J.C.C. Henriques, L.M.C. Gato, and A.F.O. Falcão. Hydrodynamic optimization of an axisymmetric floating oscillating water column for wave energy conversion. *Renewable Energy*, 44 (Supplement C):328 – 339, 2012. ISSN 0960-1481. doi: <https://doi.org/10.1016/j.renene.2012.01.105>. URL <http://www.sciencedirect.com/science/article/pii/S0960148112001413>.

- [15] António F.O. Falcão, João C.C. Henriques, Luís M.C. Gato, and Rui P.F. Gomes. Air turbine choice and optimization for floating oscillating-water-column wave energy converter. *Ocean Engineering*, 75 (Supplement C):148 – 156, 2014. ISSN 0029-8018. doi: <https://doi.org/10.1016/j.oceaneng.2013.10.019>. URL <http://www.sciencedirect.com/science/article/pii/S0029801813003892>.
- [16] Alexia Aubault, Marco Alves, António Sarmento, Dominique Roddier, and Antoine Peiffer. Modeling of an oscillating water column on the floating foundation windfloat. In *ASME 2011 30th International Conference on Ocean, Offshore and Arctic Engineering*, pages 235–246. American Society of Mechanical Engineers, 2011.
- [17] Richard Yemm, David Pizer, Chris Retzler, and Ross Henderson. Pelamis: experience from concept to connection. *Philosophical Transactions of the Royal Society of London A: Mathematical, Physical and Engineering Sciences*, 370(1959):365–380, 2012. ISSN 1364-503X. doi: 10.1098/rsta.2011.0312. URL <http://rsta.royalsocietypublishing.org/content/370/1959/365>.
- [18] Jens Peter Kofoed, Peter Frigaard, Erik Friis-Madsen, and Hans Chr. Sørensen. Prototype testing of the wave energy converter wave dragon. *Renewable Energy*, 31(2):181 – 189, 2006. ISSN 0960-1481. doi: <https://doi.org/10.1016/j.renene.2005.09.005>. URL <http://www.sciencedirect.com/science/article/pii/S0960148105002582>. Marine Energy.
- [19] James Tedd and Jens Peter Kofoed. Measurements of overtopping flow time series on the wave dragon, wave energy converter. *Renewable Energy*, 34(3):711 – 717, 2009. ISSN 0960-1481. doi: <https://doi.org/10.1016/j.renene.2008.04.036>. URL <http://www.sciencedirect.com/science/article/pii/S096014810800195X>.
- [20] M.E. McCormick. Modified linear analysis of a wave-energy conversion buoy. *Ocean Eng. (United States)*, 3:3, May 1976. doi: 10.1016/0029-8018(76)90029-9.
- [21] D. V. Evans. The oscillating water column wave-energy device. *IMA Journal of Applied Mathematics*, 22 (4):423–433, 1978. doi: 10.1093/imamat/22.4.423. URL <http://dx.doi.org/10.1093/imamat/22.4.423>.
- [22] A. J. N. A. Sarmento and A. F. de O. Falcão. Wave generation by an oscillating surface-pressure and its application in wave-energy extraction. *Journal of Fluid Mechanics*, 150:467–485, 1985. doi: 10.1017/S0022112085000234.
- [23] Falnes J. *Ocean Waves and Oscillating Systems: Linear Interactions Including Wave-Energy Extraction*. Cambridge University Press, 2002. doi: 10.1017/CBO9780511754630.
- [24] D. V. Evans and R. Porter. Hydrodynamic characteristics of an oscillating water column device. *Applied Ocean Research*, 17(3):155–164, 1995.
- [25] J. Falnes and P. McIver. Surface wave interactions with systems of oscillating bodies and pressure distributions. *Applied Ocean Research*, 7(4):225 – 234, 1985. ISSN 0141-1187. doi: [https://doi.org/10.1016/0141-1187\(85\)90029-X](https://doi.org/10.1016/0141-1187(85)90029-X). URL <http://www.sciencedirect.com/science/article/pii/014111878590029X>.
- [26] A. Brendmo, J. Falnes, and P.M. Lillebekken. Lineær modelling of oscillating water columns including viscous loss. *Applied Ocean Research*, 18(2):65 – 75, 1996. ISSN 0141-1187. doi: [https://doi.org/10.1016/0141-1187\(96\)00011-9](https://doi.org/10.1016/0141-1187(96)00011-9). URL <http://www.sciencedirect.com/science/article/pii/0141118796000119>.
- [27] WE Cummins. The impulse response function and ship motions. Technical report, David Taylor Model Basin Washington DC, 1962.
- [28] A. Iturrioz, R. Guanche, J.A. Armesto, M.A. Alves, C. Vidal, and I.J. Losada. Time-domain modeling of a fixed detached oscillating water column towards a floating multi-chamber device. *Ocean Engineering*, 76:65 – 74, 2014. ISSN 0029-8018. doi: <https://doi.org/10.1016/j.oceaneng.2013.11.023>. URL <http://www.sciencedirect.com/science/article/pii/S0029801813004253>.

- [29] R. Gervelas, F. Trarieux, and M. Patel. A time-domain simulator for an oscillating water column in irregular waves at model scale. *Ocean Engineering*, 38(8):1007 – 1013, 2011. ISSN 0029-8018. doi: <https://doi.org/10.1016/j.oceaneng.2011.04.006>. URL <http://www.sciencedirect.com/science/article/pii/S002980181100076X>.
- [30] I. Amin. Numerical study of an oscillating water column chamber with internal wall. *Maritime Technology and Engineering*, 2015.
- [31] Ahmed Elhanafi, Alan Fleming, Gregor Macfarlane, and Zhi Leong. Numerical hydrodynamic analysis of an offshore stationary–floating oscillating water column–wave energy converter using cfd. *International Journal of Naval Architecture and Ocean Engineering*, 9(1):77 – 99, 2017. ISSN 2092-6782. doi: <https://doi.org/10.1016/j.ijnaoe.2016.08.002>. URL <http://www.sciencedirect.com/science/article/pii/S2092678216304290>.
- [32] António E.O. Falcão and João C.C. Henriques. Model-prototype similarity of oscillating-water-column wave energy converters. *International Journal of Marine Energy*, 6:18 – 34, 2014. ISSN 2214-1669. doi: <https://doi.org/10.1016/j.ijome.2014.05.002>. URL <http://www.sciencedirect.com/science/article/pii/S2214166914000058>.
- [33] Weoncheol Koo and Moo-Hyun Kim. Nonlinear time-domain simulation of a land-based oscillating water column. *Journal of Waterway, Port, Coastal, and Ocean Engineering*, 136(5):276–285, 2010. doi: 10.1061/(ASCE)WW.1943-5460.0000051. URL <https://ascelibrary.org/doi/abs/10.1061/%28ASCE%29WW.1943-5460.0000051>.
- [34] Chia-Ying Chang, Frederick N.-F. Chou, Yang-Yih Chen, Yi-Chern Hsieh, and Chia-Tzu Chang. Analytical and experimental investigation of hydrodynamic performance and chamber optimization of oscillating water column system. *Energy*, 113:597 – 614, 2016. ISSN 0360-5442. doi: <https://doi.org/10.1016/j.energy.2016.06.117>. URL <http://www.sciencedirect.com/science/article/pii/S036054421630891X>.
- [35] Sheng W., Thiebaut E., Babuchon M., Brooks J., Lewis A., and Alcorn R. Investigation to air compressibility of oscillating water column wave energy converters. *International Conference on Offshore Mechanics and Arctic Engineering*, 8, 2013. doi: 10.1115/OMAE2013-10151. URL <http://dx.doi.org/10.1115/OMAE2013-10151>.
- [36] LMC Gato and AF de O Falcão. On the theory of the wells turbine. *Journal of engineering for gas turbines and power*, 106(3):628–633, 1984.
- [37] S.L. Dixon. *Fluid Mechanics, Thermodynamics of Turbomachinery, 4th Edition*. Butterworth-Heinemann, 1998.
- [38] A.F. de O. Falcão and P.A.P. Justino. Owc wave energy devices with air flow control. *Ocean Engineering*, 26(12):1275 – 1295, 1999. ISSN 0029-8018. doi: [https://doi.org/10.1016/S0029-8018\(98\)00075-4](https://doi.org/10.1016/S0029-8018(98)00075-4). URL <http://www.sciencedirect.com/science/article/pii/S0029801898000754>.
- [39] Riaan van’t Veer and Haye Jan Tholen. Added resistance of moonpools in calm water. In *Proceedings of the ASME 27th International Conference on Offshore Mechanics and Arctic Engineering. OMAE2008-57246*, 2008.
- [40] W Sheng, R Alcorn, and A Lewis. Hydrodynamics of owc wave energy converters. *Proc. 1st Renew. Energies Offshore*, pages 24–26, 2014.
- [41] AF de O Falcão and RJA Rodrigues. Stochastic modelling of owc wave power plant performance. *Applied Ocean Research*, 24(2):59–71, 2002.
- [42] Leo H Holthuijsen. *Waves in oceanic and coastal waters*. Cambridge university press, 2010.
- [43] Klaus Hasselmann. Measurements of wind wave growth and swell decay during the joint north sea wave project (jonswap). *Dtsch. Hydrogr. Z.*, 8:95, 1973.
- [44] J.M.J. Journée, W.W. Massie, and R.H.M. Huijsmans. *Offshore Hydromechanics*. TU Delft Press, 2000.

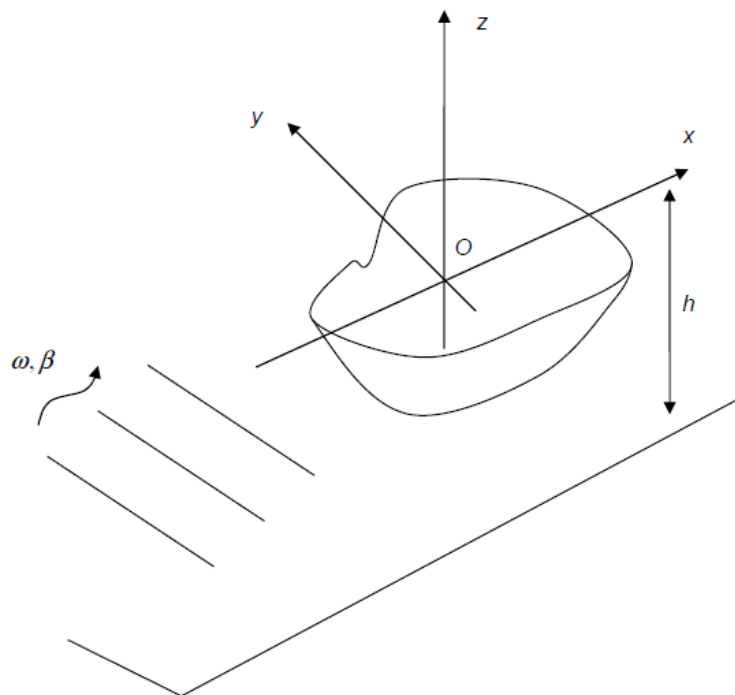
- [45] K Rezanejad, C Guedes Soares, I López, and R Carballo. Experimental and numerical investigation of the hydrodynamic performance of an oscillating water column wave energy converter. *Renewable energy*, 106:1–16, 2017.
- [46] E.P.D. Mansard and E.R. Funke. *The Measurement of Incident and Reflected Spectra Using a Least Squares Method*. 1980. doi: 10.1061/9780872622647.008. URL <https://ascelibrary.org/doi/abs/10.1061/9780872622647.008>.
- [47] J-M. Forestier, B. Holmes, S. Barrett, and A.W. Lewis. Value and validation of small scale physical model tests of floating wave energy converters. 2007. URL <https://eprints.soton.ac.uk/167115/>.
- [48] Edinburgh Designs. Edinburgh designs piston coastal wave generators. <http://www4.edesign.co.uk/>. Accessed: 25-01-2018.
- [49] Thomas Lykke Andersen Peter Frigaard. *Analysis of Waves Technical Documentation for WaveLab 3*. Aalborg University Department of Civil Engineering, 2014.
- [50] Yoshimi Goda and Tasumasa Suzuki. Estimation of incident and reflected waves in random wave experiments. *Coastal Engineering Proceedings*, 1(15), 2011. ISSN 2156-1028. doi: 10.9753/icce.v15.%p. URL <https://icce-ojs-tamu.tdl.org/icce/index.php/icce/article/view/3096>.
- [51] Harry B Bingham, Damien Ducasse, Kim Nielsen, and Robert Read. Hydrodynamic analysis of oscillating water column wave energy devices. *Journal of Ocean Engineering and Marine Energy*, 1(4):405–419, 2015.
- [52] Énergétique et Environnement Atmosphérique Laboratoire de recherche en Hydrodynamique. *General notations and conventions*. LHEEA Centrale Nantes.
- [53] ANSYS Inc. *ANSYS AQWA Theory Manual*. 2017.
- [54] E. Mackay. Modelling owcs in nemoh. <http://130.66.47.2/redmine/boards/3/topics/501>.
- [55] Markel Penalba, Thomas Kelly, and John V Ringwood. Using nemoh for modelling wave energy converters: A comparative study with wamit. *Centre for Ocean Energy Research (COER), Maynooth University, Co. Kildare, Ireland*, 2017.
- [56] T Francis Ogilvie. Recent progress toward the understanding and prediction of ships motion. In *Proceedings of the 5th Symposium on Naval Hydrodynamics*, pages 3–128, 1964.
- [57] Tristan Perez and Thor I Fossen. A matlab toolbox for parametric identification of radiation-force models of ships and offshore structures. *Modeling, Identification and Control*, 30(1):1, 2009.
- [58] Reza Taghipour, Tristan Perez, and Torgeir Moan. Hybrid frequency–time domain models for dynamic response analysis of marine structures. *Ocean Engineering*, 35(7):685–705, 2008.
- [59] R. Guanche J.A. Armesto. Translation of fdi toolbox into python.



Solutions to potential flow theory

The following has been taken from NEMOH general notations and conventions documentation [52], which can be found [here](#).

General notations and conventions



Units:

All units are SI units :

- Length is in meter
- Mass is in kg
- Time is in second
- Frequency (circular) is in rad/s
- Phase angle are in radian

Reference frame:

$O(0,0,0)$ is the origin of the reference frame. The horizontal plane $z=0$ defines the free surface at rest. The vertical axis z is pointing upwards. 0 degrees wave direction means that the wave is propagating towards the x positive axis.

Notations:

- h is the water depth
- ω is the wave frequency
- k is the wave number
- β is the direction of incident wave propagation
- t is time
- (x, y, z) are coordinates in the Cartesian reference frame. (r, θ, z) are coordinates in the cylindrical reference frame.
- p denotes the pressure
- ϕ is a velocity potential
- \vec{V} is a velocity
- g is gravity
- A is the incident wave amplitude

Mathematical expressions for physical quantities:

- Phase of the incident wave elevation is 0 at origin. Incident wave elevation is given by:

$$\eta_I(x, t) = A \cos(k(x \cos \beta + y \sin \beta) - \omega t) = \Re\left(A e^{i(k(x \cos \beta + y \sin \beta) - \omega t)}\right)$$

with k solution of the dispersion relation $kg = \omega^2 \tan kh$.

- The excitation force relates to the incident wave according to:

$$F_{ex}(t) = \Re\left(A \tilde{F}_{ex}(\omega) e^{-i\omega t}\right) = \Re\left(A \left| \tilde{F}_{ex}(\omega) \right| e^{-i(\omega t - \angle \tilde{F}_{ex}(\omega))}\right)^1$$

- The incident wave potential is:

$$\phi_I(x, t) = \Re\left(-\frac{ig}{\omega} A f_0(z) e^{i(k(x \cos \beta + y \sin \beta) - \omega t)}\right)$$

with $f_0(z) = e^{kz}$ in deep water and $f_0(z) = \frac{\cosh(k((z+h)))}{\cosh(kh)}$ in intermediate water depth.

- The incident wave pressure field is:

$$p_I(x, t) = \Re\left(\rho g A f_0(z) e^{i(k(x \cos \beta + y \sin \beta) - \omega t)}\right)$$

- The incident wave velocity field is:

$$\circ \vec{V}(M, t) = \Re\left(\frac{g}{\omega} A \begin{pmatrix} k \cos \beta \\ k \sin \beta \\ -ik \end{pmatrix} e^{kz} e^{i(k(x \cos \beta + y \sin \beta) - \omega t)}\right) \text{ in deep water.}$$

$$\circ \vec{V}(M, t) = \Re\left(\frac{g}{\omega} A \begin{pmatrix} k \cos \beta \cosh(k((z+h))) \\ k \sin \beta \cosh(k((z+h))) \\ -ik \sinh(k((z+h))) \end{pmatrix} \frac{1}{\cosh(kh)} e^{i(k(x \cos \beta + y \sin \beta) - \omega t)}\right) \text{ in}$$

intermediate water depth.

¹ This equation shows that the phase angle of the excitation force in Nemoh is opposite to the one in Aquaplus.

B

Ocean Falls ANSYS AQWA model

The modelling of oscillating water columns in ANSYS AQWA is trickier than conventional oscillating bodies such as ships or buoys. In essence the oscillating body in the Ocean Falls case is the water mass inside the channel. It is difficult for BEM software to characterise the motion of a body that does not exist. This chapter contains the thought and modelling process to obtain the most accurate AQWA model for the Ocean Falls.

B.1. ANSYS AQWA

Firstly it is important to address the method of solution behind ANSYS AQWA to avoid it being perceived as a 'black box'. This section contains a brief summary of the numerical solution method behind AQWA.

In the case of relatively small amplitude waves, the incident wave forcing is defined by the the linear (first order) Froude-Krylov force corrected by a diffraction force which is induced by the disturbance wave because of the existence of an oscillating body. Firstly, AQWA solves the diffraction and Froude-Krylov forcing for complex geometry systems. In some other cases, like larger or sever seas, the second order waves and transient forces may also be interesting to considered. Although AQWA solves these, they will not be included in this report because they do not fall within the scope of this work. Secondly, the radiation forces due to the disturbance waves caused by the oscillation of a considered body are also computed by AQWA.

This problem for complex geometries is generally solved using three dimensional panel methods based on the fluid potential theory, representing the surface of the structure or structures by a series of wave diffracting panels. Fluid potential theory is the description of the mechanics of fluids that satisfy the basic laws of fluid mechanics, namely the conservation of mass and momentum. This theory assumes that the fluid is incompressible, inviscid and irrotational, similar to the linear wave theory. A fine explanation of the fluid potential theory can be found in the Offshore Hydromechanics lecture notes by Journée et al. [44]. AQWA also can compute the Morison drag forces on slender bodies, but this is not relevant to this research and is therefore omitted.

As the surface of the structure is split into multiple panels, the differential equations and boundary conditions governing the fluid motion around the structure can be solved. This solution method is referred to as a boundary integration approach, where the fluid velocity potential is solved by input conditions. This integration occurs with the use of the Greene's function, which simply put, states that each panel contains a source term that with the use of the hull wetted surface boundary condition can be solved. Solving these source terms will yield the solution to the diffraction and radiation problem. The AQWA Theory manual chapter 4 [53] gives a more comprehensive and elaborate explanation of this method and clearly states the equations that are solved in the AQWA code. The differential equation and boundary conditions that are solved are also given there. Some key assumptions, as they have been noted in the AQWA Theory Manual [53], are:

- The oscillating body is assumed to have none or very small forward speed. This is the case with the oscillating water column, so this assumption will have no effect on the results with respect to reality.
- The water is inviscid, incompressible and water flow irrotational. These assumptions have also been stated in the derivation process in chapter 3.

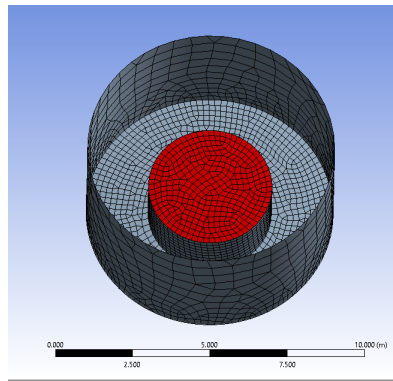


Figure B.1: AQWA model mesh for a piston length of 3m.

- All body motions are harmonic and the incident waves have a small amplitude with respect to wavelength, meaning their slope is small. This is also the case for the Linear Wave Theory and hence incorporated in the derivation in the linear model.

B.1.1. WAMIT/NEMOH comparison

Before jumping into directly modelling the Ocean Falls in AQWA, perhaps it is wiser to place oscillating water columns in general into context within AQWA and other software. This section contains a comparison made between on the one hand ANSYS AQWA and on the other hand WAMIT/NEMOH results regarding a simple oscillating water column. The OWC has a cylinder structure with outer and inner diameters of 8m and 4m, respectively. The structure has a draft of 5m. The lengths of the pistons are varied from 1 m to 5 m. See figure B.1 below.

A comparison of results between the WAMIT model and the NEMOH model has been done for this geometry, with varying mesh resolutions, by Mackay [54]. Another interesting comparison for a similar oscillating water column has been made by Penalba et al. [55]. Combining these two sources together gives a more accurate approach to modelling OWCs in BEM software such as AQWA. The piston length has been varied from 1m to 5m. The model consists of 2 diffracting sections, the first is the outer, bottom and inner faces with normals facing the water. This section of the system is fixed in place. The second part of the system is the 'rigid piston' modelled as a surface (representing the bottom of the piston) with normals facing downwards. This surface is free to move. The results for the added mass, radiation damping and excitation force are given in figures B.2 and B.3.

It is clear that NEMOH shows some discrepancies regarding added mass, radiation damping and force excitation. For smaller piston lengths, the added mass and radiation damping show lower results than for the same mesh in WAMIT. For higher resolution meshes this difference is lower but still visible. Based on these results one could say that a large length and finer mesh resolution chosen for the piston is more favourable when modelling OWCs using NEMOH.

B.1.2. ANSYS AQWA model

The OWC for AQWA is modelled in a similar manner. The first body is the fixed 'outer' body of the system, consisting of the outer tube, the bottom and the inner tube. The diffracting panel normals are facing towards the water for each of these surfaces. The second body is the piston surface, which is at the top of the inner tube. This surface models the bottom surface of the rigid piston. The piston is constrained in all degrees of freedom except for heave. Figures B.4, B.5 and B.6 give the hydrodynamic results obtained from AQWA for the same model but a slightly different mesh (see figure B.1). The total mass of the system based on available literature is given by the sum of the total length of the water column and an 'end-correction' length equal to $l = 0.6133r$ according to Evans [21].

It is clear that the AQWA model follows the NEMOH results based on the change results. However it is also clear that NEMOH and AQWA results converge towards the WAMIT results for increased mesh resolution. In conclusion the piston should be placed at the lower part of the water column, so large piston lengths are favourable for a more accurate result. Also a finer mesh resolution is needed to obtain more accurate results.

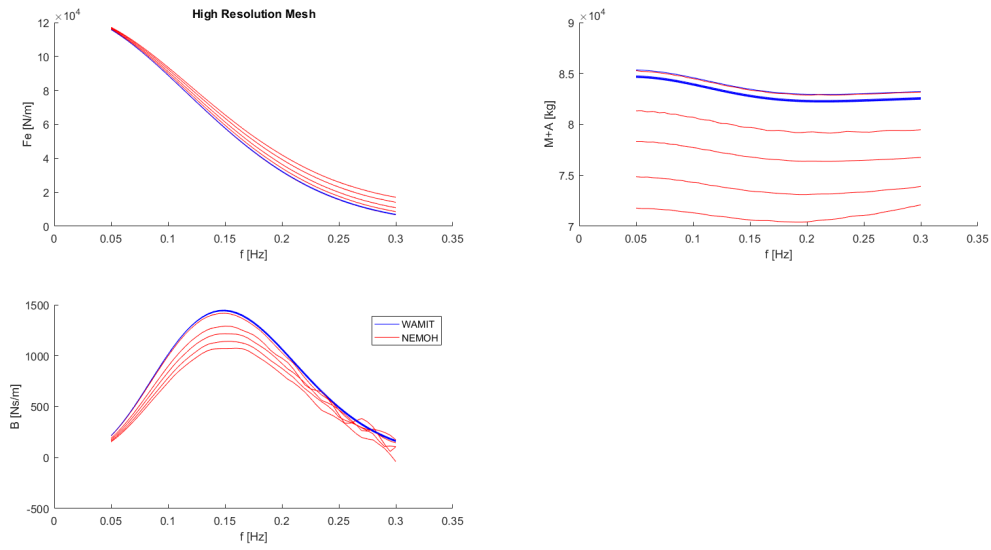


Figure B.2: Comparison in WAMIT and NEMOH results for simple geometry OWC for high resolution meshes [54].

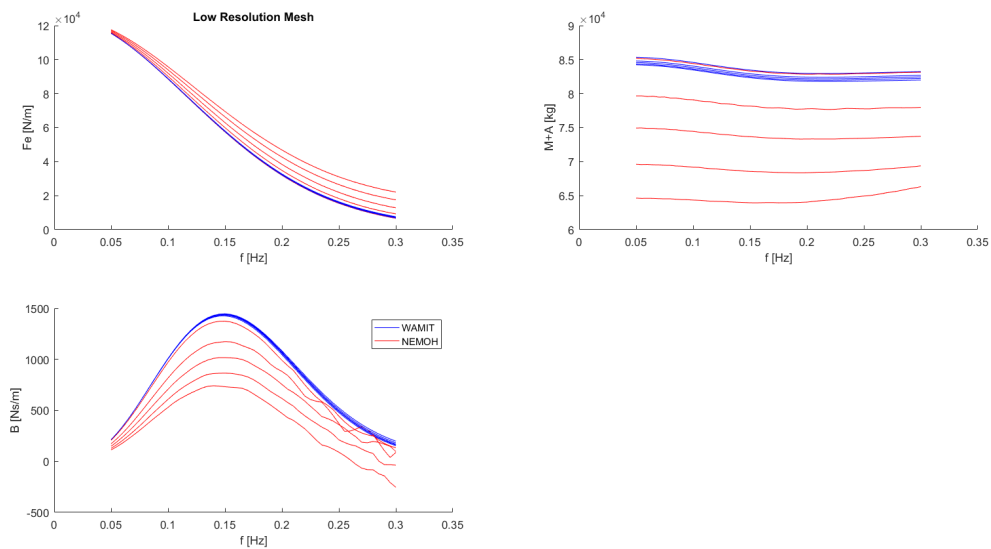


Figure B.3: Comparison in WAMIT and NEMOH results for simple geometry OWC for low resolution meshes [54].

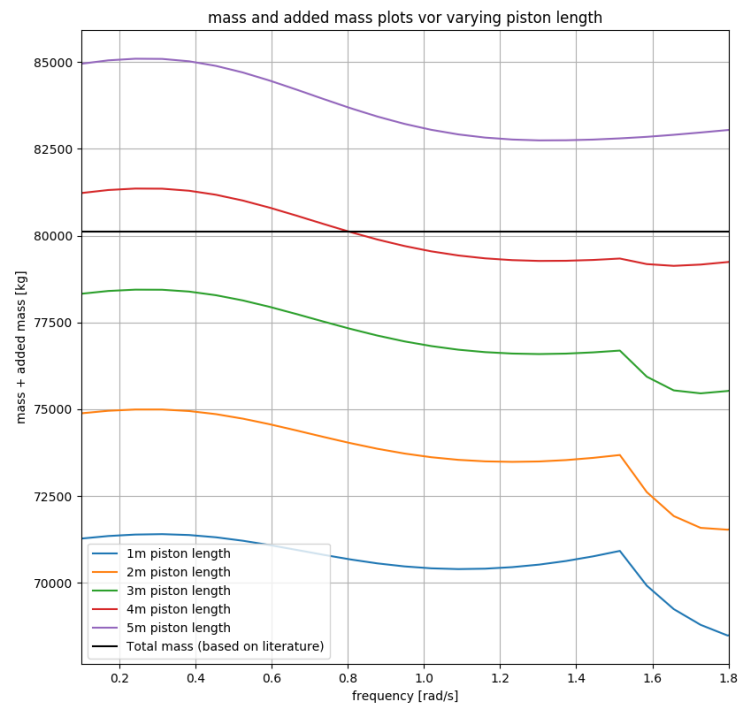


Figure B.4: Mass and added mass obtained from the AQWA model.

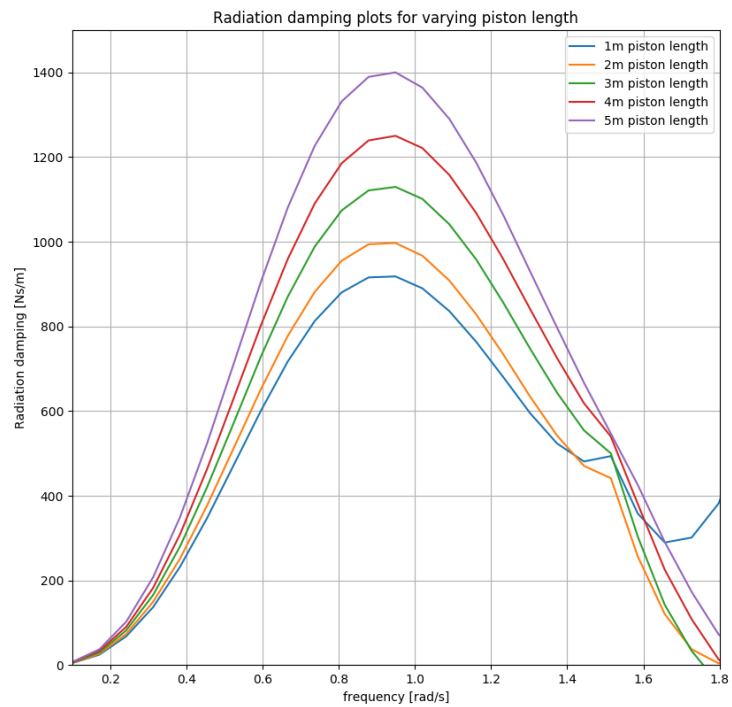


Figure B.5: Radiation damping obtained from the AQWA model.

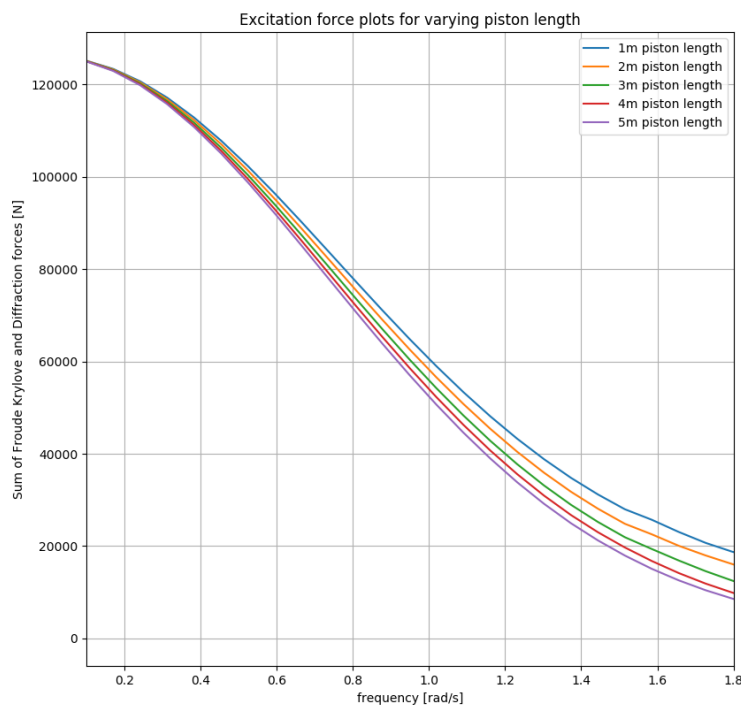


Figure B.6: Excitation obtained from the AQWA model.

B.2. The Ocean Falls AQWA model

This section contains the Ocean Falls final model that has been used in the numerical computations in this research.

B.2.1. Geometry definition

The geometry of the Ocean Falls as has been used in the experiment set-up is designed into ANSYS AQWA through the SpaceClaim designer. The only addition to this is the piston-like plate that has been added at the opening of the tube. The Ocean Falls itself is fixed while this piston is set to oscillate freely only in x-direction. This approach automatically removes the effect of the inclination of the tube. This angle had been assumed to be small, but it is important to note that the model does not account for this. This will cause the results in AQWA to differ from those in reality, but this difference has been assumed to be small. So these two bodies will interact with each other for incoming waves. It is important to note that the key difference between the simple geometry OWC stated in the previous section and the model for the Ocean Falls presented here, is the change in orientation and thus the effective stiffness of the piston. This difference has also been underlined in derivations in chapter 3. The Ocean Falls geometry is given figure B.7. The dimensions in this figure have been directly used in the AQWA model.

Additionally, an internal lid has been generated in the AQWA runs that ensures that the occurrence of irregular frequencies is negated as much as possible. Irregular frequencies are errors that cause abrupt variations in the results in surface piercing hulls. The irregular frequencies are a solely numerical problem and have no physical meaning. Also, in the case of the Ocean Falls, real resonance phenomenon occurring in the chamber will have similar abrupt variations in the hydrodynamic coefficients. Employing an internal lid will force the vertical component of the interior fluid velocity inside the structure hull (so where in reality there is no water) to be zero. This will to some extent diminish the above stated problems.

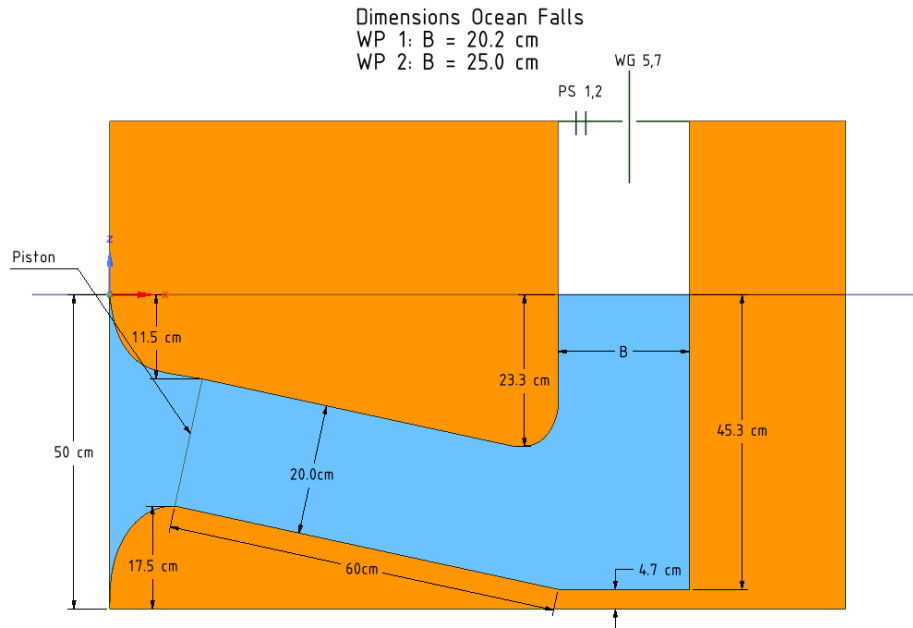


Figure B.7: The geometry of the Ocean Falls flume model. These values have been directly used in AQWA. The piston is also indicated in the figure.

B.2.2. Mesh configuration

Once the geometry of the system has been designed in a design module, SpaceClaim in this case, the geometry can be meshed. Meshing is nothing else than representing a geometry as a set of finite elements, panels in our case. As mentioned above, a higher mesh resolution i.e. more panels, yields a better result. Therefore a very large amount of panels has been employed in both wall positions. The built in AQWA mesh generator is used. See figures B.8.

B.2.3. Input wave conditions

The input wave periods used for the flume Ocean Falls model range from $T = 5$ s to $T = 0.85$ s, staying within the range of the flume wave generator. The water density in the flume is set to sweet water at $\rho_w = 1000 \text{ kg/m}^3$. There is only one direction possible inside the flume so no variations in direction have been employed in AQWA. The water level has been set to $h = 0.5 \text{ m}$.

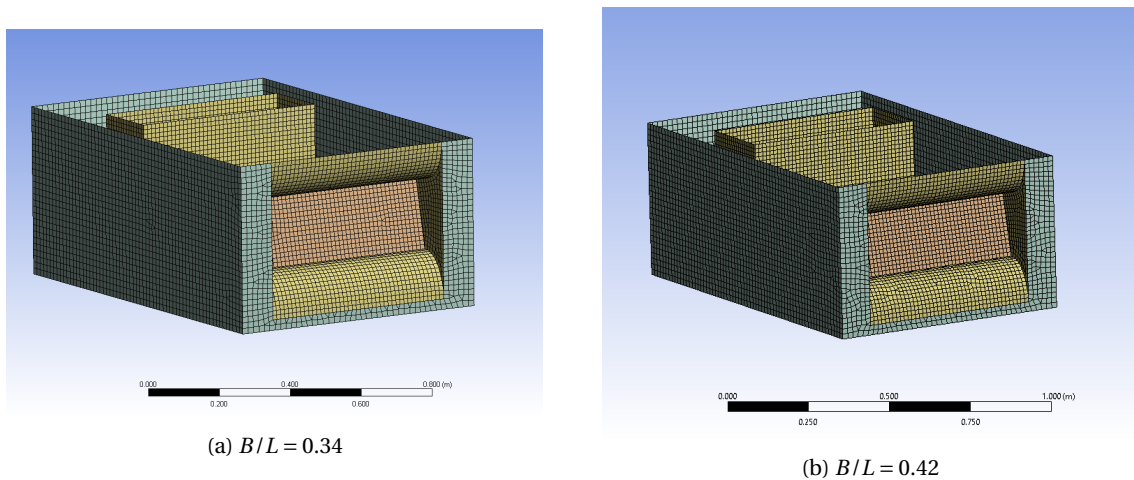


Figure B.8: Generated mesh for AQWA runs.

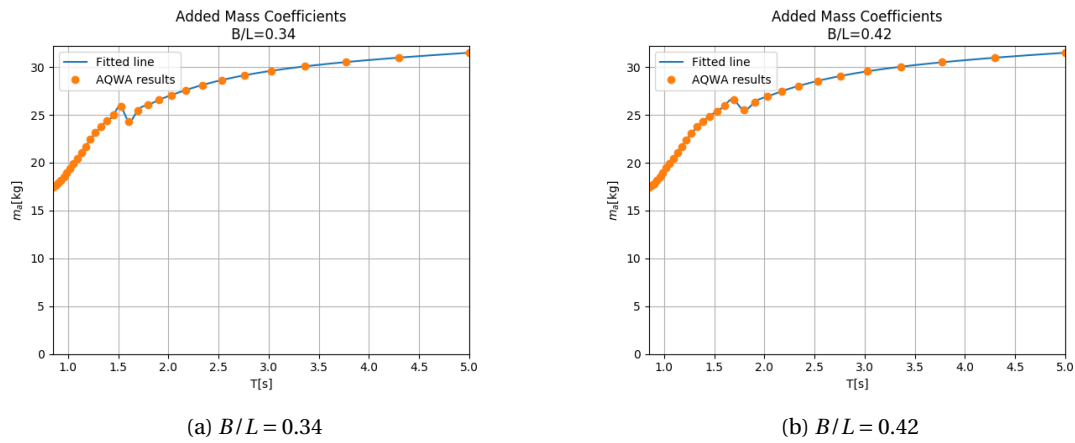


Figure B.9: Added mass coefficients.

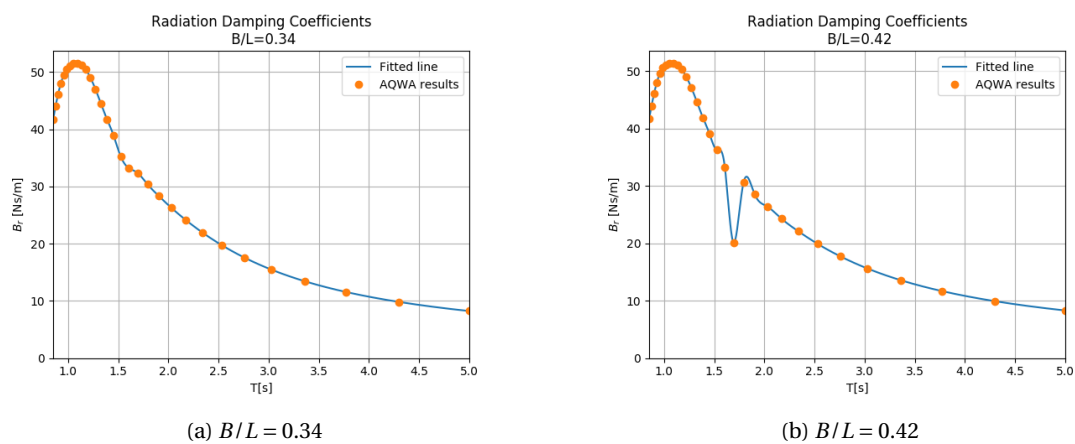


Figure B.10: Radiation damping coefficients.

B.2.4. Results

In figures B.9, B.10 and B.11, the added mass, radiation damping and Froude-Krylov and diffraction force is given, respectively. There are abrupt changes in results at certain frequencies. These frequencies correspond to the natural frequencies of the system. Since AQWA and similar software have difficulties modelling resonance phenomenon in the fluid potential flow the graphs show a sudden change in value.

B.3. Conclusion

This chapter defines the key approach towards modelling the Ocean Falls oscillating water column in ANSYS AQWA. The most important points are summed as follows:

- AQWA has been compared to similar boundary element method software modelling oscillating water columns and it is clear that AQWA gives varying results for piston lengths and requires a finer mesh.
- The Ocean Falls differs essentially in stiffness compared to a simple oscillating water column. This difference effects the AQWA model in the sense that the piston is now imposed into the fluid as a vertical plate.
- An internal lid has been added into the AQWA model to mitigate any irregular frequencies.
- The results given are fine graphs and seem reliable, except for the abrupt peaks at resonant frequencies.

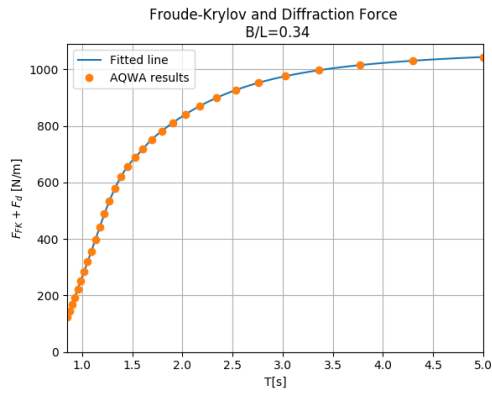
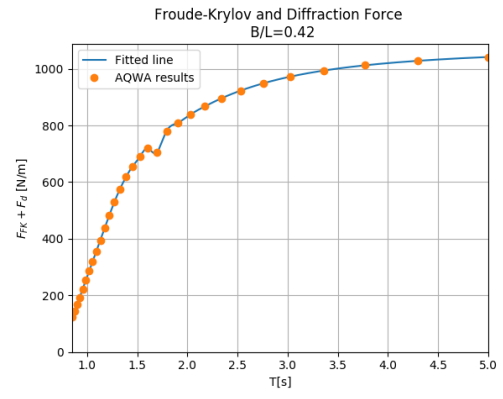
(a) $B/L = 0.34$ (b) $B/L = 0.42$

Figure B.11: Froude-Krylov and Diffraction Forces.

C

Data acquisition and processing

This appendix contains an explanation of the data acquisition systems utilised in the experiment and the processing performed.

C.1. Data acquisition

C.1.1. Wave gauges

The wave gauges utilised in the experiments are standard Edinburgh Design wave gauges. These robust wave gauges measure the elevation of water with 0.1% accuracy of the full span [48]. However, given the fact that the wave gauge disturbs the water surface during the presence of waves and that the wet surface of the gauge will have a slightly increased conductivity, the uncertainties will be slightly higher. The gauges consist of two parallel cylinders that measure the resistance induces by the elevation of the water. The gauges are connected to a controller that further transmits the signal to the computer. The used sampling rate is 32 Hz. See figure C.1. The data acquisition system is not relevant here because it is standard and not unique to this research.



Figure C.1: Wave gauge and controller. This image has been taken from [48].

C.1.2. Pressure sensors

Two pressure sensors of the kind SPD102SAhyb by Smartec were used in the experiments. The data sheet can be found by clicking [here](#). The sensors measure the pressure between 0 to 0.15 psi (circa 1000 Pa) with an accuracy of 2.2% (circa 22 Pa). These sensors measure the pressure linearly starting at 0.5V to 4.0V. The pressure is measured as the difference between both cylinders. See figure C.2. Since the sensor only measures in one direction the second sensor is added to measure in both directions, so measure both positive and negative pressure oscillations. This data can then be combined to accurately depict the pressure oscillation in the chamber. The ratio between voltage and pressure is given in the data sheet as 0.15psi/3.5V, so 1 V corresponds to circa 0.043 psi (circa 300 Pa).

The pressure sensors are connected to a National Instruments USB-6008 Multifunction I/O Device Device that is then connected to the computer. More information on this device can be found [here](#). The data acquisition system set-up in LabVIEW by Jos van Driel. Figure C.3 gives the LabVIEW diagram. The device is set to measure every 31 ms.



Figure C.2: Pressure sensor and interface device.

C.2. Data processing

Now that the data acquisition has been elaborated, the data processing can be explained. All processing has been performed in python 2.7.13.

Firstly, the data that is acquired needs to be chopped. The sections of interest of each data set has to be cut out for both pressure and elevation accordingly. This has been done by visually assessing each measured data set and deciding the amount of data points to cut out from the start and end of the data sets both for pressure and elevation. Secondly, the pressure data sets are downsampled to fit the elevation data sampling rate at 32 Hz. This is done by employing the python 'interp1d' function. If filtering is needed, then the data sets are fourier transformed using the fast fourier transform function 'fft' in python. This transforms the time series data into a representation in the frequency domain. The power spectral density of the data is assessed to filter out frequencies that are not relevant (lower power density). Then an inverse fourier transform 'ifft' is employed to generate a time series sample of the filtered data. The amplitudes and frequencies can be exported to use in the data analysis. If a time domain representation is needed of, for example, the power then the generated time series from the inverse fourier transform need to be aligned. This is needed because the data acquisition of the elevation and pressure were on different computers and could not be started at exactly the same time. The performer of the experiments needed to walk between both computers, which causes a lag in the data. This can be corrected by employing a correlation function to both pressure and elevation data sets ('correlate' in python). The maximum index of the correlation function represents the lag time. The pressure data or elevation data is then shifted to align with the respective other. Then the flow and can be computed either analytically (for filtered data) or numerically through the 'gradient' function in python. The power is simply computed by multiplying both filtered and aligned data sets.

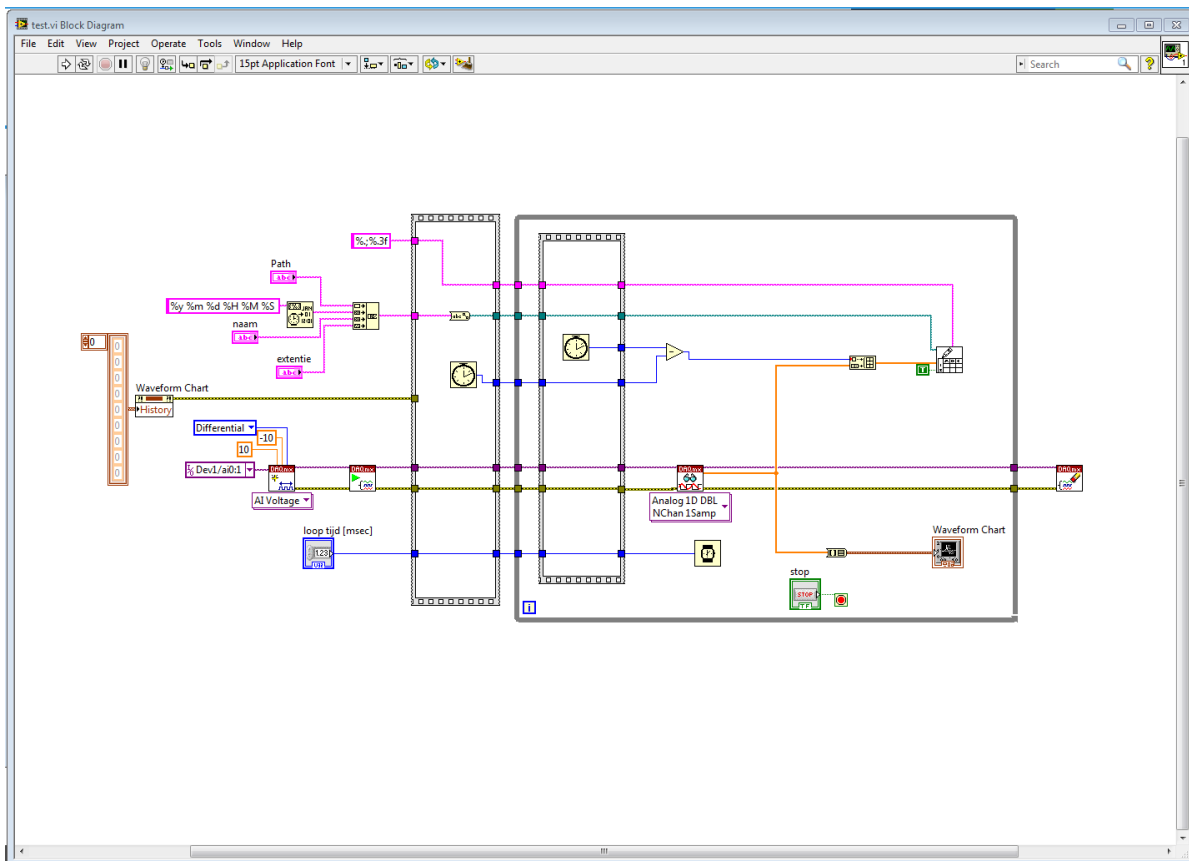


Figure C.3: LabVIEW diagram created by Jos van Driel.

Some error prints were incorporated into the code to avoid mistakes; several examples are lag times longer than 1 period, low correlation or large differences in analytical flow and numerical flow.



Experiments program and protocol

This appendix gives a compact list of steps taken to perform the experiments.

D.1. Experiment program

Figure D.1 gives an overview of the performed experiments.

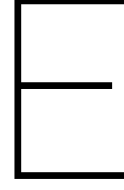
Amplitude: 0.03 m	Calibration	Wall Position 1			Wall Position 2		
		No Damping	Low Damping	High Damping	No Damping	Low Damping	High Damping
Wave Periods [s]	5.00	5.00	5.00	5.00	5.00	5.00	5.00
	4.25	4.25	4.25	4.25	4.25	4.25	4.25
	3.70	3.70	3.70	3.70	3.70	3.70	3.70
	3.30	3.30	3.30	3.30	3.30	3.30	3.30
	2.95	2.95	2.95	2.95	2.95	2.95	2.95
	2.68	2.68	2.68	2.68	2.68	2.68	2.68
	2.45	2.45	2.45	2.45	2.45	2.56	2.56
	2.26	2.26	2.37	2.37	2.37	2.45	2.45
	2.09	2.09	2.26	2.26	2.32	2.41	2.41
	1.95	1.95	2.16	2.16	2.27	2.37	2.37
	1.83	1.83	2.12	2.12	2.26	2.32	2.32
	1.72	1.72	2.09	2.09	2.16	2.26	2.26
	1.62	1.62	2.05	2.05	2.12	2.22	2.22
	1.54	1.54	2.00	2.00	2.09	2.16	2.16
	1.46	1.46	1.95	1.95	2.05	2.09	2.09
	1.39	1.39	1.90	1.90	2.00	1.95	1.95
	1.33	1.33	1.83	1.83	1.95	1.83	1.83
	1.27	1.27	1.72	1.72	1.83	1.72	1.72
	1.21	1.21	1.62	1.62	1.72	1.62	1.62
	1.16	1.16	1.54	1.54	1.62	1.54	1.54
	1.12	1.12	1.46	1.46	1.54	1.46	1.46
	1.08	1.08	1.39	1.39	1.46	1.39	1.39
	1.04	1.04	1.33	1.33	1.39	1.33	1.33
	1.00	1.00	1.27	1.27	1.33	1.27	1.27
	0.97	0.97	1.21	1.21	1.27	1.21	1.21
	0.94	0.94	1.16	1.16	1.21	1.16	1.16
	0.91	0.91	1.12	1.12	1.16	1.12	1.12
	0.88	0.88	1.08	1.08	1.12	1.08	1.08
0.85	0.85	1.04	1.04	1.08	1.04	1.04	
-	-	1.00	1.00	1.04	1.00	1.00	
-	-	0.97	0.97	1.00	-	-	
-	-	0.94	0.94	-	-	-	
-	-	0.91	0.91	-	-	-	
-	-	0.88	0.88	-	-	-	
-	-	0.85	0.85	-	-	-	

Figure D.1: An overview of the performed experiments.

D.2. Experiments protocol

1. Receive Safety Training for the wave lab and sign safety training form.
2. Prepare equipment, measuring devices, desired wave runs in wave generator software and the Ocean Falls model.
3. Fill the flume with water until desired water level is achieved. Enjoy a cup of coffee for several minutes, measure water level and adjust if necessary.
4. Place wave absorbing cushion in the water at the far end of the wave flume so that its surface slightly touches the water surface.
5. Calibration Runs
 - (a) Place two sets of three wave gauges at desire location of Ocean Falls and before it.
 - (b) Start wave piston driver and wave synthesiser software.
 - (c) Calibrate all wave gauges.
 - (d) Load prepared regular wave runs.
 - (e) Run regular wave runs for desired frequencies.
6. Regular Wave Runs
 - (a) No Damping Runs
 - i. Empty wave flume.
 - ii. Remove second set of three wave gauges, insert Ocean Falls into the wave flume, fix structure to the walls of the flume and add ballast rocks inside the structure to prevent floatation.
 - iii. Place one wave gauge before the structure and place two wave gauges inside the internal water chamber aligned parallel to each other.
 - iv. Fill the wave flume to desired wave height. Enjoy a cup of coffee for several minutes, measure water level and adjust if necessary.
 - v. Start wave piston driver and wave synthesiser software.
 - vi. Calibrate all wave gauges.
 - vii. Load prepared regular wave runs.
 - viii. Place a camera to face the Ocean Falls from the side of the flume.
 - ix. Place board with information on which run is going to be filmed in front of camera.
 - x. Start filming on camera.
 - xi. Start wave generator.
 - xii. Observe and note down anything relevant and/or wait until desired run time is over.
 - xiii. Stop wave generator and filming on camera.
 - xiv. Repeat previous 5 steps for all desired regular wave no damping runs.
 - (b) Low Damping Runs
 - i. Measure water level and adjust if necessary.
 - ii. Remove both wave gauges in the internal chamber.
 - iii. Place air chamber lid and seal with silicone until air tight expect for opening of the orifice.
 - iv. Place wave gauges through the orifice opening in the internal chamber.
 - v. Set-up second computer and connect to it the pressure sensor USB interface.
 - vi. Connect to this interface the pressure sensors and place them through the air chamber lid and connect flexible small pipes from these sensors inside the air chamber to the atmosphere through the wall of the air chamber.
 - vii. Start LabVIEW code for pressure measurements on computer.
 - viii. Place board with information on which run is going to be filmed in front of camera.
 - ix. Start filming on camera.
 - x. Start pressure data acquisition on LabVIEW.

- xi. Start wave generator.
 - xii. Observe and note down anything relevant and/or wait until desired run time is over.
 - xiii. Stop wave generator, pressure data acquisition and filming on camera.
 - xiv. Repeat previous 6 steps for all desired regular wave low damping runs.
- (c) High Damping Runs
- i. Adjust air chamber lid to desired high damping scenario.
 - ii. Repeat low damping steps with new air chamber lid.
7. Repeat regular wave runs for second wall position.
 8. Empty wave flume.
 9. Remove Ocean Falls constraints.
 10. Remove Ocean Falls ballast and structure itself.
 11. Retrieve all data needed and clean-up all utilised equipment.



Non-linear time-domain model

This section contains an explanation and results of the non-linear model of the Ocean Falls in time domain. The linear relation between the pressure and flow has been replaced by a quadratic one.

E.1. Non-linear equations of motion

Let us recall the time domain equation of motion in equation 3.27 discussed in chapter 3. As previously mentioned, to solve the non-linear equations, we must solve the equations in the time-domain, like in equation 2.4. The single degree of freedom equation of motion for the oscillation of the elevation inside the chamber for the Ocean Falls given by

$$\rho_w B \ddot{h}(t) + \frac{\rho_w g A}{L} h(t) + \frac{A}{L} p(t) = \frac{f_{wave}(t)}{dL} - \frac{f_{rad}(t)}{dL} \quad (E.1)$$

The radiation forcing term in time-domain has thus been replaced by a convolution integral term, as is described by Cummins [27]. The equation now can be written as

$$\left(\rho_w B + \frac{a_\infty}{dL} \right) \ddot{h}(t) + \frac{1}{dL} \int_0^t K(t-\tau) \dot{h}(\tau) d\tau + \frac{\rho_w g A}{L} h(t) + \frac{A}{L} p(t) = \frac{f_{wave}(t)}{dL} \quad (E.2)$$

where a_∞ is the constant added mass term at $\omega \rightarrow \infty$ and the integral term is the convolution integral described by Cummins. $K(t)$ is the impulse response function representing the fluid memory. Now, let us recall the thermodynamics equations derived in chapter 3. The non-linear description of the pressure oscillations can be described by

$$\dot{m}(t) = \rho_a B \dot{h}(t) - \frac{B(h_{air} - h(t))}{c^2} \dot{p}(t) \quad (E.3)$$

where the assumption is made that the pressure oscillations inside the chamber are small with respect to the atmospheric pressure, so $p_a \gg p$. However, the air chamber height is not assumed to be much larger than the elevation inside the chamber, making the equations non-linear. Also, we can now equate the left hand side to a quadratic relation of pressure and flow given by

$$\dot{m}(t) = \sqrt{K_{1,mes}} |p(t)| \text{sgn}(p(t)) \quad (E.4)$$

where $K_{1,mes}$ is the measured coefficient for the relation between pressure and flow, as described in chapter 6. The non-linear equation describing the pressure now becomes

$$\sqrt{K_{1,mes}} |p(t)| \text{sgn}(p(t)) = \rho_a B d \dot{h}(t) - \frac{B d (h_{air} - h(t))}{c^2} \dot{p}(t) \quad (E.5)$$

Equations E.2 and E.5 are non-linear and can be solved in the time-domain.

E.2. State-space representation of the convolution

The non-linear equations of motions can be solved by direct numerical integration. However, the radiation convolution term can be time-consuming. Therefore, a state-space representation can be used to replace the convolution integral by a series of first order ordinary differential equations. According to Iturrioz et al. [28] the order of this system of ODEs is typically small for wave energy converters.

Following the approach taken in Iturrioz et al. [28], we can replace the integral term by a state-space approximation as

$$\dot{\mathbf{X}}_c(t) = \mathbf{A}_c \mathbf{X}_c(t) + \mathbf{B}_c \dot{h}(t) \quad (\text{E.6})$$

$$y(t) = \mathbf{C}_c \mathbf{X}_c(t) \quad (\text{E.7})$$

where $y(t)$ represents the convolution term in the equations of motion. This term now has been split into a system of ODEs and can be solved for known matrices \mathbf{A}_c , \mathbf{B}_c and \mathbf{C}_c . These coefficients have no physical meaning and can therefore not be measured. However, we know that there has to be a relation between the hydrodynamic coefficients and the convolution term. Ogilvie [56] presents the relation between the frequency dependent added mass and radiation damping coefficients and the time domain transfer function $K(t)$ using the Fourier transform of equation E.2. These equations are given as

$$m_a(\omega) = a_\infty - \frac{1}{\omega} \int_0^\infty K(t) \sin(\omega t) dt \quad (\text{E.8})$$

$$B_r(\omega) = \int_0^\infty K(t) \cos(\omega t) dt \quad (\text{E.9})$$

From this Fourier transform one can also define an expression for the frequency domain representation of $K(t)$. Following Perez and Fossen [57] and Taghipour et al. [58], this relation is given as

$$\tilde{K}_{AQWA}(i\omega) = B_r(\omega) + i\omega[m_a(\omega) + a_\infty] \quad (\text{E.10})$$

where B_r , m_a and a_∞ is the radiation damping, added mass and added mass at infinite frequency, where the former two are obtained through ANSYS AQWA and the latter is obtained through the FDI python toolbox.

This relation can be approximated by a rational function $\hat{K}(s)$, whose numerator and denominator coefficients are determined through the FDI Matlab Toolbox developed by Perez and Fossen [57] and translated to python by J. A. Armesto and R. Guancho [59]. These coefficients approximate the transfer function $\tilde{K}(i\omega)$, which can be represented in the frequency domain as

$$\tilde{K}(i\omega) = \hat{K}(i\omega) = \mathbf{C}_c(i\omega \mathbf{I} - \mathbf{A}_c)^{-1} \mathbf{B}_c \quad (\text{E.11})$$

where the letters in bold are the state-space representation matrices and \mathbf{I} is the identity matrix. Thus, a relation can be given for the frequency domain representation of the transfer function $\tilde{K}(i\omega)$ approximating the transfer function in the convolution term in time-domain.

E.3. Solution in python

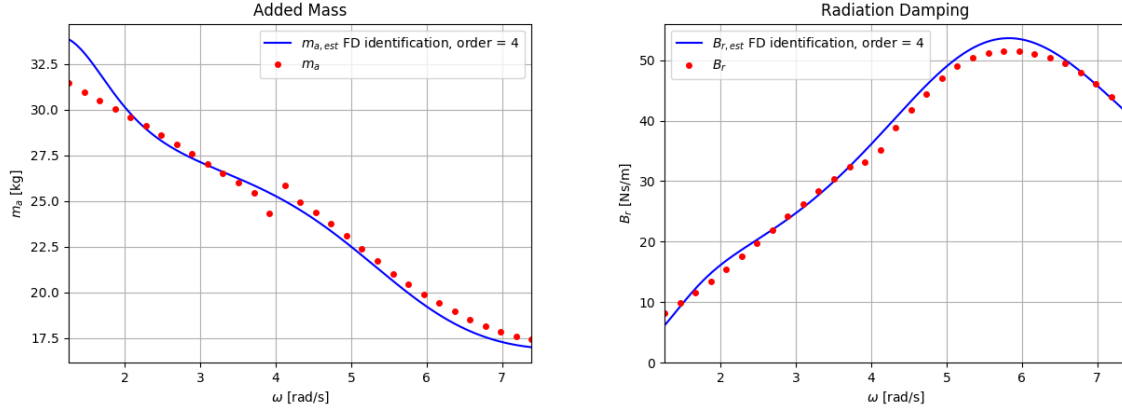
Now that the convolution term is represented by a series of ODEs, we can solve the system of equations numerically. It is convenient to extend the state-space matrices to include the total equations of motion with the addition of three new equations; equations for the internal water surface velocity, internal water surface acceleration and the time derivative of the pressure. Again following Iturrioz et al. [28], the state-space equations can now be written as

$$\dot{\mathbf{X}}(t) = \mathbf{A}\mathbf{X}(t) + \mathbf{B}F_{wave}(t) \quad (\text{E.12})$$

$$z(t) = \mathbf{C}\mathbf{X}(t) \quad (\text{E.13})$$

where

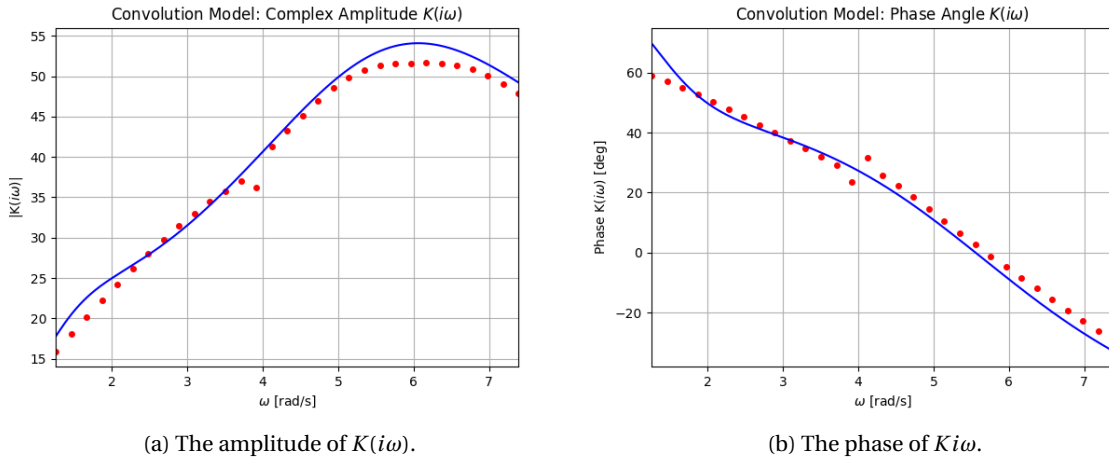
$$\mathbf{X}(t) = [\mathbf{X}_c(t), z(t), \dot{z}(t), p(t)] \quad (\text{E.14})$$



(a) Added mass obtained from AQWA and the respective state-space approximation.

(b) Radiation damping obtained from AQWA and the respective state-space approximation.

Figure E.1: Frequency domain identification of the hydrodynamic coefficients from AQWA using the infinite added mass obtained from the FDI toolbox.



(a) The amplitude of $K(i\omega)$.

(b) The phase of $Ki\omega$.

Figure E.2: Frequency domain identification of the fluid memory function $K_{i\omega}$ using the the infinite added mass obtained from the FDI toolbox.

The above equation can easily be solved in the time-domain with an ODE solver employed in python. The matrices \mathbf{A} , \mathbf{B} and \mathbf{C} are now augmented with the equations of motion presented in equations E.1 and E.5. The solver utilises the python `scipy.integrate.odeint` package. The composition of the state-space matrices has been filled according to Iturrioz et al. [28].

E.4. Results

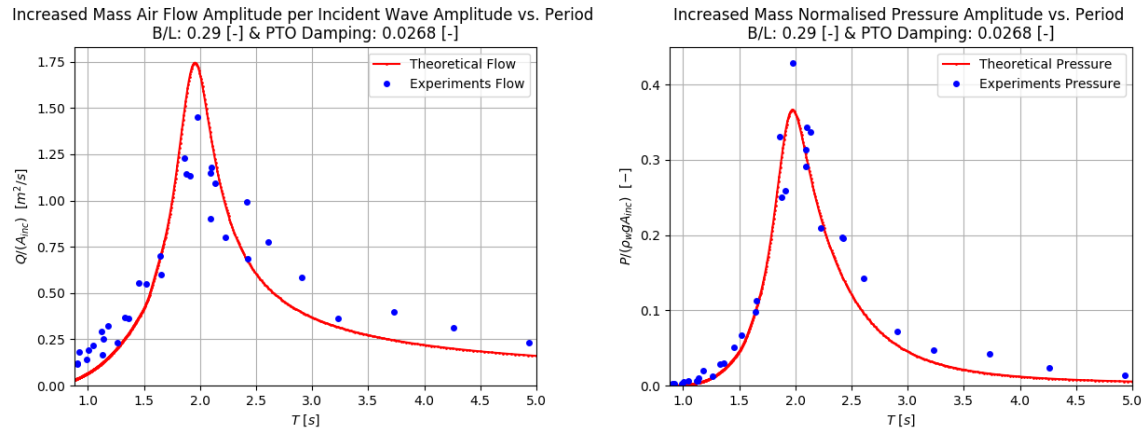
This section contains the results of the non-linear model. First, the approximation of the fluid memory function is presented followed by the solution of the model and its comparison to a regular wave excitation.

E.4.1. Validity of approximation

Before solving the equations, let us consider the validity of the state-space approximation by comparing equations E.10 and E.11. Considering the first wall position and low damping cases, figure E.1 gives the hydrodynamic coefficients computed in AQWA and the state-space approximation. The state-space model gives a fairly good approximation. Figure E.2 gives the fluid memory function $\tilde{K}(i\omega)$ and the approximation employed through the state-space model, again giving a good approximation.

E.4.2. Engineering approach to model and experiments comparison

In the report main body, it is clear from the comparisons of the linear model and the experiment results, that the peak periods do not align. The main reason for this is thought to be the inadequate AQWA model. Therefore, the non-linear model is also likely to not have the same peak period as is observed in the experiments, meaning any comparison made will not match. See for example the low damping case for $B/L = 0.34$ in figure 6.10. As an engineering approach, let us increase the mass of the tube so that the peaks align. This gives figure E.3. The length of the tube has been increased from 60 cm to 70 cm, so an increase of circa 17%.



(a) Air flow versus the wave excitation period for $L = 0.7m$ (b) Pressure versus the wave excitation period for $L = 0.7m$

Figure E.3: Air flow and pressure amplitudes for an increased tube length to $L = 0.7m$.

Recalling equations E.12 - E.14, the augmented state-space matrices can be solved to yield the internal water elevation, internal water velocity and the air pressure inside the chamber. This is done by employing an ordinary differential equation solver in python using the `scipy.integrate.odeint` packages.

Keeping the above mentioned approach in mind, let us now solve the non-linear model for a regular wave with period $T = 2.12s$ (close to resonance) and amplitude equal to the incident wave amplitude determined through the Mansard & Funke reflection analysis. The obtained non-linear results will be compared to the experiment data for the corresponding wave run. Figures E.4 and E.5 give respectively the flow and pressure in time. Similarly, we can consider the system for a regular wave with period $T = 1.53s$. Figures E.6 and E.7 give the results for this case. Please note here that the data has not been filtered and the lag between the data sets and the models has been removed by shifting the data sets to align the experiment data peaks to the model peaks. Figures E.8 - E.11 give the corresponding zoomed versions of figures E.4 - E.7 mentioned in this paragraph.

The results presented above show that the non-linear model approximates the system better than the linear model, especially for the excitation wave period of $T = 2.12s$, which is close to resonance. This analysis of course has to be performed for all the periods studied in the experiments and also for all the different damping cases and wall positions. However, based on this short analysis, this non-linear model yields a promising path to pursue to more accurately model the Ocean Falls.

E.5. Discussion

Firstly, one must consider the 'engineering' approach taken in this analysis. The shift in resonance period between the data and the linear model has been removed by increasing the tube length, based on the assumption that the added mass coefficients are underestimated in the AQWA model. This approach has no real basis. In a more elaborate study, the AQWA model should be improved by, for example, moving the position of the piston more towards the inlet. Also, a comparison should be made with similar software like WAMIT or NEMOH.

Secondly, the analysis is done for just one damping and wall position scenario and just for two wave periods. The drawn conclusions are therefore only based on a portion of the data and model results.

Finally, one should note that only the non-linear pressure-flow relation and the non-linear change in air compressibility stiffness has been included in this model. Other non-linearities or non-linear phenomenon, such as friction, can be added into the model without too complex modifications.

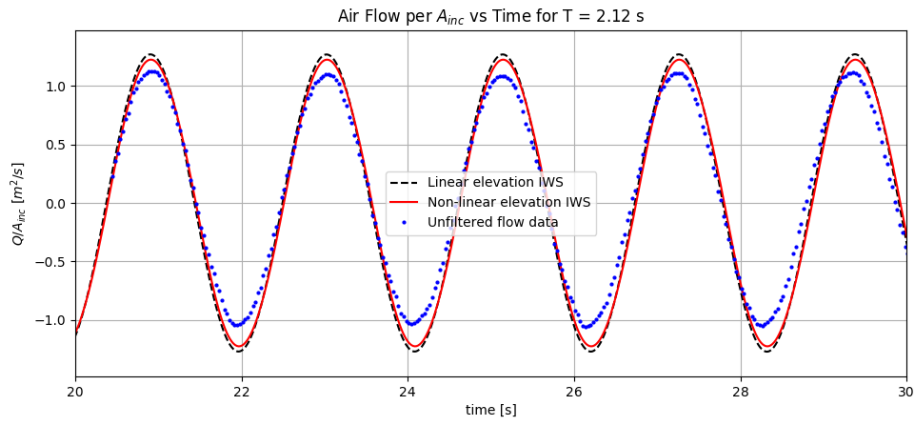


Figure E.4: Air flow per meter incident wave amplitude for $T = 2.12$ s for the linear model, non-linear model and unfiltered experiment data.

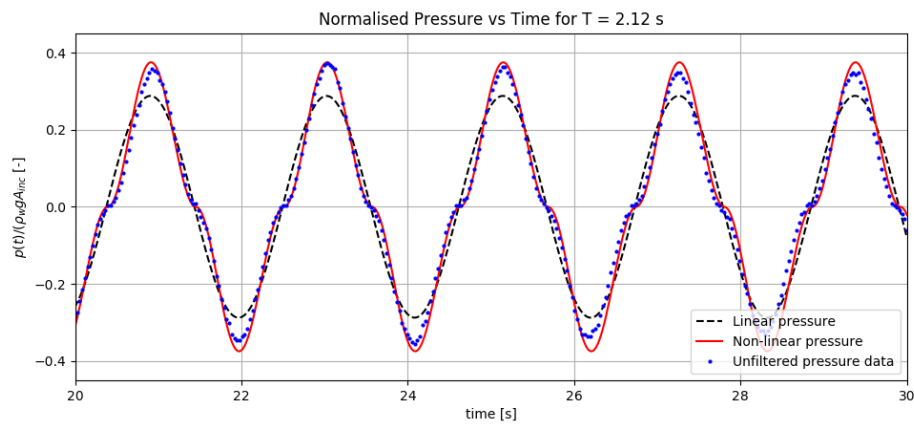


Figure E.5: Normalised pressure for $T = 2.12$ s for the linear model, non-linear model and unfiltered experiment data.

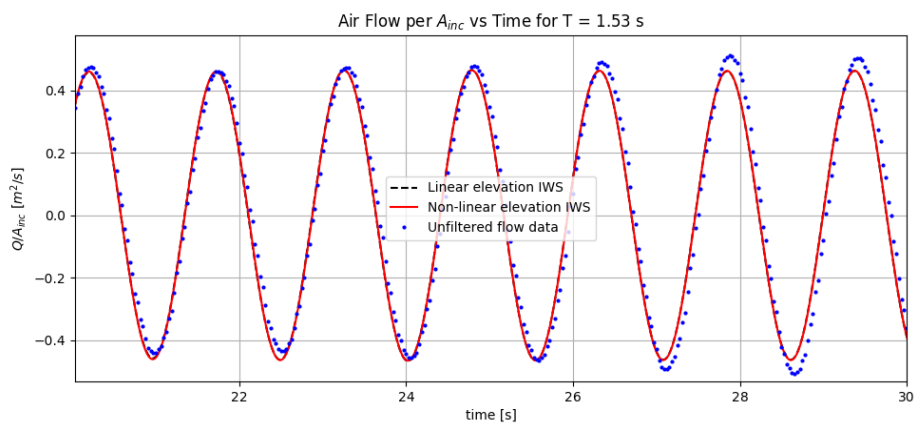


Figure E.6: Air flow per meter incident wave amplitude for $T = 1.53$ s for the linear model, non-linear model and unfiltered experiment data.

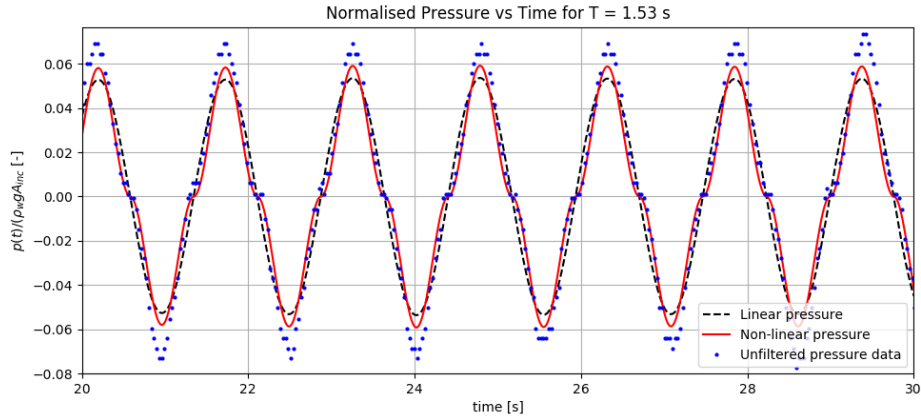


Figure E.7: Normalised pressure for $T = 1.53\text{ s}$ for the linear model, non-linear model and unfiltered experiment data.

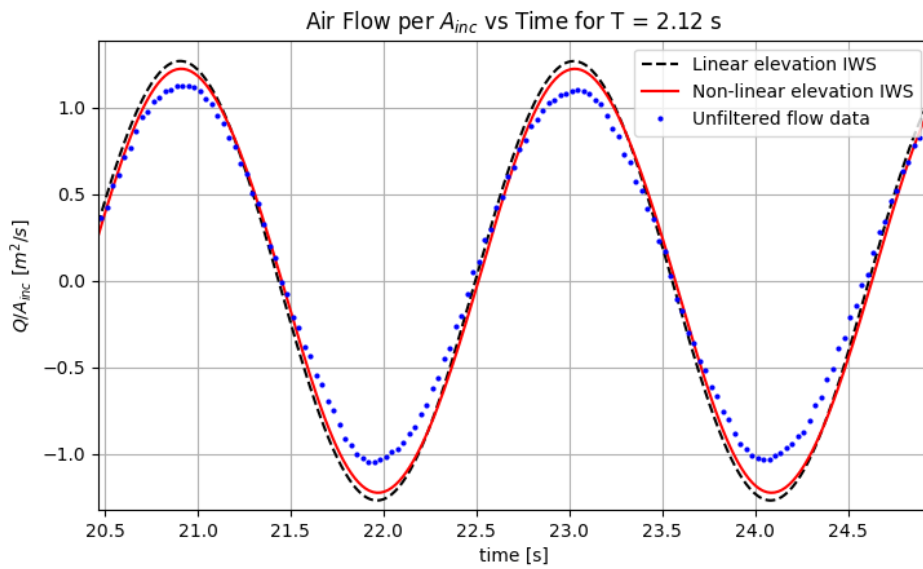


Figure E.8: Zoomed in air flow per meter incident wave amplitude for $T = 2.12\text{ s}$ for the linear model, non-linear model and unfiltered experiment data.

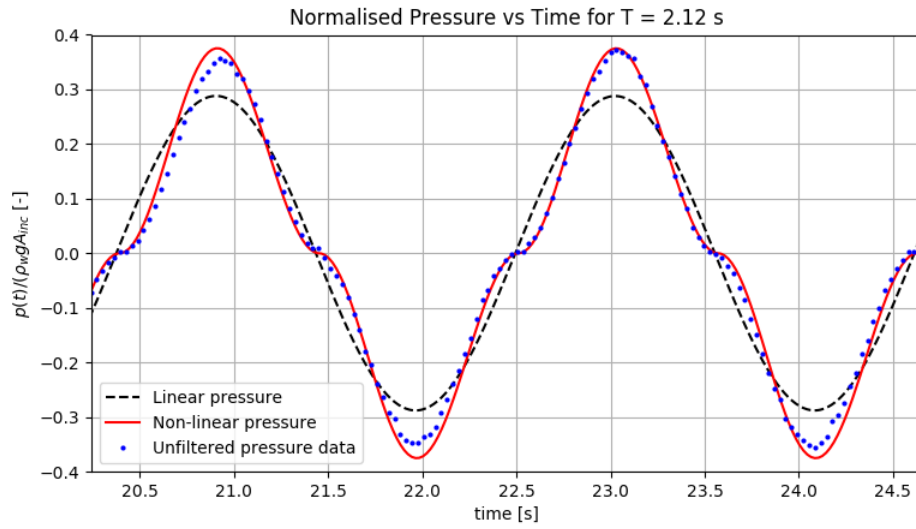


Figure E.9: Zoomed in normalised pressure for $T = 2.12s$ for the linear model, non-linear model and unfiltered experiment data.

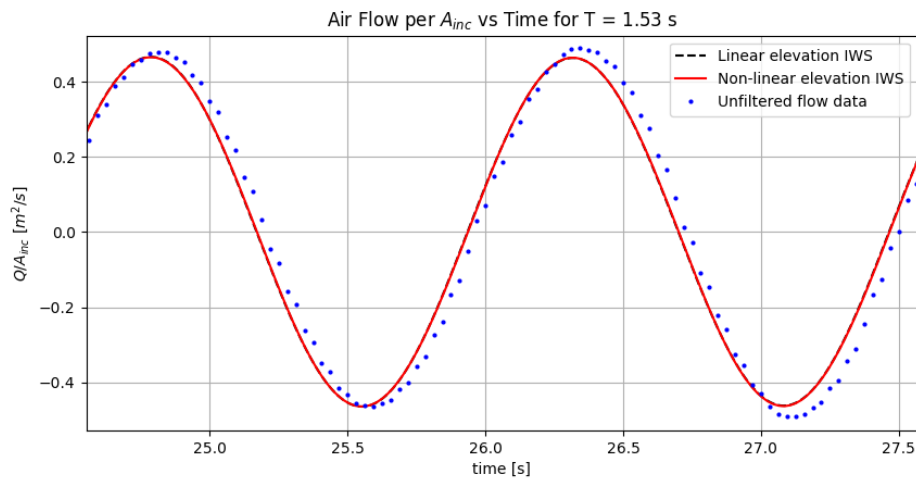


Figure E.10: Zoomed in air flow per meter incident wave amplitude for $T = 1.53s$ for the linear model, non-linear model and unfiltered experiment data.

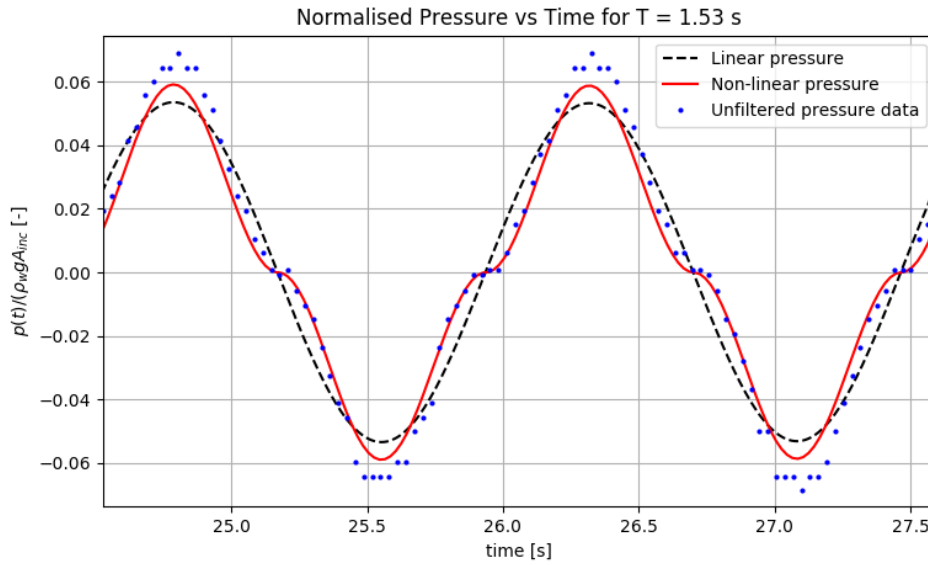


Figure E.11: Zoomed in normalised pressure for $T = 1.53s$ for the linear model, non-linear model and unfiltered experiment data.

E.6. Conclusion

In conclusion, this non-linear approach, considering the results presented for one wall position and one damping case for two periods, is promising and yields impressive results. It is important to underline once more that it is recommended to revise the AQWA model by choosing the optimum piston position (see Appendix B) and also to compare the AQWA results to other software, such as WAMIT or NEMOH.